FACULTY OF ENGINEERING AND ARCHITECTURE

Shear wave elastography for assessing interstitial fluid pressure in tumours

Ariana Cihan
Student number: 02100167

Supervisors: Prof. dr. ir. Patrick Segers, Prof. dr. ir. Charlotte Debbaut
Counsellor: Dr. ir. Annette Caenen

Master's dissertation submitted in order to obtain the academic degree of
Master of Science in Biomedical Engineering

Academic year 2022-2023

GHENT UNIVERSITY

VUB VRIJE UNIVERSITEIT BRUSSEL

FACULTY OF ENGINEERING AND ARCHITECTURE

Shear wave elastography for assessing interstitial fluid pressure in tumours

Ariana Cihan
Student number: 02100167

Supervisors: Prof. dr. ir. Patrick Segers, Prof. dr. ir. Charlotte Debbaut
Counsellor: Dr. ir. Annette Caenen

Master's dissertation submitted in order to obtain the academic degree of
Master of Science in Biomedical Engineering

Academic year 2022-2023

GHENT UNIVERSITY

VUB VRIJE UNIVERSITEIT BRUSSEL

Permission of Use of Loan

"The author gives permission to make this master dissertation available for consultation and to copy parts of this master dissertation for personal use. In all cases of other use, the copyright terms have to be respected, in particular with regard to the obligation to state explicitly the source when quoting results from this master dissertation."

Ariana Cihan, June 2023

Acknowledgements

First and foremost, I would like to express my sincere appreciation to my counsellor Dr. Ir. Annette Caenen, whose guidance has been invaluable throughout my thesis. Her expertise, observations, and time have significantly contributed to the development of this work and my understanding in the topic. I am truly thankful for the informative and useful meetings we had, and to have delved into the world of research under her mentorship.

Additionally, I would like thank my supervisors Prof. Dr. Ir. Patrick Segers and Prof. Dr. Ir. Charlotte Debbaut, for providing me with opportunities, knowledge, and resources to lead me in the right direction. They introduced me to the world of computational modelling and were always supportive both during previous courses and during my thesis.

Furthermore, I am grateful to Ir. Kristyna Holkova, whose thesis laid a solid foundation for my own work. Her meticulous research enabled me to carry on with the topic and dig deeper into the research. I would also like to acknowledge the contributions of other researchers, such as Ir. Hooman Salavati, whose insights have been particularly valuable.

Lastly, I want to express my heartfelt appreciation to my family, friends, and fellow students for their support throughout my thesis, academic career, and semester abroad. Their encouragement, help and presence have been a source of strength and joy, and I am grateful for having each and every one of them by my side.

Ariana Cihan

5th of June, 2023

Remark

"This master's dissertation is part of an exam. Any comments formulated by the assessment committee during the oral presentation of the master's dissertation are not included in this text."

Abstract

In (malignant) solid tumours, the Interstitial Fluid Pressure (IFP) is elevated [70, 89], which creates an outward fluid flow away from the tumour and hence limits the amount of therapeutic drugs that reaches the tumour centre through convection [30]. In fact, the drug distribution is concentrated at the periphery of the tumour while 90% of the tumour volume receives very little to no drugs [75]. IFP has therefore been shown to be a valuable marker for both diagnosis and prognosis of many solid cancer types [33, 36].

Accurate and non-invasive measurements of the IFP would be clinically valuable for developing patient-specific and optimized drug delivery strategies, and monitor the efficacy of treatments designed to lower IFP over time [80]. Currently, only invasive techniques exist, limiting the widespread use of IFP measurements in clinical practice. However, Shear Wave Elastography (SWE) has emerged as a promising non-invasive alternative for measuring the IFP indirectly. SWE is used currently to measure tissue stiffness based on ultrasound. Previous studies and experiments have shown that the shear wave velocity (SWV) measured during SWE is correlated to the IFP, and that elevated IFP increases the apparent observed tissue stiffness [1, 31, 51, 66, 88, 89]. Therefore, this work explores how the IFP affects the SWV through computational modelling in COMSOL Multiphysics® 6.1 (COMSOL AB, Stockholm, Sweden).

Keywords- Shear Wave Elastography (SWE), Interstitial Fluid Pressure (IFP), solid tumours, computational modelling, poroelasticity

Shear Wave Elastography for Assessing Interstitial Fluid Pressure in Tumours

Ariana Cihan
Supervisors: Patrick Segers, Charlotte Debbaut
Counsellor: Annette Caenen

***Abstract*—The Interstitial Fluid Pressure (IFP) is elevated in solid tumours and limits the efficacy of therapeutic agents. IFP measurements would be clinically valuable for diagnosis, prognosis, and drug delivery optimisation. Shear Wave Elastography (SWE) has emerged as a promising non-invasive technique for assessing the IFP indirectly. In this study, the influence of the IFP on the Shear Wave Velocity (SWV) measured through SWE is assessed through numerical modelling in COMSOL Multiphysics® in a poro- and hyperelastic tissue.**

***Keywords*— Shear Wave Elastography (SWE), Interstitial Fluid Pressure (IFP), solid tumours, computational modelling, poroelasticity**

I. Introduction

(Malignant) solid tumours are characterised by elevated Interstitial Fluid Pressure (IFP) [1, 2]. Typical values from 10 to 40 $mmHg$ have been reported in various solid tumours, such as in head, neck, breast, and cervical cancer, with highest recordings going up to 100 $mmHg$ in malignant melanomas [1]. The pressure difference with the surrounding tissue creates a fluid flow away from the tumour, which limits the amount of therapeutic drugs that reach the tumour centre through convection [3]. In fact, the drug distribution is concentrated at the periphery of the tumour while 90% of the tumour volume receives very little to no drugs [4], and IFP is therefore indicative for diagnosis and prognosis of many solid cancers [5, 6].

Currently, only invasive techniques are used for measuring IFP in clinical practise, limiting its widespread use. On the contrary, accurate and non-invasive measurements of the IFP would be valuable for optimizing drug delivery strategies and monitoring the efficacy of treatments designed to lower IFP over time [7]. Shear Wave Elastography (SWE) has emerged as an indirect non-invasive alternative for measuring the IFP. Currently, the technique is used to measure tissue stiffness based on ultrasound, but previous studies and experiments have shown that the Shear Wave Velocity (SWV) measured during SWE is correlated to the IFP [2, 8–12]. Therefore, this work explores how the IFP affects the SWV through computational modelling in COMSOL Multiphysics® 6.1 (COMSOL AB, Stockholm, Sweden). This is done as follows. First, a material model for a poroelastic tissue is constructed. The tissue is then pressurised, and shear waves are generated. Post-processing allows to determine the SWV, and subsequently, the IFP-SWV relationship.

II. Materials & Methods

A. Material Model

As the extracellular matrix consists of structural elements and the interstitial fluid, it can be represented by a poroelastic material, where deformation of a solid matrix induces fluid flow and vice-versa. A poroelastic soft tissue is recreated in COMSOL Multiphysics® by manually coupling the Solid Mechanics module to the Free and Porous Media Flow module bidirectionally, as validated by [13]. Here, the fluid pressure (P) governed by the Free and Porous Media Flow module induces a body load on the solid phase, resulting in either swelling or shrinking. Alternatively, changes in volumetric strain (ε_{vol}) of the solid phase influence the fluid phase similarly to a mass source. The manually added coupling factors are represented by [8, 13, 14]:

$$\mathbf{F} = -\nabla \mathbf{P} \tag{1a}$$

$$Q_{br} = -\rho \frac{\partial \varepsilon_{vol}}{\partial t} \tag{1b}$$

where the volumetric body force F (units N/m^3) is added to the solid phase and the mass source Q_{br} (units $kg/(m^3 \cdot s)$) is added to the fluid phase. Additionally, porosity and permeability should increase or decrease with tension or compression, so they are modelled as strain-dependent variables according to [15, 16]:

$$\phi = \frac{\phi_0 + \varepsilon_{vol}}{1 + \varepsilon_{vol}} \tag{2a}$$

$$k = k_0 e^{M\varepsilon_{vol}} \tag{2b}$$

where ϕ is the porosity (dimensionless), ε_{vol} the volumetric strain (dimensionless), k the permeability (units m^2), M an exponential parameter of the permeability (dimensionless), and subscript 0 describes the initial configuration. These equations are also manually inserted into COMSOL Multiphysics®.

Linear elasticity is often insufficient to adequately describe soft biological tissues, especially at high strains. Therefore, both linear and hyperelastic tissues are modelled. The hyperelastic tissue is described by a first order Ogden strain energy function. An overview of all material parameters is shown in Tab. I.

TABLE I
Overview of material parameters. Values for linear solid matrix and interstitial fluid taken from [8]. Values for hyperelastic solid matrix roughly fitted to experiments in chicken breasts from [8]. Values for porous medium calculated from [17].

Linear solid matrix	
Young's modulus	$E = 100\ kPa$
Poisson's ratio	$\nu = 0.495$
Density	$\rho = 945\ kg/m^3$
Hyperelastic solid matrix	
Ogden parameters	$\mu_1 = 0.15\ kPa$, $\alpha_1 = 70$
Density	$\rho = 945\ kg/m^3$
Interstitial fluid	
Viscosity	$\mu = 1.5 \cdot 10^{-3}\ Pa \cdot s$
Density	$\rho = 1000\ kg/m^3$
Porous medium	
(Initial) porosity	$\phi = 0.51$
(Initial) permeability	$k = 5.3 \cdot 10^{-12}\ m^2$
Exponential factor	$M = 4.3$

B. Geometry and Mesh

The Region of Interest (ROI) is a square with sides of 30 mm and represents the tissue under investigation. A layer of 20 mm

surrounding ROI is modelled as well to prevent reflections of shear waves within the ROI. The same material model is used throughout complete geometry.

As the 2D geometry is simple and regular, a uniform mesh can be obtained with quadrilateral elements (4 nodes). These elements don't contain sharp angles. Additionally, they are aligned with the primary shear wave propagation and displacement directions, reducing numerical dispersion artifacts [8, 18]. A mesh with 84100 mesh elements and a maximal element size of $0.242\ mm$ is selected based on a mesh sensitivity analysis.

C. Boundary Conditions and Pressurisation

The boundary conditions that are applied on the geometry are illustrated in Fig. 1. The solid matrix is fixed at the central point of the bottom edge, while roller constraints are placed along the entire bottom edge. The interstitial fluid is pressurised through inlet (for fluid inflow) and outlet (for fluid outflow) boundary conditions. Inlet pressures ranging from $0 - 120\ mmHg$ are applied on the top and bottom edges and an outlet pressure of $0\ mmHg$ is applied on the sides.

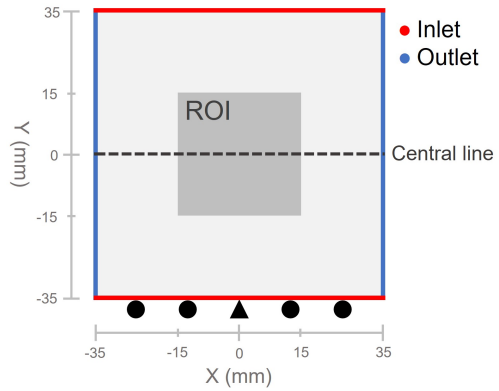

Fig. 1. Boundary conditions of healthy model. The solid matrix is fixed at the central point of the bottom edge and roller constraints are placed along the entire bottom edge. An inlet fluid pressure between $0 - 120\ mmHg$ is applied at the top and bottom boundary and an outlet pressure of $0\ mmHg$ at the sides.

D. Shear Wave Generation and Post-Processing

In this study, Acoustic Radiation Force Impulse (ARFI)-driven SWE is considered, whereby a high-intensity pulse or ARF is generated at a particular tissue depth with an ultrasound (US) transducer. This induces tissue displacements perpendicular to the transducer surface (axial or Y direction) that propagate parallel to the transducer surface (lateral or X direction). In the numerical model, shear waves are generated by applying a downward time-dependent body load, representing the ARF, of $1.5 \cdot 10^6\ N/m^3$ in the axial direction over an area of 1 by 5 mm in the centre of the geometry. The height is chosen as in [8]. The body load magnitude and area are set such that realistic tissue displacements are induced (peak displacements should be in the range of $10 - 20\ \mu m$ [19]).

The ARF push is represented by a rectangular load of $0.3\ ms$ [8] (typically $0.1 - 0.5\ ms$ [18]) with smooth transition zones (of $20\ \mu s$) to improve convergence. The total simulation time, starting with the application of the body load, is $3\ ms$. As such, the shear waves can propagate sufficiently across models with different material parameters to allow accurate tracking of the SWV. Similarly, the maximal time step of the solver is constrained to $0.01\ ms$ and the results at every $0.01\ ms$ are stored for post-processing.

The axial velocities of the solid phase in all mesh nodes and at all timeframes are exported from COMSOL Multiphysics® and imported into MATLAB R2020b (The MathWorks Inc., Natick, MA, USA) for post-processing. During post-processing, only the values within the ROI are extracted and interpolated onto a regular grid containing approximately the same number of nodes as the original mesh in the ROI. The velocity of the shear waves propagating to the left and right is estimated using the Radon sum transform [20]. This code was provided by Dr. Ir. Annette Caenen.

E. Simulation Pipeline

The simulation process consists of two distinct steps, followed by post-processing to obtain the SWVs. An overview of the process is provided in Fig. 2. Initially, the material undergoes a stationary step where the IFP is applied, meaning that the steady-state solution after the pressurisation is obtained. In the subsequent step, the fluid pressure is maintained, shear waves are generated and their propagation is analysed, thereby inherently requiring a time-dependent study.

For both steps, the default solver configurations of COMSOL Multiphysics® are implemented. An 'automatic' nonlinear method is used in the stationary solver and the iterative process is terminated using a relative tolerance of 0.001 (default). For the time-dependent step, an implicit solver is employed with a method based on BDF (backward differentiation formula). Importantly, the maximum step constraint is changed from 'automatic' to a 'constant' value of $0.01\ ms$ to ensure the time steps taken by the solver don't exceed the time step used for post-processing.

III. Results & Discussion

A. Comparison to Theoretical Values

The SWV obtained through computational modelling in the non-pressurised case can be compared to theoretical values. In a linear elastic material, the SWV c_s can be written in terms of the shear modulus μ or Young's modulus E [21]:

$$c_s = \sqrt{\frac{G}{\rho}} \tag{3a}$$

$$c_s = \sqrt{\frac{E}{2\rho(1+\nu)}} \tag{3b}$$

For a linear elastic tissue with $E = 100\ kPa$, the theoretical SWV is $5.95\ m/s$. For the first order hyperelastic Ogden model, the shear modulus can be approximated by:

$$\mu = \frac{\mu_1 \alpha_1}{2} \tag{4}$$

where μ_1 and α_1 are the first order Ogden parameters. This results in a theoretical SWV of $2.36\ m/s$. By comparison, the mean SWV of the right and left propagating shear waves in the computational model are $6.07\ m/s$ and $2.91\ m/s$ in the linear and hyperelastic tissues, respectively. The theoretical values are lower than the computationally obtained values. This could be due to numerical dispersion or due to the fact that the theoretical values are approximations. Nevertheless, the comparison with theoretical values validates the model's ability to provide realistic estimates of the SWV.

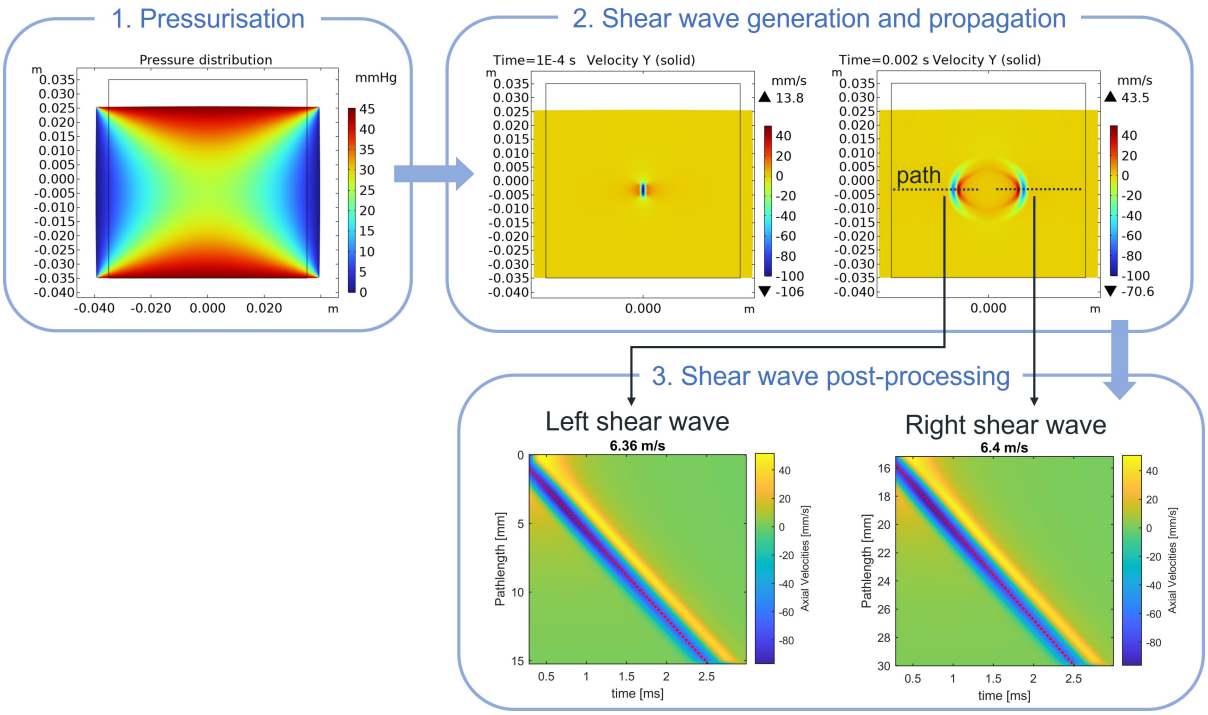

Fig. 2. Overview of the simulation process.

B. SWE in Pressurised Tissues

The resulting shear wave propagation in a pressurised hyperelastic tissue is shown in Fig. 3. It can be seen that shear waves propagate faster when the tissue is pressurised. High (and mostly quadratic) correlations between the IFP, stresses, and strains and the SWV are observed, as shown in Fig. 4. The results in pressurised linear elastic tissues are not shown here, but also show high (and mostly linear) correlations.

Elevated IFP noticeably affects SWV in both linear and hyperelastic tissues. In linear elastic tissues, this could be due to the geometric nonlinearity as noted in [22]. In hyperelastic tissues, the shear modulus increases with strain and introduces an additional nonlinear term.

Supplementary simulations have confirmed that the SWV is not affected by pressurisation if the tissue is constrained, i.e., not allowed to deform during pressurisation, as observed experimentally in [9].

IV. Conclusion

The model developed in this study allows to examine how the SWV increases with the IFP. Comparison of the non-pressurised computationally obtained SWVs proved to be similar to the theoretical values, proving that realistic values are obtained.

In the models' current configuration, determination of the absolute value of the IFP within a tissue is not yet possible without knowledge of the tissue parameters, as comparison of the tumour SWV with adjacent tissues is not sufficient to decouple the influence of tumour stiffness and IFP. Therefore, only the variation in fluid pressure over time can be determined currently, which would already be useful for monitoring the efficacy of treatments designed to lower the IFP over time that aim to improve uptake of other therapeutic drugs to the tumour.

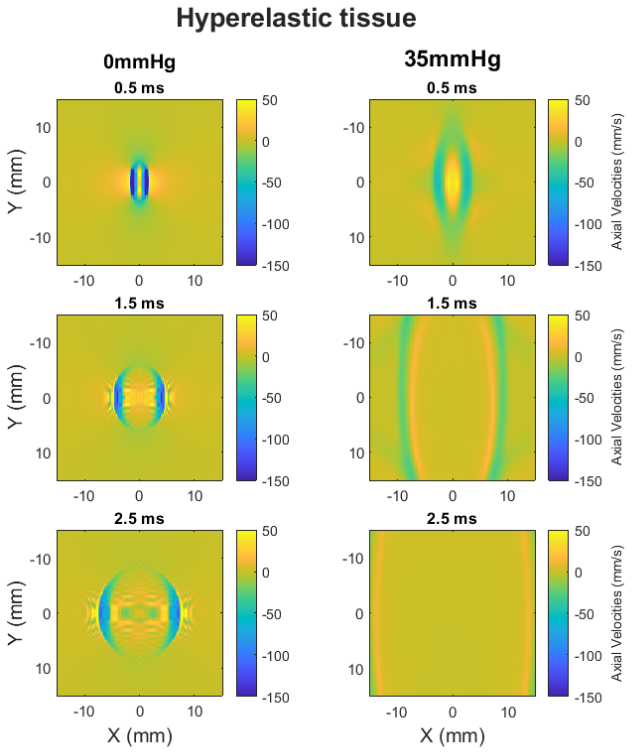

Fig. 3. Influence of pressurisation on shear wave propagation. SWV is increased in the pressurised tissue (right) compared to the non-pressurised tissue (left).

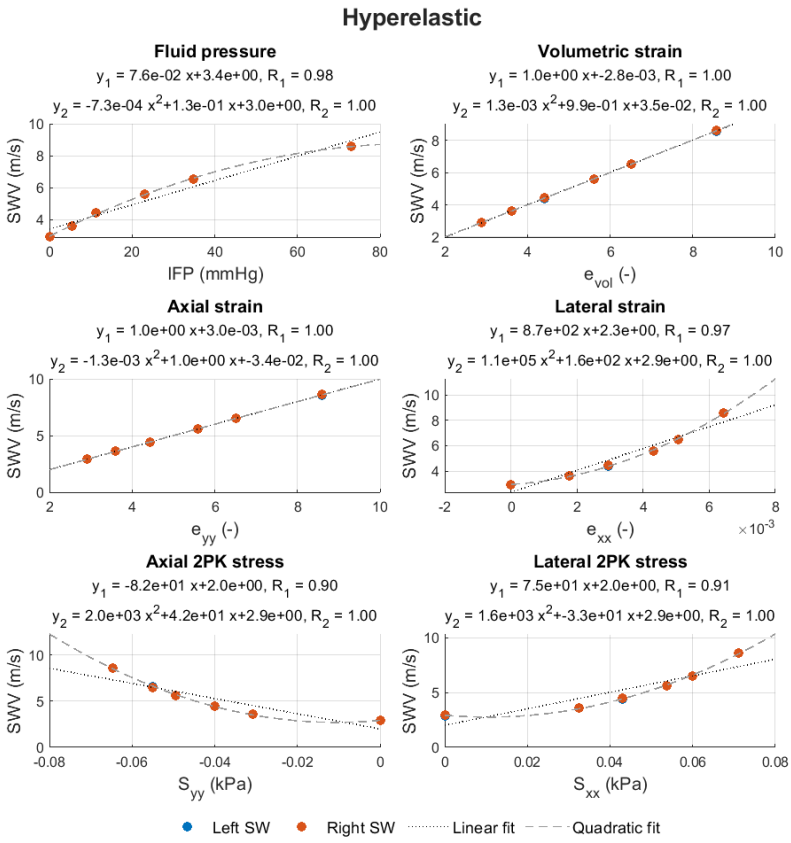

Fig. 4. Relationships between the SWV and the IFP, stresses, and strains in the centre of the model. Both linear and quadratic fits of the mean SWV are provided for comparison.

Moreover, this model can serve as a basis to test whether additional measurements in the time and/or frequency domain can allow to characterise the tissue and fluid pressure. Finally, the model developed in this study could also be used to study the effect of fluid pressure in a multitude of disorders, such as oedema.

References

[1] H. Salavati, C. Debbaut, P. Pullens, and W. Ceelen, "Interstitial fluid pressure as an emerging biomarker in solid tumors," *Biochimica et Biophysica Acta (BBA) - Reviews on Cancer*, vol. 1877, no. 5, p. 188792, 09 2022.

[2] Y. Zheng, Y. Jiang, and Y. Cao, "Effects of interstitial fluid pressure on shear wave elastography of solid tumors," *Extreme Mechanics Letters*, vol. 47, p. 101366, 2021.

[3] C.-H. Heldin, K. Rubin, K. Pietras, and A. Östman, "High interstitial fluid pressure — an obstacle in cancer therapy," *Nature Reviews Cancer*, vol. 4, no. 10, p. 806–813, 10 2004.

[4] M. Soltani and P. Chen, "Numerical modeling of fluid flow in solid tumors," *PLOS ONE*, vol. 6, no. 6, pp. 1–15, 06 2011.

[5] M. T. Islam, S. Tang, E. Tasciotti, and R. Righetti, "Non-invasive assessment of the spatial and temporal distributions of interstitial fluid pressure, fluid velocity and fluid flow in cancers in vivo," *IEEE Access*, vol. 9, pp. 89 222–89 233, 2021.

[6] H.-G. Kim, A. R. Yu, J. J. Lee, Y.-J. Lee, S. M. Lim, and J. S. Kim, "Measurement of tumor pressure and strategies of imaging tumor pressure for radioimmunotherapy," *Nuclear Medicine and Molecular Imaging*, vol. 53, no. 4, p. 235–241, 06 2019.

[7] L. Tan, M. D. J. McGarry, E. E. W. Van Houten, M. Ji, L. Solamen, W. Zeng, J. B. Weaver, and K. D. Paulsen, "A numerical framework for interstitial fluid pressure imaging in poroelastic mre," *PLOS ONE*, vol. 12, no. 6, p. e0178521, 06 2017.

[8] K. Holkova, "Shear wave elastography for assessing interstitial fluid pressure: a combined computational-experimental study," Master's thesis, Ghent University, 2022.

[9] V. Rotemberg, M. Palmeri, R. Nightingale, N. Rouze, and K. Nightingale, "The impact of hepatic pressurization on liver shear wave speed estimates in constrained versus unconstrained conditions," *Physics in Medicine & Biology*, vol. 57, no. 2, p. 329, 12 2011.

[10] Y. Zheng, Y. Jiang, and Y. Cao, "A porohyperviscoelastic model for the shear wave elastography of the liver," *Journal of the Mechanics and Physics of Solids*, vol. 150, p. 104339, 2021.

[11] N. Nazari and P. Barbone, "Shear wave speed in pressurized soft tissue," *Journal of the Mechanics and Physics of Solids*, vol. 119, pp. 60–72, 2018.

[12] J. Aichele and S. Catheline, "Fluids alter elasticity measurements: Porous wave propagation accounts for shear wave dispersion in elastography," *Frontiers in Physics*, vol. 9, 2021.

[13] C. A. Silvera Delgado, "Modeling the interaction between lymphatic capillaries and interstitium," Master's thesis, Politecnico

di Torino, 2022.
[14] COMSOL, *Porous Media Flow Module User's Guide 5.6*, 2020.
[15] W. M. Lai, V. C. Mow, and V. Roth, "Effects of Nonlinear Strain-Dependent Permeability and Rate of Compression on the Stress Behavior of Articular Cartilage," *Journal of Biomechanical Engineering*, vol. 103, no. 2, pp. 61–66, 05 1981.
[16] M. Holmes and V. Mow, "The nonlinear characteristics of soft gels and hydrated connective tissues in ultrafiltration," *Journal of Biomechanics*, vol. 23, no. 11, p. 1145–1156, 1 1990.
[17] M. Ramazanilar and A. Mojra, "Characterization of breast tissue permeability for detection of vascular breast tumors: An in vitro study," *Materials Science and Engineering: C*, vol. 107, p. 110222, 2020.
[18] M. L. Palmeri, B. Qiang, S. Chen, and M. W. Urban, "Guidelines for finite-element modeling of acoustic radiation force-induced shear wave propagation in tissue-mimicking media," *IEEE Transactions on Ultrasonics, Ferroelectrics, and Frequency Control*, vol. 64, no. 1, pp. 78–92, 2017.
[19] K. Nightingale, "Acoustic radiation force impulse (arfi) imaging: A review," *Current Medical Imaging Reviews*, vol. 7, no. 4, p. 328–339, 1 2011.
[20] F. Q. Jin, A. E. Knight, C. T. Paley, L. S. Pietrosimone, L. D. Hobson-Webb, K. R. Nightingale, and M. L. Palmeri, "An open-source radon-transform shear wave speed estimator with masking functionality to isolate different shear-wave modes," in *2022 IEEE International Ultrasonics Symposium (IUS)*, 2022, pp. 1–4.
[21] R. M. Sigrist, J. Liau, A. E. Kaffas, M. C. Chammas, and J. K. Willmann, "Ultrasound elastography: Review of techniques and clinical applications," *Theranostics*, vol. 7, no. 5, p. 1303–1329, 2017. [Online]. Available: http://thno.org/v07p1303.pdf
[22] J.-L. Gennisson, M. Rénier, S. Catheline, C. Barrière, J. Bercoff, M. Tanter, and M. Fink, "Acoustoelasticity in soft solids: Assessment of the nonlinear shear modulus with the acoustic radiation force," *The Journal of the Acoustical Society of America*, vol. 122, no. 6, pp. 3211–3219, 12 2007.

Contents

List of Figures

List of Tables

List of Acronyms

ARF Acoustic Radiation Force.

ARFI Acoustic Radiation Force Impulse.

ECM Extracellular Matrix.

IFP Interstitial Fluid Pressure.

MRE Magnetic Resonance Elastography.

MRI Magnetic Resonance Imaging.

ROI Region Of Interest.

SE Strain Elastography.

SWE Shear Wave Elastography.

SWV Shear Wave Velocity.

US ultrasound.

USE Ultrasound Elastography.

List of Symbols

Shear Wave and Solid Mechanics

σ	Stress	Pa
ε	Strain	-
ε_{vol}	Volumetric strain	-
Λ	Isotropic stretch	-
E	Young's modulus	Pa
G	Shear modulus	Pa
μ	Shear modulus	Pa
K	Bulk modulus	Pa
c_l	Longitudinal wave velocity	m/s
c_s	Shear wave velocity	m/s
ρ	Density	kg/m^2
ν	Poisson's ratio	-
W	Strain energy function	J

Fluid and Poroelasticity Mechanics

P	Fluid pressure	Pa
q	Fluid flow	m/s
v_f	Fluid velocity	m/s
μ	Dynamic viscosity	$Pa \cdot s$
k	Intrinsic permeability	m^2
$\mathcal{K}$	Hydraulic conductivity	$m^4/(N \cdot s)$
M	Exponential permeability parameter	-
ϕ	Porosity	-
θ	Fluid content variation	-

1 Introduction

Tumours, and other biological tissues, can be described by a poroelastic material consisting of a porous solid matrix and (interstitial) fluid between the pores. Solid tumours represent more than 85% of all human cancers [75]. In (malignant) solid tumours, the pressure of the interstitial fluid is elevated [70, 89]. This creates an outward fluid flow away from the tumour, which limits the amount of therapeutic drugs that reaches the tumour centre through convection [30]. In fact, the drug distribution is concentrated at the periphery of the tumour while 90% of the tumour volume receives very little to no drugs [75]. The Interstitial Fluid Pressure (IFP) has therefore been shown to be a valuable marker for both diagnosis and prognosis of many solid cancer types [33, 36].

Accurate and non-invasive measurements of the IFP would be clinically valuable for developing patient-specific and optimized drug delivery strategies and monitor the efficacy of treatments designed to lower the IFP over time [80]. Currently, only invasive techniques exist. However, Shear Wave Elastography (SWE) provides an alternative. This non-invasive technique is used today to measure tissue stiffness based on ultrasound. By hypothesizing that the measured tissue stiffness is not only dependent on the stiffness of the porous solid matrix but also affected by the IFP, SWE is a promising technique to measure the IFP indirectly.

Therefore, the goal of this Master's thesis is to explore and assess through computational modelling in which way SWE measurements are affected by IFP. Numerical models have the advantage of allowing to study the influence of different parameters on outcomes separately, and may provide novel insights that would be difficult to acquire through *in vivo* or *ex vivo* experiments. This thesis builds upon the work performed by Kristyna Holkova in her Master's thesis [31]. She successfully demonstrated a correlation between IFP and the Shear Wave Velocity (SWV) measured during SWE in *ex vivo* experiments on a chicken breast. However, no relationship was observed between the IFP and computationally obtained SWV. The model for healthy biological soft tissue that she developed is improved in this thesis in order to observe the effect of IFP on the SWV. Additionally, it is extended to include a tumour mass and examine a more relevant clinical scenario.

Part I

Literature Study

2 Interstitial Fluid Pressure (IFP)

2.1 The Interstitium and Interstitial Fluid

The interstitium, which is the space between cells and blood capillaries as shown in Figure 2.1, accounts for roughly one-eight of the total body weight [8]. It consists of the extracellular matrix (ECM), which contains the interstitial fluid and structural elements such as collagen fibres, elastin fibres, proteoglycans and glycosaminoglycans [78]. As water binds to certain elements in the ECM, the interstitial fluid acquires a hydrogel-like structure. Human bodies contain at least three times more interstitial fluid volume than blood [22]. The interstitial fluid brings oxygen and nutrients from blood capillaries to cells, removes their waste products (through lymphatic drainage) and allows cells to exchange information through molecular signals. [22, 49, 78]

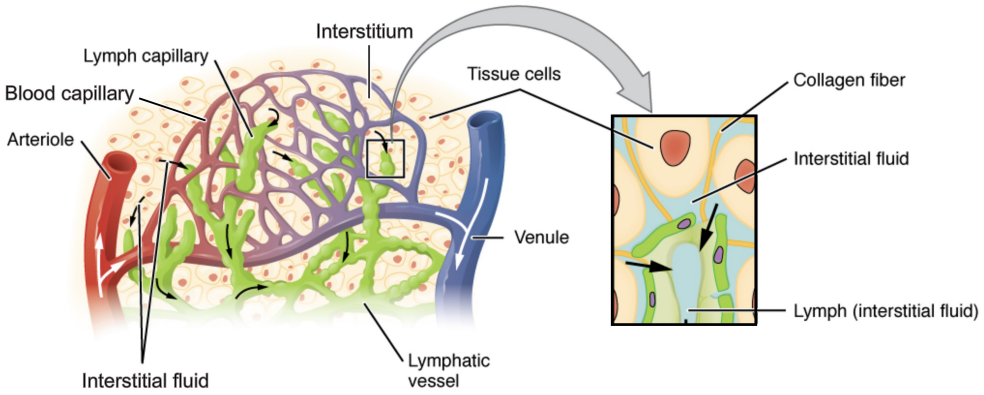

Figure 2.1: The interstitium is the space between cells and blood capillaries and contains interstitial fluid. Adapted from [77].

2.2 Poroelasticity of Biological Tissues

As the ECM consists of structural elements and the interstitial fluid, it can be represented by a poroelastic tissue, where deformation of a solid matrix induces fluid flow and vice-versa. Similarly to a wet sponge, when a poroelastic material is compressed, fluid is forced out of the material while its pores get compressed.

2.3 Transcapillary Flow

The exchange of fluid between the capillaries and the interstitium is called the transcapillary flow. In healthy tissues, the fluid flows from the arterial end of capillaries to the interstitium and is reabsorbed at the venous end or eliminated through lymphatic drainage [22]. The net filtration pressure across the capillary wall is driven by the Starling forces, which are the hydrostatic and colloid osmotic pressures in both the capillaries and the interstitial fluid [30].

Hydrostatic pressures refer to the force exerted by a fluid against a wall. In the capillaries, the hydrostatic pressure is positive and corresponds to the blood pressure generated by the heart, pushing fluid into the interstitium. In the interstitium, it is (generally) negative due to, e.g., lymphatic drainage, pushing fluid out of the interstitium and into the lymphatics. [60]

Osmotic pressures occur when two solutions with different concentrations are separated by an impermeable membrane. The capillary wall is impermeable to plasma proteins, giving rise

to a lower colloid osmotic (or oncotic) pressure in the interstitium, pulling water out of the interstitium and into the capillaries [60].

The direction and rate of fluid exchange of the transcapillary flow is determined by a balance between the hydrostatic pressure gradient, pushing fluid into the interstitium, and the colloid osmotic pressure gradient, pushing fluid into the capillaries as illustrated in Figure 2.2. This interplay can be summarised using the following equations:

$$P_{net} = (P_c - P_{if}) - (\Pi_c - \Pi_{if}) \tag{2.1}$$

$$J = K \cdot P_{net} \tag{2.2}$$

where P_{net} is the net filtration pressure, P the hydrostatic pressure, Π the colloid osmotic pressure, J the transcapillary flow, and $\mathcal{K}$ the vascular permeability coefficient. Subscripts c and if refer to the capillaries and interstitial fluid, respectively. Thus, the transcapillary flow is positive for flows into the interstitium. [30, 60]

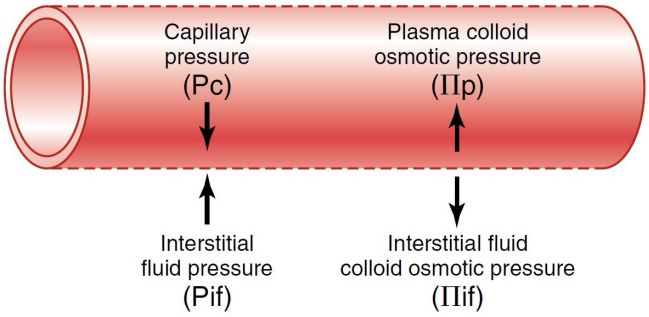

Figure 2.2: Interplay of Starling forces that regulate transcapillary flow. [28]

Average values for the Starling forces in human capillaries and interstitium and the resulting net filtration pressure can be found in Table 2.1. The average net filtration pressure is slightly positive, indicating that the transcapillary flow is directed from the capillaries toward the interstitium.

Table 2.1: Average values for the Starling forces in human capillaries and interstitium. [30]

P_{net}	P_c	P_{if}	Π_c	Π_{if}
1 to 3 $mmHg$	20 $mmHg$	-3 to -1 $mmHg$	28 $mmHg$	8 $mmHg$

2.4 Interstitial Fluid Pressure (IFP) in Healthy and Cancerous Tissues

The Interstitial Fluid Pressure (IFP), previously referred to as the hydrostatic pressure of the interstitial fluid, varies slightly depending on the location in the human body. In general, it is a few millimetres of mercury around the atmospheric pressure [70]. Solid tumours, however, are characterized by increased IFP [30, 70, 80]. Typical values from 10 to 40 $mmHg$ have been reported in various solid tumours, such as in head, neck, breast, and cervical cancer, with highest recordings going up to 100 $mmHg$ in malignant melanomas [70]. The tumour IFP is distributed uniformly throughout the centre with a rapid decrease towards the edges [30].

Some of the plausible underlying processes of increased IFP in tumours are described below and illustrated in Figure 2.3. Solid tumours require the formation of new blood vessels, i.e.,

angiogenesis, to provide sufficient oxygen and nutrients for growth. These vessels are often hyperpermeable (leaky), irregular, tortuous, and compressed by surrounding proliferating cells, causing inefficient blood flow and allowing more fluid and plasma proteins to diffuse into the interstitium. This reduces the capillary hydrostatic pressure and increases the IFP. Furthermore, a lack of lymphatic vessels limits drainage of the excess fluid and proteins, and the increased presence of inflammatory cells contributes even more to the higher tumour IFP. More precisely, the IFP is uniformly elevated throughout the tumour, with a steep decrease in the periphery where functional lymphatics are available. [3, 21, 30, 52, 72]

Numerical models have allowed to identify additional parameters that influence IFP, such as tumour size and shape, tumour vascular heterogeneity, and hydraulic conductivity of the interstitium. The latter represents the ease of fluid flow through the porous matrix and depends on the tissue's permeability, degree of saturation, fluid density, and fluid viscosity. [70]

The increased IFP cannot be (completely) compensated for through volume expansion, as the tumour tissue is stiffer due to a denser network of collagen fibres in the ECM. This likely explains the persistent elevated IFP. [30]

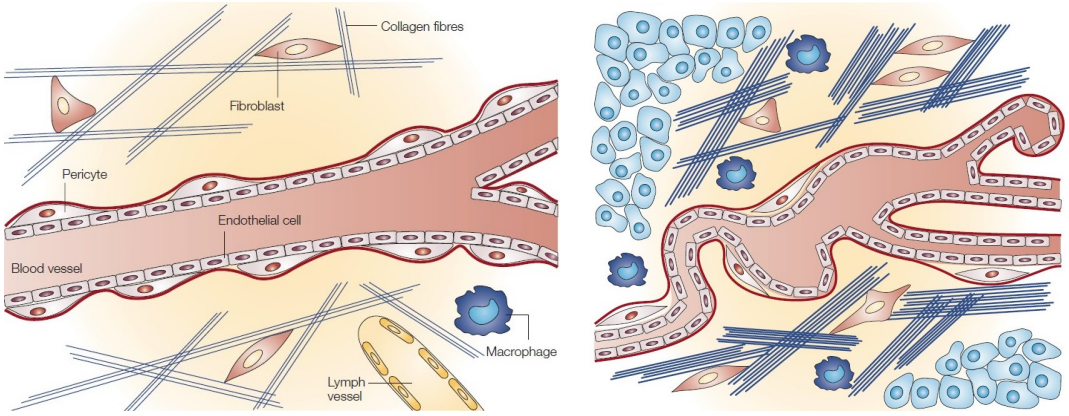

(a) Healthy tissue **(b)** Tumour tissue

Figure 2.3: Differences between healthy and tumour tissues that impact interstitial fluid pressure (IFP). Blood vessels in tumours are often hyperpermeable, irregular, tortuous, and compressed by surrounding proliferating cells, causing inefficient blood flow and allowing more fluid and plasma proteins to diffuse into the interstitium. The lack of lymphatic vessels limits drainage of the excess fluid and proteins. The tumour tissue also contains more inflammatory cells. Combined, these structural changes increase the IFP in the tumour. The increased IFP cannot be compensated through volume expansion, as the tumour tissue is stiffer due to a denser network of collagen fibers in the ECM. [30]

2.5 Impact of Increased Tumour IFP

Many drugs that are used in cancer therapy are comprised of compounds with high molecular weight that cannot be transported from the bloodstream to the interstitium through diffusion. Instead, their transportation occurs through convection. However, the increased tumour IFP induces a pressure gradient between the tumour and the surrounding normal tissue which creates a fluid flow away from the tumour. Therefore, a lower amount of therapeutic drugs reach the tumour centre and drug distribution is heterogeneous within the tumour, limiting the therapeutic efficacy. [30, 36]

Increased tumour IFP is therefore a barrier to cancer therapy and has been associated to poor prognosis to treatment, such as chemotherapy and radiation therapy, and higher risk of recurrence and distant metastases. Conversely, a progressive lowering of IFP in various cancer types has been observed in patients who respond positively to therapy. Moreover, compounds

that reduce the tumour IFP have been shown to improve the efficacy and therapy by enabling more efficient uptake of therapeutic drugs. [36, 80]

Therefore, tumour IFP has been established as a valuable diagnostic and prognostic marker, and predictor of clinical response for various cancer types [33, 36]. For example, IFP is the prominent prognostic indicator of survival for patients suffering from cervical cancer [21].

2.6 Clinical Importance of IFP Measurements

The aforementioned arguments highlight the clinical potential of accurate *in vivo* IFP measurements. The measurements could be employed for [80]:

- Identifying solid tumours with high IFP.
- Designing optimized treatment plans taking into account the constraining impact of increased IFP.
- Monitoring the efficacy of treatments aimed at reducing the IFP to facilitate the transport of therapeutic drugs towards the tumour.

Additionally, IFP measurements would be valuable in other pressure-related disorders such as hydrocephalus (build-up of cerebrospinal fluid in the ventricles of the brain [50]), stroke (impaired interstitial fluid drainage [2]), and oedema (excessive build-up of fluid in the interstitium [30]) [80]. These applications are outside the scope of this thesis.

2.7 IFP Measurement Methods

Despite their clinical potential, IFP measurements have not been implemented much in oncology practice. This is because invasive techniques (requiring needle insertion) were required until recently. In general, these are uncomfortable for the patient, destructive to the tissue thereby limiting the accuracy of the pressure estimation, constrained to tumours located superficially and restricted to measurements at discrete locations [6, 36, 70, 80].

Alternatives to invasive methods, that measure pressure directly, are imaging- or elastography-based methods. These approaches estimate the pressure indirectly. They could overcome the limitations associated with invasive techniques and expedite the adoption of IFP measurements for clinical decision-making in oncology, leading to improved cancer treatment and outcomes [36].

The following sections will elaborate on both the direct and indirect methods. A more in-depth explanation of the techniques described below is provided in [70] and an overview of their (dis)advantages is found in Table 2.2.

2.7.1 Invasive Techniques

2.7.1.1 Wick Catheter and Wick-In-Needle

A wick catheter (illustrated in Figure 2.4) is filled with saline and contains a protruding absorbent wicking material such as nylon thread. A large cannula is necessary to insert the catheter into the skin and a needle and plastic sheath are used to advance the wick deeper into the tissue, after which they are retracted. A pressure transducer is connected to the catheter and measures the equilibrium pressure between the saline and interstitial fluid. The wick-in-needle technique (illustrated in Figure 2.4) is similar apart for the fact that the wick is now encased within a fine needle that contains an elongated side hole to allow contact between the wick and interstitium. These techniques have the advantage of being reproducible and are therefore most commonly used. [6, 30, 70, 85]

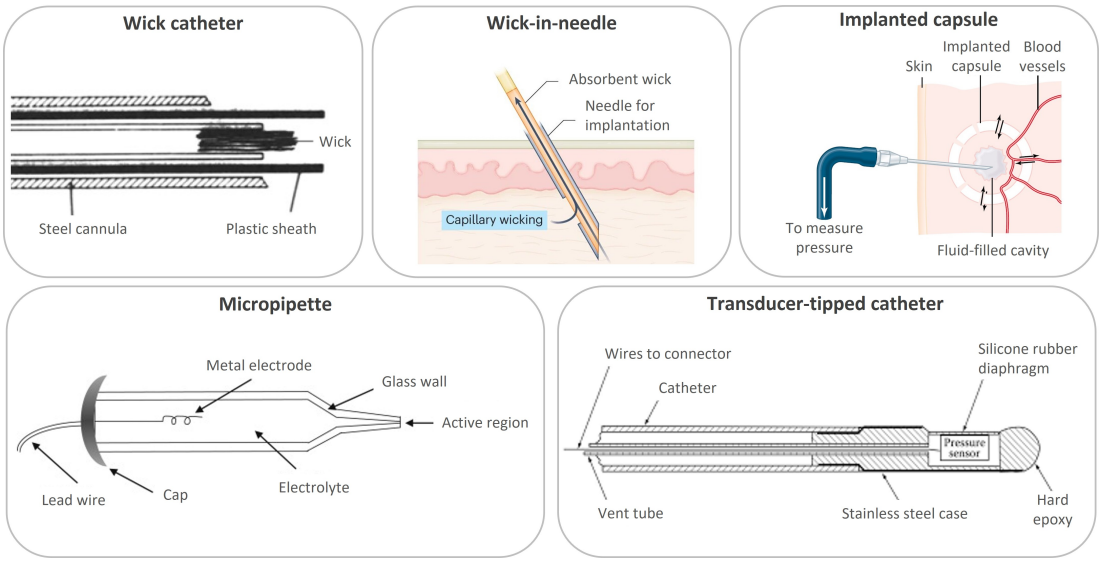

Figure 2.4: Invasive methods to measure IFP. Figures adapted from [85] (wick catheter), [22] (wick-in-needle), [29] (implanted capsule), [9] (micropipette), [38] (transducer-tipped catheter).

2.7.1.2 Servo-Controlled Micropipette

When using a servo-controlled micropipette (illustrated in Figure 2.4), the tissue is punctured with a sharpened saline-filled microscopic glass pipette. A servo-controlled counterpressure is applied to the pipette in order to avoid a change in electrical impedance that occurs when interstitial fluid enters the pipette. The counterpressure is equal to the interstitial fluid hydrostatic pressure acting on the tip of the pipette and can be gauged by a pressure transducer. The pressure estimations of this method are more reliable compared to the wick-in needle technique, owing to the minimal tissue damage of the technique due to the smaller tip. Nevertheless, glass tubes are fragile and pressure assessment is limited to tissues located at a depth of up to 1 mm from the surface. [6, 30, 70, 85]

2.7.1.3 Transducer-Tipped Catheter (Millar)

The transducer tipped catheter (illustrated in Figure 2.4) is a miniature transducer within a needle, which can be retracted after being introduced into the tissue. Calibration of the transducer is necessary both prior to and following each use to achieve accurate IFP measurements. Unfortunately, the technique is expensive and the reading might be biased by the solid stress in the tissue as well. [55, 70]

2.7.1.4 Implanted Capsules

Chronic measurement methods also exist, and involve implanting hollow perforated or porous capsules (illustrated in Figure 2.4) into the tissue of interest several weeks before measurements can start. Subsequently, the pressure of the interstitial fluid inside the capsule is assessed using a catheter or needle, linked to a pressure transducer. However, these methods are highly damaging to the tissue and are restricted to superficially located tissues and non-urgent measurements. Additionally, the accuracy of the readings is compromised because of the sensitivity to changes in vascular pressure or the colloid osmotic pressure of the interstitial fluid. [70, 85]

2.7.2 Non-Invasive Techniques

There are two approaches for indirectly estimating the IFP: one measures fluid flow through dynamic imaging, while the other involves elastography to assess the stiffness of the tissue [70].

Therefore, the indirect methods measure a quantitative value first, from which the IFP can be deduced through a scaling factor or computational algorithm [36]. These methods are still in the research phase and are not implemented into clinical practice for IFP assessment.

2.7.2.1 Dynamic Imaging-Based

In literature, most dynamic imaging methods for IFP assessment are based on Magnetic Resonance Imaging (MRI). These include Dynamic Contrast Enhanced (DCE), Diffusion Weighted (DW), and Convection MRI. These techniques are explained briefly below, a more extended explanation can be found in [70].

- Dynamic Contrast Enhanced MRI
  In DCE MRI, a contrast agent is administered and pre- and post-injection MRI scans are compared. The signal intensity of the contrast agent over time is related to the tissue perfusion and can be used to estimate IFP through curve analysis or fitting to pharmacokinetic compartment models. [70]
- Diffusion-Weighted MRI
  DW MRI allows to assess quantitatively the diffusion path of water molecules and yields a map of apparent diffusion coefficients. These values have shown to be inversely correlated with IFP. [36, 70]
- Convection MRI
  Finally, convection MRI measures interstitial fluid velocity through a specific sequence. It can be converted to IFP through Darcy's law. The added value is that it provides additional information, namely, both 3D pressure and fluid-velocity maps. However, the acquisition is slow, limiting its clinical potential. [36, 70]

2.7.2.2 Elastography-based

The last non-invasive approach, which forms the subject of this Master's thesis, is founded on elastography. This technique employs medical imaging modalities, such as ultrasound (US) or MRI to obtain stiffness maps of tissues, also known as elastograms. The following chapter describes this technique and its relevance for pressure estimations.

Table 2.2: Comparison of methods to measure interstitial fluid pressure (IFP). Table adapted from [70].

Technique	Disadvantages	Advantages
Direct methods		
Servo-controlled micropipette	Only superficial measurements possible (max 1 mm), fragile, breaks easily, invasive	Minimally invasive
Wick catheter	Vulnerable to clotting, tissue trauma due to large cannula (invasive)	Rapid
Wick-in-needle	Requires custom needles with side holes, invasive	Rapid, minimal tissue trauma
Capsule implantation	Considerable trauma and wound healing response (invasive), slow and superficial measurements	Measures only fluid pressure
Transducer-tipped catheter	Expensive, tend to measure total tissue pressure (IFP plus solid stress), invasive	Minimal tissue trauma, rapid and simple
Indirect methods		
Dynamic contrast MRI	Requires complex models, safety and patient considerations, expensive	Non-invasive, measures only fluid pressure
Convection MRI	Slow acquisition, safety and patient considerations	Non-invasive, requires less complex models, no contrast agent required, measures only fluid pressure
Diffusion-weighted MRI	Uncertainty, safety and patient considerations	Non-invasive, no contrast agent required, measures only fluid pressure
Ultrasound-based elastography	Limited field of view, uncertainty	Non-invasive, rapid and cheap, no contrast agent required
MR based elastography	Uncertainty	Non-invasive method, no contrast agent required

3 Shear Wave Elastography (SWE)

3.1 Elastography

The stiffness of tissues has been known to be correlated to tissue pathologies and is therefore an important biomarker. For example, the stiffness is increased in most tumours or in liver tissue affected by liver fibrosis [73]. Assessing and quantifying changes in tissue stiffness can therefore improve the diagnosis of certain tissue pathologies. Palpation is the oldest technique used by clinicians to qualitatively assess changes in tissue stiffness through physical examination. [11, 56].

Today, several methods based on elastography have been developed. They are more quantitative, less operator-dependent and allow to assess tissues that are not located superficially. Elastography is a non-invasive technique employing medical imaging modalities to estimate the stiffness of tissues. More specifically, a mechanical excitation is applied and the resulting tissue displacement measured. Stiffer tissues will deform less for the same mechanical excitation. [11, 56]

Ultrasound (US) and Magnetic Resonance Imaging (MRI) are the main imaging modalities used in elastography. Mechanical excitation of the tissue is generated by an actuator in Magnetic Resonance Elastography (MRE) and through internal or external compression in Ultrasound Elastography (USE) [70]. US-based methods generally have the advantage of being faster, less expensive and more widely available, including at bedside, than MRE [11, 73]. On the other hand, MRI-based methods are not limited by gas and bone and can thus be used for imaging in e.g., the brain. They have a larger field of view, and higher repeatability and reproducability. MRE is also able to detect tissue displacement in 3D, whereas this can only be detected in 1D, along the direction of the US beam, in US-based methods. [11, 70]

The USE techniques and mechanics will be explained in more detail in section 3.3. Shear Wave Elastography (SWE) is a subtype of USE and forms the the primary emphasis of this thesis. While elastography is traditionally designed to acquire the elastic or Young's modulus of tissues, this thesis focuses on the indirect assessment of IFP through stiffness measurements from USE instead. The following section describes the theory underlying this concept.

3.2 Stiffness and Total Tissue Pressure

As mentioned in the previous section, the stiffness in most tumours is elevated. The stiffness of tissues is defined as the resistance to deformation. It is commonly described by the elastic modulus, which is the ratio of the stress over the strain with units of N/m^2 or Pa [12]. This is an intrinsic property of the material that is not affected by its physical dimensions [70]. However, stresses and strains are difficult to determine in clinical practice. The structural stiffness is therefore often used instead, which is also dependent on the geometry and boundary conditions besides the intrinsic material stiffness [12]. Stiffness is mainly influenced by the composition and organization of the ECM. More precisely, increased collagen deposition and crosslinking of ECM constituents in tumours lead to the densification of the ECM, which results in an augmentation of tissue stiffness [52, 57].

Tensile and compressive forces are present in the tumour. These solid stresses are determined by the solid components of the tumour, such as the ECM, cancer cells, collages fibres, and hyaluronan acid gel. Solid stress is increased in many tumours, due to cell proliferation, matrix deposition, cell contraction, and abnormal growth. Therefore, it can be influenced by both the ECM and cells, whereas the tumour stiffness is predominantly affected by solely the ECM. [52, 57]

Besides the solid stress (SS), the tissue is also affected by the IFP for reasons mentioned in section 2.4. The total tissue pressure (TTP) in a tumour is therefore the sum of the solid stress (SS) and interstitial fluid pressure (IFP) [36, 70]:

$$TTP = SS + IFP \tag{3.1}$$

Importantly, the IFP and matrix stiffness are tightly linked and interdependent: an increase in IFP results in tissue deformation, a modification in strain distribution, and an elevation in stiffness [70]. As highlighted in [40], the contribution of IFP to the tumour stiffness might resemble the effect of the air pressure within a basketball, which feels harder when it is more inflated. The growth of tumours results in an elevation of both solid and fluid pressures, with the latter contributing more significantly to the overall tissue pressure. As a result, the tissue undergoes deformation, leading to a change in stiffness proportional to the total tissue pressure. This principle has led to the development of elastography-based techniques that enable the estimation of tumour IFP. [70]

The effect of IFP on drug delivery was already discussed in section 2.5. The elevated solid stress and stiffness also influence drug delivery, as summarised in Figure 3.1.

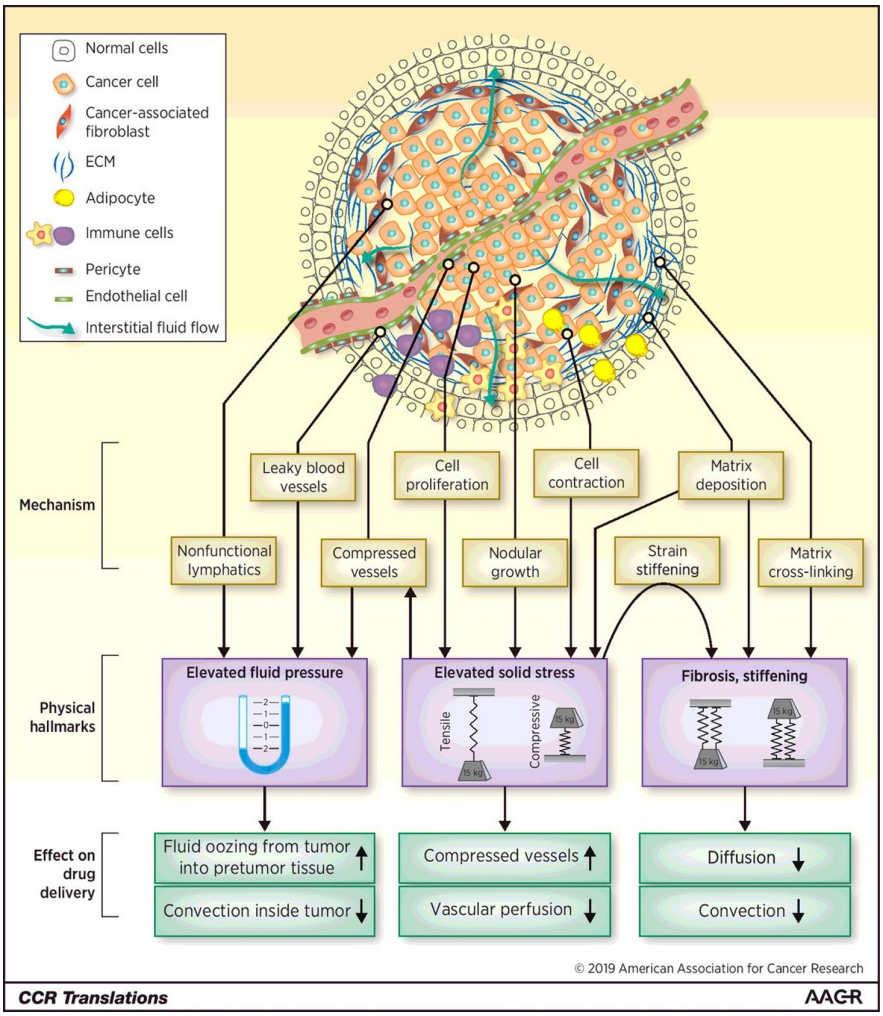

Figure 3.1: Mechanisms in tumours that lead to altered drug delivery. [52]

3.3 Ultrasound Elastography (USE)

3.3.1 Physics

3.3.1.1 Hooke's Law

Hooke's law describes elasticity in materials that are linearly elastic and experience deformations that are not influenced by time (i.e., no poroelasticity or viscoelasticity):

$$\sigma = \Gamma \cdot \varepsilon \tag{3.2}$$

where σ is the stress or force per unit area (in units of N/m^2 or Pa), ε is the strain or expansion per unit length (dimensionless) and Γ is the elastic modulus that correlates the stress and strain (in units of N/m^2 or Pa). Materials possessing a higher elastic modulus will exhibit greater resistance to deformation and thus enhanced stiffness.

Three different elastic moduli can be defined dependent on the method of deformation: the Young's modulus (E), shear modulus (G), and bulk modulus (K). The Young's modulus is used to relate normal stresses (σ_n) and strains (ε_n), the normal being perpendicular to the surface, and is measured during uniaxial loading. The shear modulus relates shear stresses (σ_s) and strains (ε_s), shear being tangential to the surface, and is measured during simple shear loading. Finally, the bulk modulus is used when a normal inward force or pressure (σ_B) results in a bulk strain or change in volume ε_B [12, 73]. This is summarised in the following equations and Figure 3.2 [12]:

$$\sigma_n = E \cdot \varepsilon_n \tag{3.3a}$$
$$\sigma_s = G \cdot \varepsilon_s \tag{3.3b}$$
$$\sigma_B = K \cdot \varepsilon_b \tag{3.3c}$$

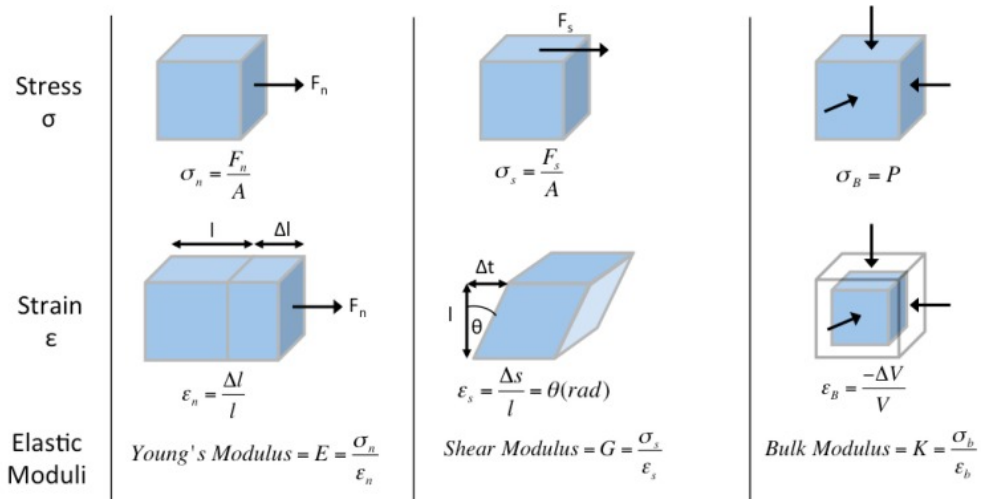

Figure 3.2: Deformation models in USE. Hooke's law relates the stress and strain through the elastic modulus in linearly elastic materials and time-independent deformations. Depending on the type of deformation, different elastic moduli can be defined. [73]

3.3.1.2 Wave Propagation

Different types of waves can be distinguished in US. The longitudinal and shear waves are described here and are illustrated in Figure 3.3. In a longitudinal wave, particle displacement occurs in the same direction as the wave propagation. Shear waves, on the other had, propagate

perpendicularly to the particle displacement. The velocity of the longitudinal (c_l) and shear (c_s) wave propagation are described by the following equations:

$$c_l = \sqrt{\frac{K + \frac{4}{3}G}{\rho}} \tag{3.4a}$$

$$c_s = \sqrt{\frac{G}{\rho}} \tag{3.4b}$$

where ρ is the material density (in units of kg/m^3), c_l is the longitudinal wave velocity ($\approx$ 1540 m/s in soft tissues), and c_s the shear wave velocity ($\approx 1 - 10$ m/s in soft tissues) [73].

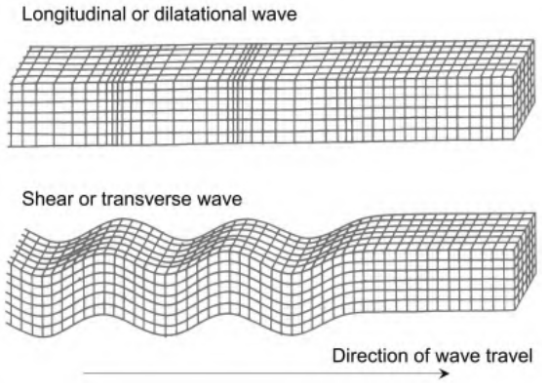

Figure 3.3: In a longitudinal wave, particle displacement occurs in the same direction as the wave propagation. Shear waves, on the other had, propagate perpendicularly to the wave propagation. [11]

The Young's and shear modulus are related to each other through the dimensionless Poisson's ratio (ν):

$$E = 2(1 + \nu)G \tag{3.5}$$

By substituting the previous equation in Equation 3.4b, the relationship between the Young's modulus and shear wave velocity can be obtained:

$$c_s = \sqrt{\frac{E}{2\rho(1 + \nu)}} \tag{3.6}$$

In case of an incompressible material, $\nu = 0.5$, and the previous equation can be simplified to:

$$c_s = \sqrt{\frac{E}{3\rho}} \tag{3.7}$$

The equations presented in this section serve as the foundation for stiffness estimation in elastography.

3.3.1.3 Advantage of Shear Wave Analysis

The variation of bulk and shear moduli across different tissues in the human body is depicted in Figure 3.4. Notably, the shear modulus exhibits a much broader range of values than the bulk modulus, as it spans several orders. Consequently, imaging of the shear wave propagation, which is determined by the shear modulus through Equation 3.4b, enables better differentiation

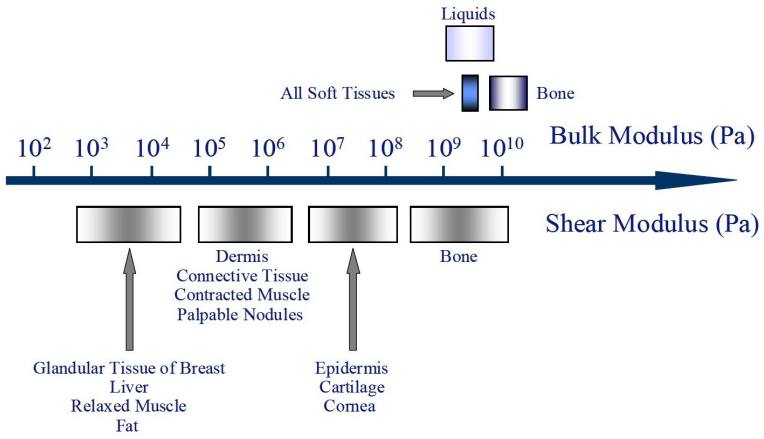

Figure 3.4: Variation in bulk and shear modulus for different tissues in the body. The shear moduli in the body span over a much larger range than the bulk moduli. [59]

between different tissue types compared to longitudinal wave propagation, which is governed by the bulk modulus through Equation 3.4a. Additionally, as explained in the previous section, shear waves propagate much slower than longitudinal waves. For this reason, shear wave analysis can be conducted with a smaller field of view and/or lower frame rate. [11]

3.3.2 Techniques

3.3.2.1 Classification Methods

As mentioned in the introduction on elastogrpahy in section 3.1, elastography-based techniques measure the displacement resulting from a mechanical excitation on the tissue. This excitation can be either (quasi-)static, involving a constant compressive stress on the tissue, or dynamic, where time-varying (transient) or oscillatory (harmonic) forces excite the tissue. Moreover, the excitation can be external, where a compression force is applied on top of the skin, or internal, which results from either physiological (e.g., cardiovascular or respiratory) motion or a forced internal motion induced by remote palpation (i.e., an acoustic radiation force). [11]

Two main USE types can be distinguished by considering the measured physical quantity: strain imaging (qualitative) and shear wave imaging (quantitative)[11]. By taking into account the method of excitation, both techniques can be subdivided again. An overview of USE classification is given in Figure 3.5 and examples of elastograms in clinical applications are shown in Figure 3.6. For a more comprehensive analysis of the various types of USE, the reader is referred to [11].

Strain imaging allows for the qualitative assessment of tissue stiffness by directly estimating the changes in strains observed in the tissue before and after the mechanical excitation. In contrast, shear wave imaging enables the quantitative evaluation of tissue stiffness, such as the elastic or shear modulus, by indirect estimations from reconstructions that take into account the tissue properties. [11]

3.3.2.2 Strain Imaging

Both Strain Elastography (SE) and Acoustic Radiation Force Impulse (ARFI) are types of strain imaging techniques. SE applies external manual compression on the tissue using the US transducer or utilizes internal physiological motion for the mechanical excitation. The former can only be used for superficially located regions such as the breast or thyroid.

In both cases, tissue displacement parallel to the excitation is measured, which allows to estimate the strain. An elastogram can be created by superimposing the strain measurements as

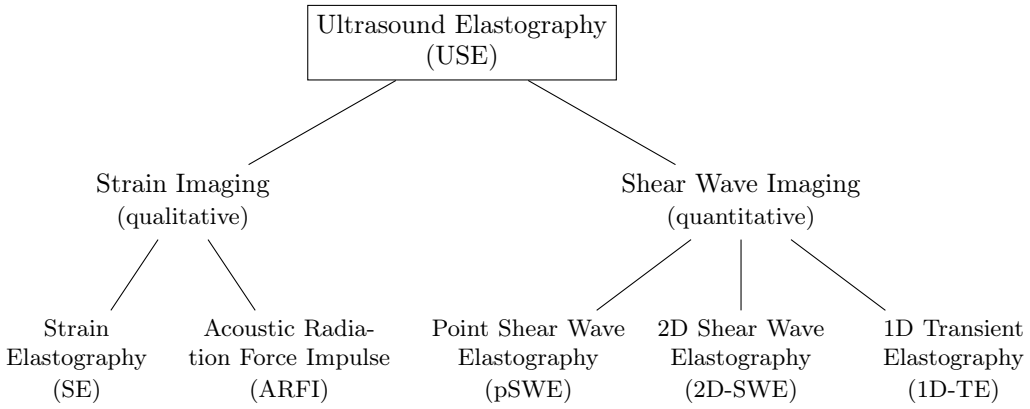

Figure 3.5: Classification of USE.

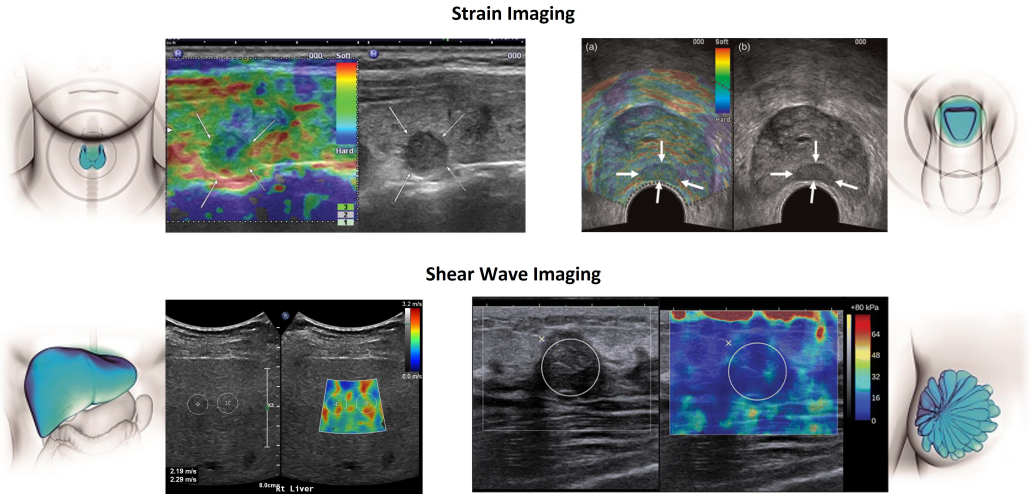

Figure 3.6: Examples of elastograms obtained through strain imaging (top) and shear wave imaging (bottom). Strain imaging provides qualitative results (e.g., soft in red and hard in blue). Shear wave imaging provides quantitative results (e.g., shear wave velocity or estimates of elastic modulus). Illustrations from [81], elastograms adapted from [47] (thyroid), [87] (prostate), [82] (liver), [90] (breast).

a semitransparant color map on top of the conventional US B-mode image. Regions with lower strains compared to the strains in a reference tissue region are characterized by higher stiffness. The strain ratio therefore provides a qualitative stiffness map, for which the applied force does not need to be known, in contrast to quantitative stiffness estimations using Equation 3.3a. [56, 73]

ARFI internally excites the tissue by generating an Acoustic Radiation Force (ARF) with the US transducer. The ARF is a short $(0.1 - 0.5\ ms)$ and high-intensity pulse (i.e., impulsive) that displaces the tissue. Peak tissue displacements are approximately $10 - 20\ \mu m$ [53]. The qualitative elastogram is created in the same way, where stiffer regions are represented by lower strains. [11, 73]

3.3.2.3 Shear Wave Imaging

Three approaches can be distinguished in shear wave imaging: Point Shear Wave Elastography (pSWE), 2D Shear Wave Elastography (2D-SWE), and 1D Transient Elastography (1D-TE). As the names suggest, pSWE provides an average stiffness value at a certain region or point of the tissue, whereas 2D-SWE generates a 2D elastogram of the tissue. They both use an ARF to excite the tissue and measure the shear waves propagating perpendicularly to the

excitation. 1D-TE, on the other hand, excites the tissue with a dynamic mechanical stress that is generated by a vibrating device that is integrated into the US transducer. The waves parallel to the excitation are measured, and decoupling of the longitudinal and shear waves is possible due to the marked difference in propagation velocities between both [45]. [11, 73]

These approaches measure the velocity of the shear wave propagation directly, and by assuming the material is linearly elastic, isotropic, incompressible and the deformation independent on time, it can be converted to a stiffness estimation using Equation 3.7. An overview of the three approaches and their characteristics are represented in Table 3.1.

Table 3.1: Summary of shear wave imaging methods. Table adapted from [73].

pSWE	**2D-SWE**	**1D-TE**
Excitation method		
Dynamic stress by ARFI, perpendicular to the transducer surface, in a single focal location.	Dynamic stress by ARFI, perpendicular to the transducer surface in multiple focal zones.	Dynamic stress by a mechanical vibrating device.
Shear wave measurement plane		
Shear waves measured perpendicular to plane of excitation.	Shear waves measured perpendicular to ARFI application.	Waves measured parallel to excitation and decoupling of longitudinal and shear waves [45].
Stiffness estimation		
Shear wave speed (c_s) reported or converted in Young's modulus (E) to provide quantitative estimate of tissue elasticity.	A near cylindrical shear wave cone is created, allowing real-time monitoring of shear waves in 2D for measurement of SWV or E and generation of quantitative elastograms.	Stiffness estimated along ultrasonic A-line, in a fixed region, neither user adjustable nor image guided.
Visualization		
Operator can use B-mode US to directly visualize and select ROI.	Operator is guided by both anatomical and tissue stiffness information, has real-time visualization of a color box; quantitative elastogram superimposed on a B-mode image stiffness information.	Operator selects imaging area using time-motion ultrasound, based on multiple A-mode lines in time at different proximal locations forming low quality image. The same probe uses A-mode US to measure SWV and E is calculated.
Remarks		
Can be performed on conventional US machine using standard ultrasound probe. Became available in 2008.	Currently newest shear wave imaging method.	First system commercially available. The most widely used and validated technique for assessment of liver fibrosis.
Advantages [56]		
Low operator dependency and strong quantification, less influenced by obesity, ROI can be selected.	Low operator dependency and strong quantification, ROI can be adjusted.	Short exam duration ($< 5min$), easy to perform, highly reproducible.

3.4 Shear Wave Elastography (SWE)

Shear waves propagate perpendicularly to the direction of particle displacement, in contrast to longitudinal waves (see Figure 3.3). They can arise from harmonic or impulsive ($< 1\ ms$) ARF [11]. This thesis will focus on the latter: ARFI driven SWE or SWE in short. This technique can be summarised as follows and is also illustrated in the corresponding Figure 3.7) [11]:

1. Using a conventional ultrasound transducer, a high-intensity pulse or ARF is focused at a particular tissue depth. This induces displacement of the tissue in the direction perpendicular to the transducer surface primarily.
2. The US transducer is then switched into an imaging mode, containing low-intensity acoustic pressure pulses, to measure the resulting tissue displacement. The tissue motion propagates in all directions, away from the focal point. The motion that is perpendicular to the transducer surface with a propagation parallel to the surface, corresponds to the shear waves.
3. A quantitative elastogram, is generated from the shear wave propagation velocity using Equation 3.7. Shear waves propagate faster in stiffer tissues.

One benefit of this method is that conventional US transducers can generate the ARF, without requiring specialized equipment and thus facilitating the incorporation of this technique into clinical practice [11].

Today, SWE is the golden standard for non-invasive detection of liver fibrosis [1]. Furthermore, it is employed in various other clinical applications such as the detection and characterization of lesions in the breast, thyroid, liver, and prostate, and tendon imaging [56, 58].

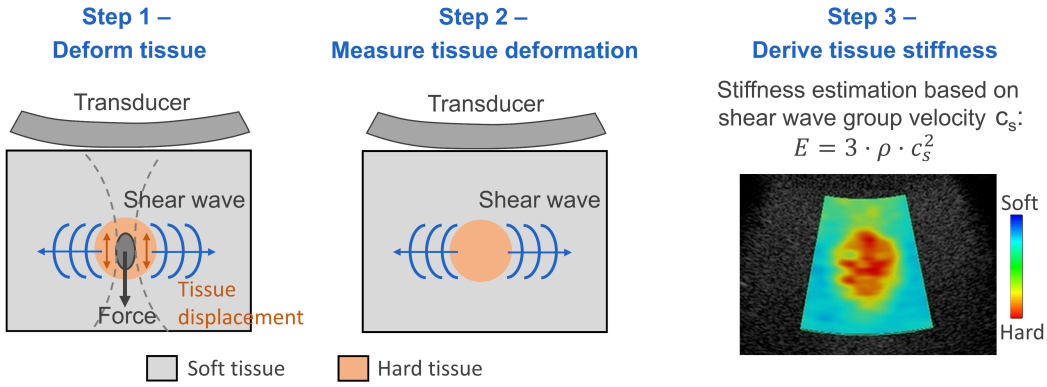

Figure 3.7: Steps in impulsive ARF-driven SWE. Adapted from [11].

3.5 Limitations

A few limitations are associated to USE and US-based systems in general. First, US cannot pass through gas and bone, so MRE has to be used instead for e.g., elastography applications in the brain. Image artifacts, related to shadowing, reverberation, and cluttering also occur in US imaging and free-hand US systems are susceptible to operator-dependent variability. Additionally, accuracy can be compromised in obese patients and deeper lying tissues, as the ultrasound signal is attenuated as a function of depth. Finally, standardization across manufacturer systems and standardization protocols of USE settings and parameters is required to enable comparison between different USE systems and measurements in longitudinal studies. [73]

4 SWE for Assessing IFP

In conventional SWE, the shear wave velocity (SWV) is converted to the Young's modulus using Equation 3.7. In order to apply this equation, the imaged tissue is assumed to have a single solid phase, be linearly elastic, isotropic, incompressible, and bulky (see subsection 3.3.1). Linear elasticity, however, often fails to adequately describe many soft tissues [61]. Additionally, they often consist of a solid and fluid phase, i.e., they are poroelastic.

In literature, laboratory phantom experiments revealed that both porosity and fluid viscosity must be taken into account to convert SWV to elasticity in soft porous materials more accurately [1]. Moreover, significant differences have been found in the estimation of the elastic modulus between *ex vivo* indentation tests and *in vivo* SWE measurements in malignant tumours, strongly suggesting that IFP is a crucial factor influencing SWE in solid tumours [89].

The focus of this thesis is to use computational modelling to examine how the SWV is affected by IFP. Therefore, this chapter investigates various aspects related to the IFP-SWV relationship and poroelasticity.

4.1 Poroelasticity in Soft Biological Tissues

As mentioned in section 2.2, the ECM consists of structural elements and the interstitial fluid. As such, it can be represented by a poroelastic material. The poroelastic or biphasic theory was first developed by Biot in 1941 for soil mechanics [62], and later extended to include anisotropy and viscoelasticity [7].

4.1.1 Governing Equations - Linear Isotropic Poroelasticity

The poroelastic theory described below relies on certain assumptions about the material and its stress-strain relationship [42, 62]. The material is assumed to be isotropic, homogeneous (i.e., requiring sufficiently small pore size to obtain a homogeneous macroscopic behaviour), and to have fully saturated pores (i.e., no presence of gas and infinite supply of fluid), a fully connected pore space and an incompressible solid and fluid phase. Small strains are also assumed, as well as a stress-strain relationship that is linear (described by Hooke's law) and reversible at equilibrium. Finally, gravitational terms are neglected[1].

Under these assumptions, the poroelastic material is governed by three laws [74]: Hooke's law, Darcy's law, and the law of mass conservation. Hooke's law was described in section 3.3.1.1. It relates the stresses in a linear elastic material to the strains through the Young's modulus. Darcy's law describes the fluid flow through a porous medium, driven by a pressure gradient:

$$\mathbf{q} = -\frac{k}{\mu}\nabla\mathbf{P} \tag{4.1}$$

where $\mathbf{q}$ is the fluid flow (units m/s), k the tissue permeability[2](units m^2), μ the fluid dynamic viscosity (units $Pa \cdot s$ or $kg/(m \cdot s)$), and $\nabla\mathbf{P}$ the gradient of the fluid pressure. Bold symbols denote tensors. The permeability describes how easily the fluid can flow through the medium. It depends on the microstructure of the porous solid, such as the porosity, tortuosity, and pore interconnections [24, 42]. In literature, the hydraulic conductivity or permeability $\mathcal{K} = k/\mu$ (units $m^4/(N \cdot s)$) is sometimes used instead. It is important to distinguish it from the intrinsic tissue permeability k [76].

[1] For very soft porous solids, such as certain hydrogels, gravity effects cannot be neglected [23].
[2] If the permeability is anisotropic, $\mathbf{k}$ is a tensor. This work considers isotropic permeability, so k is a scalar.

From the fluid flow, the fluid velocity $\mathbf{v_f}$ (units m/s) can be obtained by considering the porosity ϕ (dimensionless), as only a limited portion of the total volume is available for fluid flow [4]:

$$\mathbf{v_f} = \frac{\mathbf{q}}{\phi} \tag{4.2}$$

Finally, the law of mass conservation (assuming incompressible constituents) ensures that the amount of fluid flowing in or out of the boundaries is met with the appropriate variation of fluid content within the material [42]:

$$\frac{\partial \theta}{\partial t} + \nabla \cdot \mathbf{q} = 0 \tag{4.3}$$

$$\theta = tr(\varepsilon) = \varepsilon_{vol} \tag{4.4}$$

where θ is the variation in fluid content per unit volume of porous media and ε the strain tensor [19]. θ is also referred to as the volumetric strain ε_{vol}, and reflects the dilation or contraction of the porous matrix [16]. In case of an incompressible solid and fluid phase, the variation of fluid content is equal to the variation of pore volume (or porosity):

$$\theta = \phi - \phi_0 \tag{4.5}$$

in which ϕ and ϕ_0 are the current and initial porosity, respectively. Therefore, Equation 4.3 becomes:

$$\frac{\partial \phi}{\partial t} + \nabla \cdot \mathbf{q} = 0 \tag{4.6}$$

4.1.2 Extension to Brinkman Equation

Darcy's law (Equation 4.1) does not consider inertial effects and is only suitable to describe slow flows [16, 41]. Moreover, the non-negligible friction that occurs when the viscous interstitial fluid moves through the interstitium is not taken into account [75]. Therefore, the law can be extended to the Brinkman equation to include additional terms and take into account inertial and viscous forces:

$$\rho \frac{\partial \mathbf{v_f}}{\partial t} + \rho \mathbf{v_f} \cdot \nabla \mathbf{v_f} = -\nabla \mathbf{P} - \frac{\phi \mu}{k} \mathbf{v_f} + \nabla(\mu_{eff} \nabla \mathbf{v_f}) \tag{4.7}$$

where μ_{eff} is the effective viscosity and depends on the dynamic viscosity, but also on the porosity and tortuosity [35]. The left-hand side of the equation represents the inertial forces (due to local acceleration and convection) and the right-hand side the forces acting on the fluid. The first term on the right-hand side is the pressure gradient, the second term a resistance force and the third term is a viscous force (to account for the dissipation of kinetic energy by viscous shear). Body forces such as gravity are neglected. [16, 20, 27, 83]

4.1.3 Extension to Non-Linear Elasticity

Linear elasticity is often insufficient to adequately describe soft biological tissues, especially at large strains. Instead, hyperelastic models are often used to describe these tissues and are defined by a strain energy function W. This function represents the energy that is stored by the material when it undergoes deformation. It thereby relates the displacement and resulting stresses in the tissues and is a scalar function per unit of reference volume. [84]

Different hyperelastic models exist, but only the Ogden model will be described here. It is a simple model considering a homogeneous, isotropic, incompressible material and has shown to fit experimental data of human breast tissue well [84]. The Ogden strain energy function can be defined as follows, taking into account the principal stretches[3] λ_i [84]:

$$W_{Ogden} = \sum_{k=1}^{N} \frac{\mu_k}{\alpha_k}(\lambda_1^{\alpha_k} + \lambda_2^{\alpha_k} + \lambda_3^{\alpha_k} - 3) \tag{4.8}$$

where N is the order of the polynomial, μ_k is the infinitesimal shear modulus[4] (units Pa), and α_k a stiffening parameter (dimensionless). Thus, at higher strains, the material becomes stiffer. The initial shear modulus μ of the material is [84]:

$$\mu = \sum_{k=1}^{N} \frac{\mu_k \alpha_k}{2} \tag{4.9}$$

4.1.4 Strain-Dependent Permeability and Porosity

In the context of small strains, constant porosity and permeability of the porous material are often considered. However, this assumption may not hold true when examining soft biological tissues, particularly in scenarios such as confined compression experiments, involving the compression of the material between permeable plates. By contrast, a more accurate representation would be to consider the porosity and permeability as strain-dependent variables, wherein their values are influenced by the deformation of the solid skeleton. Specifically, when subject to compression, the porous material exhibits a reduction in pore size, resulting in a decreased porosity and diminished permeability.

In biomechanics, cartilage is the most investigated biological poroelastic material [37] and literature about strain-dependency in these tissues is also mainly orientated to articular cartilage [5, 13, 32, 39, 43, 44, 63, 79, 86]. These studies seem to propose different models for the implementation of the strain-dependency in porous media, but they can all be referred back to the formulation originally developed in [39] and later extended in [32]. The strain-dependent porosity and permeability can therefore be written as follows:

$$\phi = \frac{\phi_0 + \varepsilon_{vol}}{1 + \varepsilon_{vol}} \tag{4.10a}$$

$$k = k_0 e^{M\varepsilon_{vol}} \tag{4.10b}$$

where ϕ_0 is the initial porosity, ε_{vol} the volumetric strain (or fluid content variation), k_0 the initial permeability and M an exponential parameter of the permeability. Strain-dependent permeability can be written in terms of the strain, porosity, or hydration. These formulations are mathematically equivalent, but only the formulation with strain can be extended from a scalar to a tensor to include anisotropy and is therefore used here to facilitate the incorporation of anisotropy in future models [32].

Tumour tissues contain more cells and therefore have different porosities and permeabilities compared to their healthy counterparts. In [64], the authors characterised the strain-dependent permeability of healthy and cancerous breast tissue. In cancerous breast tissues, they observed a decrease in the permeability of $40-70\%$ compared to healthy breast tissue. The obtained initial porosity, permeability, and exponential parameter for the tissue specimens are summarized in Table 4.1.

[3] As the strain energy function is defined in function of the principal stretches, the Ogden model is a stretch-based model. Alternative models are based on the invariants of the Cauchy deformation tensor.

[4] The shear modulus μ is different from the dynamic viscosity μ.

Table 4.1: Characterisation of strain-dependent porosity and permeability in breast tissue. A summary is provided of the initial porosity ϕ_0, initial hydraulic permeability $\mathcal{K}_0$, and exponential parameter of the average values within the healthy (H) and cancerous (C) breast tissue specimens. Δ represents the difference between the healthy and tumoral tissue within one specimen. Note that the characterisation was performed using compressive strain, so the opposite of M should be taken when considering the volumetric strain as in Equation 4.10b. Values calculated from [64].

	ϕ_0 (%)			$\mathcal{K}_0$ (10^{-10} $m^4/(Ns)$)			M (-)	
	H	**C**	**Δ**	**H**	**C**	**Δ**	**H**	**C**
Mean	51.5	43.9	8.0	35.6	14.5	24.3	-4.3	-4.1
Median	47.0	42.5	6.5	18.9	10.1	11.0	-4.2	-4.2
Max	71.2	65.1	19.2	187.8	46.4	144.5	-2.9	-1.4
Min	40.0	23.7	-1.5	4.4	0.3	0.9	-5.9	-6.8
Stdev	10.4	9.8	6.1	42.1	12.7	34.4	0.7	1.1

4.2 IFP-SWV Relationship

4.2.1 Our Previous Experimental Work

As mentioned in the introduction (chapter 1), this thesis builds upon the research Kristyna Holkova performed in her Master's thesis [31] last year. In order to explore the correlation between the IFP and SWV, SWE experiments were performed on chicken breasts. These are briefly outlined below.

The experimental setup is illustrated in Figure 4.1. A chicken breast tissue was selected due to its isotropic poroelastic structure. To ensure complete saturation of the tissue, it is immersed in water, while the absorbing US rubbers on the bottom serve to minimise reflections. Two closely positioned needles are inserted into the tissue. One needle is connected to a syringe for controlled fluid insertion, thereby increasing the IFP. The second needle is used for evaluating the resulting pressure. Finally, SWE measurements are performed by placing the US transducer close to the injection point.

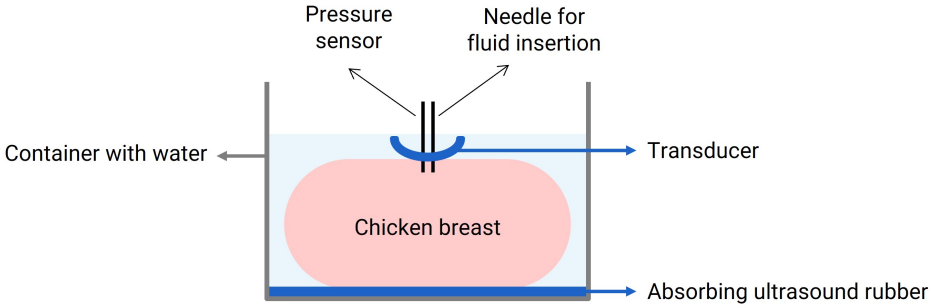

Figure 4.1: Experimental setup for SWE measurements on a chicken breast.

The results of one of the experiments on a chicken breast is shown in Figure 4.2. As can be observed from the figures, a high linear correlation ($R = 0.95$) exists between the IFP and SWV. The SWV was determined through the Radon transformation, which will be explained in section 5.4, and slightly overestimated the SWV compared to manual tracking, showing SWVs in the range of $2.01 - 6.47$ m/s. The analysis of other chicken breast experiments can be found in [31].

4.2.2 Effect of Deformation

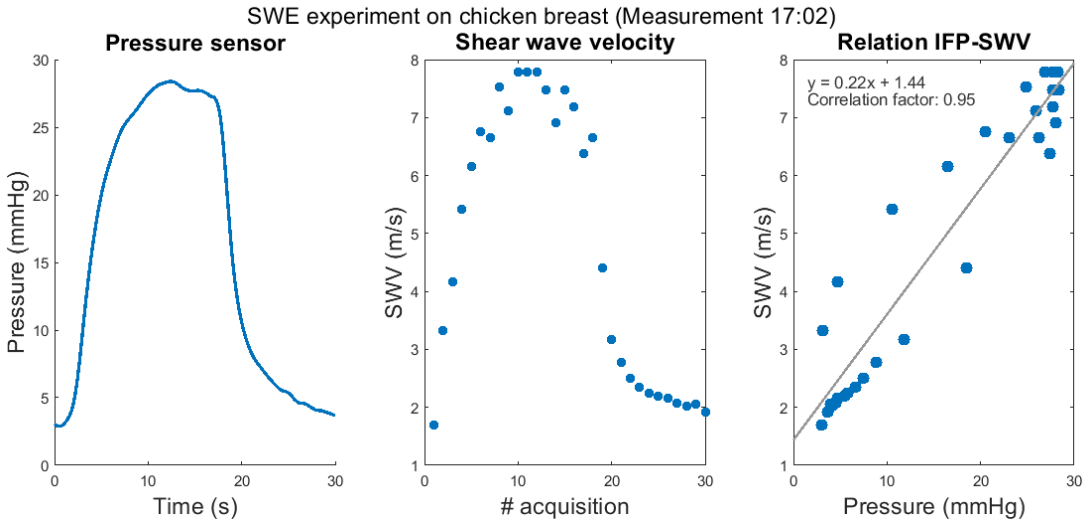

Figure 4.2: Results of a SWE experiment on a chicken breast performed in [31]. Water is injected into the tissue to increase the IFP. The resulting IFP and SWV are measured.

4.2.2.1 *Ex Vivo* Experiments

Increasing stiffness estimations with pressure suggest a nonlinear, e.g., hyperelastic, stress-strain relationship of the tissue. Therefore, shear wave experiments were performed on pressurised hepatic tissue in [66]. The results are shown in Figure 4.3. An increase in SWV with fluid pressure was observed, but only in the unconstrained case, i.e., when the tissue was allowed to expand during pressurization. This indicates that tissue deformation is crucial to observe stiffening with increasing pressure and that a hyperelastic material model can be used for studying this relationship. [66]

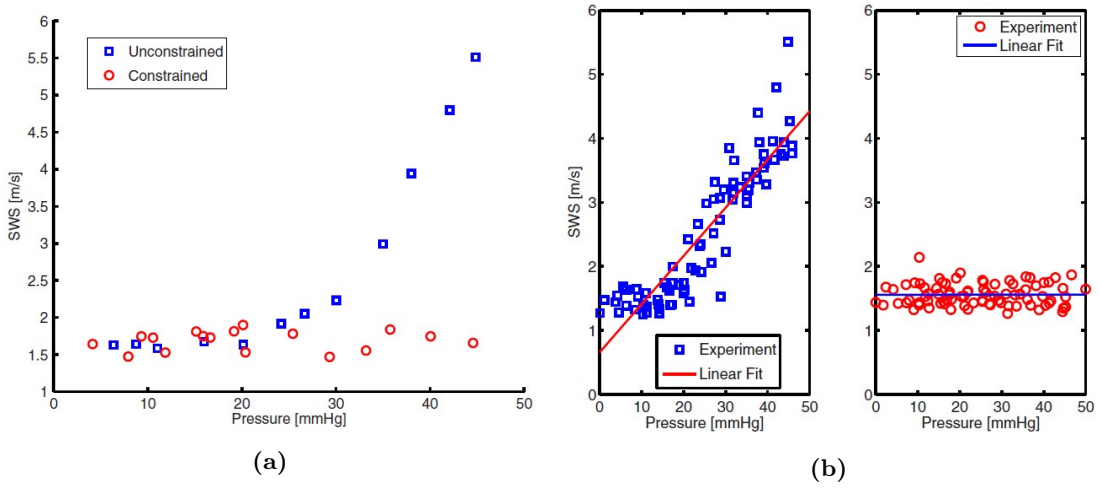

Figure 4.3: Relationship and correlation between the shear wave speed (SWS) and pressure of hepatic tissue during experiments performed by [66]. During pressurization, the tissue is allowed to deform in the unconstrained case and is not allowed to deform in the constrained case. A clear correlation between the SWS and pressure is observed in the unconstrained case. [66]

4.2.2.2 Analytical model

The conventional acoustoelastic theory postulates that the propagation speed in a solid is influenced by prestress, but this theory does not explain the observed phenomenon in the experiments described above. An analytical model was thus derived in [51] for the SWV in an

incompressible isotropic poroelastic material, in which an arbitrary strain function is suitable to describe the solid phase, as long as the decoupled formulation (containing a volumetric and isochoric/volume-preserving contribution) is not used. The resulting formula for the SWV (c_s) is dependent on tissue expansion [51]:

$$c_s = \sqrt{\frac{\tilde{\mu}}{\tilde{\rho}}} \tag{4.11a}$$

$$\tilde{\mu} = 2\frac{W_1}{\Lambda} + 2\Lambda W_2 \tag{4.11b}$$

$$\tilde{\rho} = \rho_{eff,0} - \rho_0^f \frac{i\omega\tau}{1 + i\omega\tau} \tag{4.11c}$$

$$\rho_{eff} = (1 - \phi)\rho^s + \phi\rho^f \tag{4.11d}$$

$$\tau = \frac{\rho_0^f \mathcal{K}}{(\phi_0)^2} \tag{4.11e}$$

in which Λ is the isotropic stretch due to the pressurisation, $\tilde{\mu}$ is similar to a shear modulus and dependends on the stretch, ρ_{eff} the effective density, ϕ is the porosity, ρ^s the density of the solid, ρ^f the density of the fluid, ω the pulsation of the wave, and $\mathcal{K}$ the hydraulic permeability. The subscript 0 denotes quantities that are assessed in the static pressurised state. For $\omega\tau << 1$, the last term in Equation 4.11c can be neglected. When $\omega\tau = O(1)$, $\tilde{\rho}$ becomes a complex number and quantifies the dissipation that occurs as the fluid moves relatively to the solid matrix. At much larger $\omega\tau$, $\tilde{\rho} \approx \rho_0^s$. [51]

The solid phase is hyperelastic and is characterised by a strain energy density function W, in which $W_i = \frac{\partial W}{\partial I_i}$ and I_i are the invariants of the left Cauchy-Green strain tensor. Note the similarity between Equation 4.11a and Equation 3.4b. The change in SWV can also be derived:

$$\frac{c_s^2}{c_{s,0}^2} = \frac{W_1(\Lambda) + \Lambda^2 W_2(\Lambda)}{\Lambda\left(W_1(1) + W_2(1)\right)} \tag{4.12}$$

in which $c_{s,0}$ is the SWV when no strain is present ($\Lambda = 1$). More information concerning the formulas and derivations can be found in [51]. As noted in [65], this analytical model is adequate for large, but purely volumetric deformations under constant pressurisation. The model can therefore be extended by splitting the principal stretches λ_i in a pure isotropic dilation component (with isotropic stretch Λ) and isochoric deformation components (with principal stretches $\tilde{\lambda}_i$). The corresponding deformation gradient F is [65]:

$$\mathbf{F} = \begin{bmatrix} \lambda_1 & 0 & 0 \\ 0 & \lambda_2 & 0 \\ 0 & 0 & \lambda_3 \end{bmatrix} = \begin{bmatrix} \Lambda & 0 & 0 \\ 0 & \Lambda & 0 \\ 0 & 0 & \Lambda \end{bmatrix} \begin{bmatrix} \tilde{\lambda}_1 & 0 & 0 \\ 0 & \tilde{\lambda}_2 & 0 \\ 0 & 0 & \tilde{\lambda}_3 \end{bmatrix} \tag{4.13}$$

The plane shear wave velocity with propagation direction in line with the principle axis of λ_2 and polarization direction[5] in line with the principle axis of λ_1 can be derived (see [65]). The initial and final equations are shown here:

$$\rho c_s^2 = J^{-1}\lambda_2^2 \frac{\lambda_1 \frac{\partial W}{\partial \lambda_1} - \lambda_2 \frac{\partial W}{\partial \lambda_2}}{\lambda_1^2 - \lambda_2^2} = 2\frac{\tilde{\lambda}_2^2}{\Lambda} W_1 + 2\Lambda\tilde{\lambda}_1^{-2} W_2 \tag{4.14}$$

where $J = det(\mathbf{F})$ is the Jacobian.

[5] The polarization direction corresponds the direction of particle motion induced by the ARF [23].

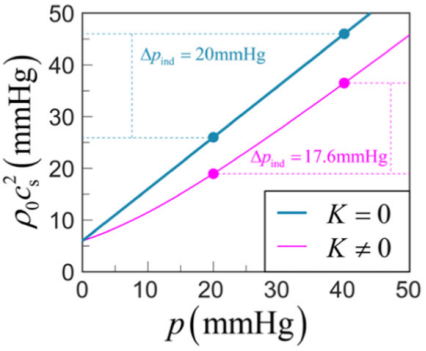

Figure 4.4: Relationship between the IFP (p) and the SWV (c_s) derived from a biomechanical model of a porous, hyperelastic, and unconfined tumour. ρ_0 is the initial density of the solid matrix of the tumour. The K is parameter denoting volumetric deformation, the material is incompressible when $K = 0$. [89]

4.2.3 Biomechanical Model

In [89], the authors developed a biomechanical model to quantitatively assess the influence of IFP on SWV in a confined solid tumour. More specifically, the model considers porous and hyperelastic tissues, and takes into account tumour growth and confinement. The analytical derivation of their biomechanical model shows that high IFP significantly increases the SWV. This strong correlation suggests that SWE can serve as a non-invasive technique for estimating the IFP *in vivo*. [89]

Determination of the absolute IFP requires knowledge of the shear modulus, which is difficult to obtain *in vivo*. However, the variation of IFP can be assessed instead through, for example, SWV measurements in the tumour before and after treatment. When considering an unconfined tumour with an incompressible solid phase, the relationship between the IFP and SWV (c_s) becomes [89]:

$$\Delta IFP = \Delta(\rho_0 c_s^2) \tag{4.15}$$

where ρ_0 is the effective tumour density in the static pressurised state. The relationship is shown in Figure 4.4. This equation is independent of the tumour constitutive parameters if the strain energy function W is dependent on I_1 only. For a general isotropic strain energy function, the equation becomes [89]:

$$\Delta IFP = \Delta(\rho_0 c_s^2) + \Delta(2W_2\Lambda) + \Delta(2W_3\Lambda^3) \tag{4.16}$$

where Λ is the stretch factor due to the interstitial fluid pressure.

Part II

Materials & Methods

5 Simulation Setup

The primary objective of this thesis is to examine how shear wave velocity (SWV) is affected by changes in the interstitial fluid pressure (IFP) through computational modelling. Thus, a numerical poroelastic model that mimics human soft tissues needs to be constructed. In this regard, two different models are developed. The first model, referred to as the 'healthy model' (chapter 6), serves to investigate the influence of various parameters on the modelling results. The second model, referred to as the 'tumour model' (chapter 7), is constructed to study a more realistic and relevant clinical scenario by incorporating a tumour mass.

The healthy and tumour models are 2-Dimensional (2D). They contain porous materials, with either constant or strain-dependent porosity and permeability. The solid phase of the materials is characterized by either linear elasticity or hyperelasticity. The simulation setup is explained in the following sections. All modelling is performed using COMSOL Multiphysics® 6.1 (COMSOL AB, Stockholm, Sweden), while the post-processing of results is carried out in MATLAB R2020b (The MathWorks Inc., Natick, MA, USA).

5.1 Geometry

In both the healthy and tumour model the tissue is represented by a square with sides of 70 mm. This is larger than the Region Of Interest (ROI), which lies in the central square with sides of 30 mm and represents the tissue under investigation.The modelled tissue is larger than the ROI to prevent reflection of shear waves within the ROI.[1]

5.2 Poroelastic Modelling in COMSOL Multiphysics

5.2.1 Coupling of Fluid and Solid Phase

A poroelastic interface is available in COMSOL Multiphysics® that couples the Solid Mechanics module (describing the behaviour of the solid matrix) to the Darcy's Law interface (describing fluid behaviour) [16]. Poroelastic coupling with the Brinkman equation (see subsection 4.1.2), however, is not possible within this multiphysics model.

Therefore, a poroelastic model was recreated manually using the Free and Porous Media Flow module (for the fluid phase) and the Solid Mechanics module (for the solid phase) as validated by [74]. The Free and Porous Media Flow module is used as it is governed by the Navier-Stokes equations in the fluid domain (computing both fluid velocity and pressure) and Brinkman equations in the porous domain and is adequate for free and fast flow [41].

Both modules are coupled bidirectionally to ensure poroelastic deformation. The fluid pressure governed by the Free and Porous Media Flow module induces a body load on the solid phase, resulting in either swelling or shrinking. Alternatively, changes in volumetric strain of the solid phase influence the fluid phase similarly to a mass source. The coupling factors are represented by the following contributions:

$$\mathbf{F} = -\nabla \mathbf{P} \tag{5.1a}$$

$$Q_{br} = -\rho \frac{\partial \varepsilon_{vol}}{\partial t} \tag{5.1b}$$

where the volumetric body force F (units N/m^3) is added to the solid phase and the mass source Q_{br} (units $kg/(m^3 \cdot s)$) is added to the fluid phase. [16, 31, 74]

[1] A perfectly matched layer (PML), which is an absorbing domain for waves, can be used instead to prevent reflections at the boundaries [18, 58] and was used in [31]. However, PMLs don't efficiently absorb the evanescent waves in the time domain [18], and were therefore not implemented in this model. Low-reflecting boundaries could be used instead in the time-dependent analyses but were not tested in this study [17].

5.2.2 Strain-Dependent Porosity and Permeability

Additionally, porosity and permeability are modelled as either constant or strain-dependent variables as explained in subsection 4.1.4. Modelling of the strain-dependency is essential in simulations involving high strains, such as confined compression experiments. In these situations, simulations will not converge if the strain-dependency is not modelled. This arises from the fact that the solid and fluid phase are (nearly) incompressible, and the only means of effectively compressing the poroelastic medium is through fluid outflow accompanied by a reduction in porosity.

Therefore, the present study will assess the influence of strain-dependent poroelasticity within the context of the application of this thesis. The strain-dependent porosity and permeability are modelled according to Equations 4.10 and were manually inserted into COMSOL Multiphysics®.

5.3 Shear Wave Generation

The shear wave is generated by applying a downwards time-dependent body load, representing the ARF (see Figure 5.1a), of $1.5 \cdot 10^6$ N/m^3 in the axial direction over an area of 1 by 5 mm in the centre of the geometry. In [31], a height of 5 mm was chosen as the resulting shear wave propagation is similar to the one observed in the chicken breast experiments (subsection 4.2.1). Although the shear wave propagation velocity is not dependent on the magnitude of the applied force, it is important for the load to be sufficiently high to differentiate the resulting tissue displacements from numerical noise. Therefore, the body load and width over which it is exerted were increased with respect to [31]. Additionally, they also allow for more realistic tissue displacements, with peak displacements being in the range of $10 - 20$ μm [53].

Typically, the duration of an ARF push is $0.1 - 0.5$ ms [58]. In the simulations, the load is sustained for a duration of 0.3 ms, similar to the experimental settings during the measurements on chicken breasts performed in [31]. It is represented by a rectangular load in time, with smooth transition zones (of 20 μs) to improve convergence. This is illustrated in Figure 5.1b. The total simulation time, starting with the application of the body load, is 3 ms for the healthy model and 4 ms for the tumour model. As such, the shear waves can propagate sufficiently across models with different material parameters and boundary conditions to allow (accurate) tracking of the SWV. Similarly, the maximal time step of the solver is constrained to 0.01 ms. The results at every 0.01 ms are stored for post-processing. [31]

5.4 Shear Wave Post-Processing

The velocities of the solid phase in the axial direction (direction of the ARF pulse) at all mesh nodes and all timeframes are exported from COMSOL Multiphysics® and imported into MATLAB® for post-processing. During post-processing, only the values within the ROI are extracted and interpolated onto a regular grid containing approximately the same number of nodes as the original mesh in the ROI. The velocities of the shear waves propagating to the left and right (e.g., see Figure 5.2 (top)) are estimated using the Radon sum transform, which is widely used for shear wave elastography to obtain the shear wave trajectory and velocity [34].

The main shear wave propagation occurs perpendicularly to the ARF, along the horizontal line through the centre of the area on which the ARF was applied. Along this path, the axial velocities can be represented in function of time. Various linear spatiotemporal trajectories can be defined for the shear wave propagation by considering a fixed starting point (x_{start},t_{start}) and different end positions (x_{end},t_{end}). The Radon transform calculates the sum of the axial velocities along all of these trajectories. The true shear wave trajectory (e.g., see Figure 5.2 (bottom)) is characterised by the largest axial displacements or velocities, and its Radon sum

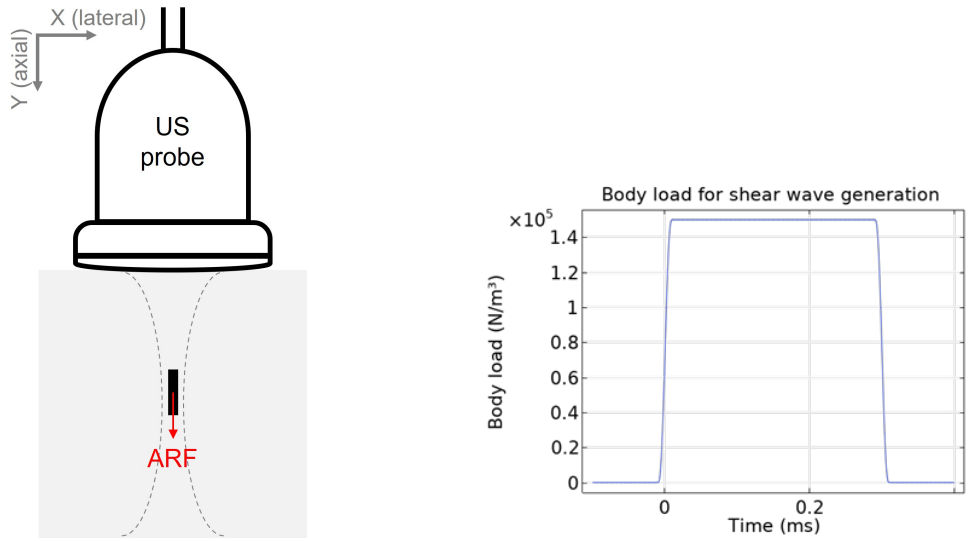

(a) (b)

Figure 5.1: (a) Physical representation of the body load: is is the acoustic radiation force (ARF) induced by the ultrasound (US) transducer. (b) Applied body load in function of time to generate shear waves.

will thus be maximal. The corresponding SWV (c_s) is the slope between the start- and endpoint [11, 68]:

$$c_s = \frac{x_{end} - x_{start}}{t_{end} - t_{start}} \tag{5.2}$$

The code for the SWV estimation was provided by Dr. Ir. Annette Caenen. It is recommended to select the starting point outside of the lateral excitation beam width to avoid diffraction effects [68], meaning that the data from the nodes on which the ARF is applied and the timeframes during the ARF application should be neglected. In this study, the starting time was therefore set to $t_{start} = 0.3\ ms$ (skipping the first 30 timeframes). However, the number of nodes within the area of body load application is dependent on the mesh size. In order to keep post-processing consistent across different meshes, no nodes were neglected ($x_{start} = 0\ mm$).

5.5 Simulation Outline

The simulation process consists of two distinct steps, followed by post-processing to obtain the SWVs. Initially, the material undergoes a stationary step where the IFP is applied, meaning that the steady-state solution after the pressurisation is obtained. The healthy and tumour model are pressurised in different ways, as will be explained in sections 6.1 and 7.2. A stationary step has the advantage of being faster than time-dependent studies and does not include transient effects. Subsequently, in the second step, shear waves are generated and their propagation is analysed, thereby inherently requiring a time-dependent study. An overview of the simulation process is provided in Figure 5.3.

For both steps, the default solver configurations of COMSOL Multiphysics® are implemented. An 'automatic' nonlinear method is used in the stationary solver, which enables the solver to automatically detect whether a linear solver approach is applicable [15]. The iterative process is terminated using a relative tolerance of 0.001 (default). For the time-dependent step, an implicit solver is employed[2]. A method based on BDF (backward differentiation formula) is

[2]Note that explicit solvers are generally more computationally efficient for transient models such as shear wave propagation models [58].

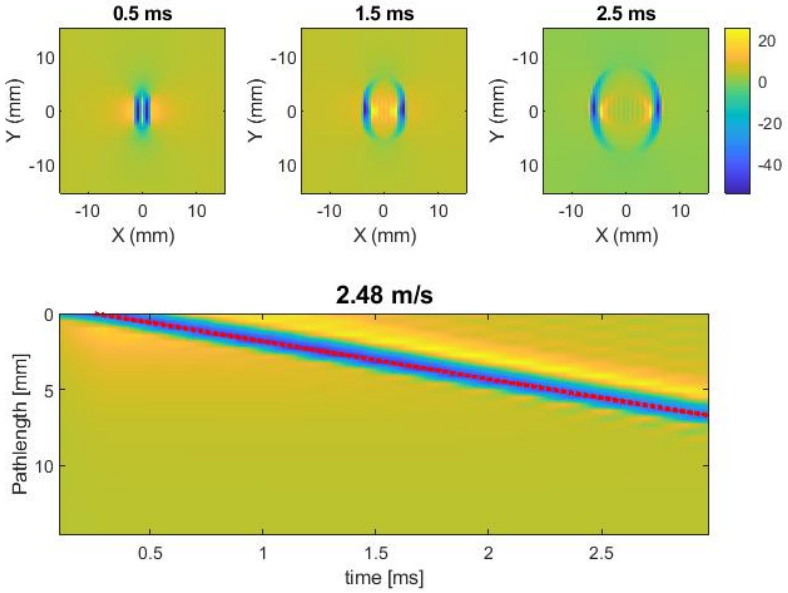

Figure 5.2: Example of shear wave processing. (top) Shear wave propagation at different timeframes. (bottom) Trajectory of shear waves propagating to the left along the central horizontal line. The SWV is the slope of the trajectory.

used with a minimal and maximal order of 1 and 2, respectively. Importantly, the maximum step constraint is changed from 'automatic' to a 'constant' value of 0.01 *ms* to ensure the time steps taken by the solver don't exceed the time step used for post-processing (section 5.3).

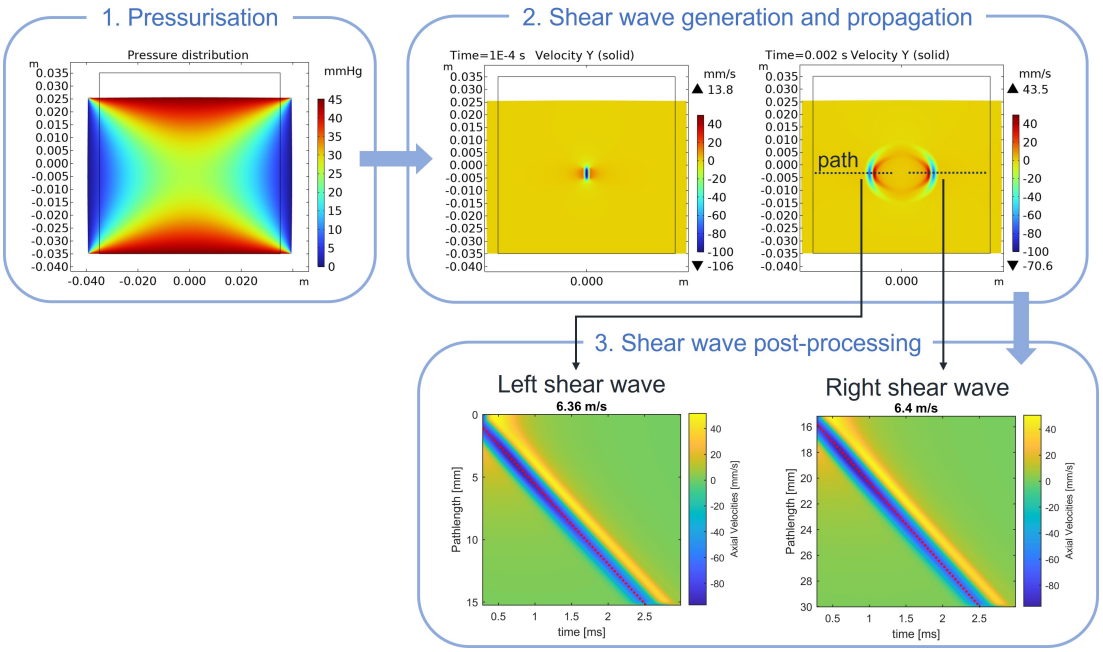

Figure 5.3: Overview of the simulation process applied to one of the healthy models.

6 Healthy Model - Default Configuration

6.1 Boundary Conditions

The boundary conditions that are applied on the geometry (see section 5.1) are illustrated in Figure 6.1. In the default model, the solid matrix is fixed at the central point of the bottom edge, while roller constraints are placed along the entire bottom edge. A roller is used instead of a fixed edge as in [31] to prevent singularities in the corners. The interstitial fluid is pressurised through inlet (for fluid inflow) and outlet (for fluid outflow) boundary conditions. Inlet pressures ranging from $0 - 120$ $mmHg$ are applied on the top and bottom edges and an outlet pressure of 0 $mmHg$ is applied on the sides. This leads to a symmetric pressure distribution (Figure 6.2a), in contrast to the models presented in [31], and an elevated pressure within the ROI (Figure 6.2b). As mentioned in chapter 5, the fluid phase is pressurised during the steady state step and maintained in the subsequent step during the shear wave propagation.

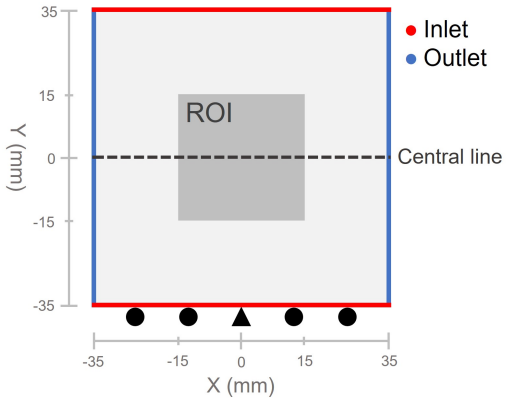

Figure 6.1: Boundary conditions of healthy model. The solid matrix is fixed at the central point of the bottom edge and roller constraints are placed along the entire bottom edge. An inlet fluid pressure is applied at the top and bottom boundary and an outlet pressure of 0 $mmHg$ at the sides.

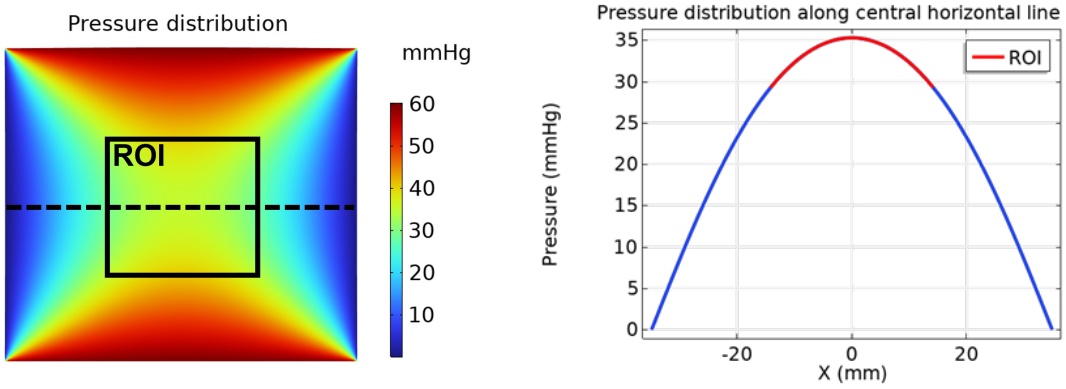

Figure 6.2: Example of obtained pressure distributions on the whole model (a) and central horizontal line (b) when a fluid inlet pressure of 60 $mmHg$ is applied at the top and bottom boundary and and outlet fluid pressure of 0 $mmHg$ at the sides.

6.2 Material Parameters

Both a linear elastic and hyperelastic solid matrix are simulated to analyse their influence. In the linear elastic material, a Young's modulus of 20 kPa and Poisson's ratio of 0.495 are

used as in [31], representing healthy soft (nearly incompressible) biological tissue, including breast tissue [25]. A stiffer linear elastic material with $E = 100\ kPa$ is also modelled. The first order Ogden hyperelastic parameters (subsection 4.1.3) are roughly fitted to the chicken breast experiments (subsection 4.2.1) by trial and error to obtain realistic SWVs, resulting in an infinitesimal shear modulus $\mu_1 = 0.15\ kPa$ and stiffening coefficient $\alpha_1 = 70$. The density was set to 945 kg/m^3, representing the mean breast density [71].

The interstitial fluid is modelled with a viscosity of $1.5 \cdot 10^{-3}\ Pa \cdot s$ and a density of 1000 kg/m^3 as in [31]. The default porous matrix is characterised by a porosity of 0.51 and permeability of $5.3 \cdot 10^{-12}\ m^2$ when constant poroelasticity is assumed, and an additional exponential factor of 4.3 when strain-dependency is modelled instead (subsection 4.1.4). These values represent the mean poroelastic values in healthy breast tissue as shown in Table 4.1[1]. An overview of all material parameters is provided in Table 6.1.

Table 6.1: Overview of material parameters for the healthy model.

Property	**Value**
Linear solid matrix	
Young's modulus	$E = 20\ kPa$ or $100\ kPa$
Poisson's ratio	$\nu = 0.495$
Density	$\rho = 945\ kg/m^3$
Hyperelastic solid matrix	
Ogden parameters	$\mu_1 = 0.15\ kPa$, $\alpha_1 = 70$
Density	$\rho = 945\ kg/m^3$
Interstitial fluid	
Viscosity	$\mu = 1.5 \cdot 10^{-3}\ Pa \cdot s$
Density	$\rho = 1000\ kg/m^3$
Porous medium	
(Initial) porosity	$\phi = 0.51$
(Initial) permeability	$k = 5.3 \cdot 10^{-12}\ m^2$
Exponential factor	$M = 4.3$

For visualisation purposes, the curves for the strain-dependent porosity and permeability are shown in Figure 6.3 and the hyperelastic stress-strain relationship in Figure 6.4. The former two are obtained in confined simulations, where roller constraints are applied at the sides and bottom of the geometry and a prescribed displacement is applied on the top boundary. The resulting porosity, permeability, and strain of the central point are plotted. The latter graph is obtained during the stationary step of the healthy model at different inlet pressures. The resulting stresses and strains in the central point are plotted.

6.3 Mesh & Mesh Sensitivity Analysis

As the 2D geometry is simple and regular, a uniform mesh is obtained with quadrilateral elements (4 nodes). An example is shown in Figure 6.5. By default, COMSOL Multiphysics® uses elements with full integration. In contrast to triangular elements (3 nodes) that are used more often for complex geometries, quadrilateral elements don't contain sharp angles, thereby mitigating numerical dispersion artifacts [58]. Additionally, the obtained mesh elements are aligned with the the primary shear wave propagation and displacement directions, reducing numerical dispersion artifacts even more [31].

The optimal mesh, balancing accuracy and computational time, is selected based on a mesh sensitivity analysis. To this end, meshes with different sizes were created. The settings that

[1]The hydraulic permeability is shown in the table, and has to be multiplied by the fluid viscosity in order to obtain the intrinsic permeability as explained in subsection 4.1.1

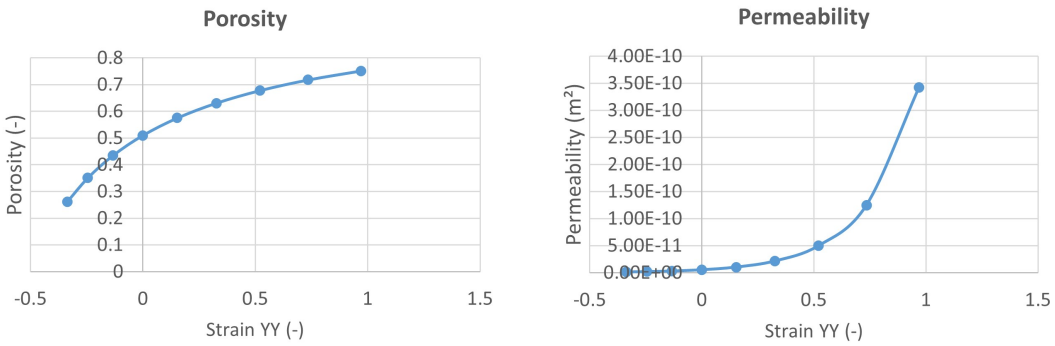

(a) **(b)**

Figure 6.3: The porosity (a) and permeability (b) in function of strain, obtained during confined compression simulations in which the sample is confined in between permeable plates and a compression displacement is applied on the top edge.

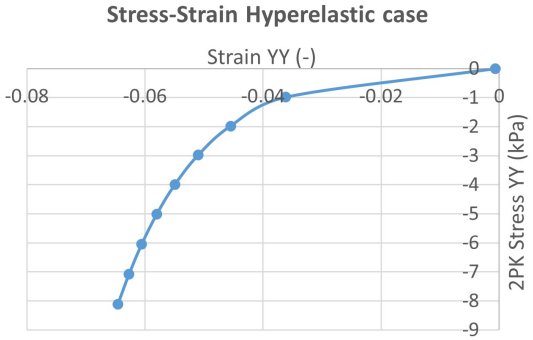

Figure 6.4: Resulting stress-strain relationship of the poro- and hyperelastic material.

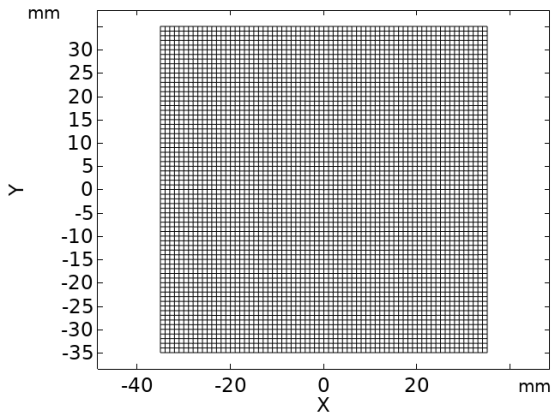

Figure 6.5: Example of a quadrilateral mesh of the geometry.

were used to create the meshes are summarised in Table 6.2. For all of these meshes, simulations are performed with an inlet pressure of 60 $mmHg$ (resulting in a pressure of approximately 35 $mmHg$ in the center of the ROI) and strain-dependent porohyperelasticity with the material parameters provided in Table 6.1. As such, the mesh sensitivity analysis is performed on the 'most complicated' model.

The selected parameters for the mesh sensitivity analysis are the estimated SWV, axial (Y) velocity, axial (Y) displacement, fluid pressure, and axial (YY) second Piola-Kirchhoff (2PK)

stress. They are analysed along the central horizontal line (within the ROI) at various time-points. Conversely, they are also examined in function of time at different X-coordinates along the aforementioned line (see Figure 6.1). For a comprehensive comparison of the parameter values across the different meshes, their maximum absolute values are compared. Specifically, the relative change of the parameter of interest x with respect to the previous mesh can be defined:

$$\%change = \left| \frac{x_{previous} - x_{current}}{x_{previous}} \right| \cdot 100\% \tag{6.1}$$

Table 6.2: Characteristics of the meshes used in the mesh sensitivity analysis for the healthy model. The minimal element size in all meshes was kept to 0.02 *mm* and the quality of all mesh elements in all meshes is 1 ('perfect'). The selected mesh is indicated in blue.

Mesh	Max. element size [mm]	# elements
1	1	4900
2	0.7	10000
3	0.5	19600
4	0.35	40000
5	0.28	62500
6	0.242	84100
7	0.2	122500
8	0.175	160000

The results of the mesh sensitivity analysis are presented in Figures 6.6-6.10[2]. The waveforms of the axial (Y) velocities at certain X-coordinates in function of time and at certain timeframes in function of the X-coordinates are shown in the Appendix, Figure B.1. The displacement, fluid pressure, and solid stress are minimally influenced (less than 0.1%) by the mesh size. The axial velocities are impacted more by the mesh size, and converge within a threshold of 5% at approximately 800000 mesh elements. At this mesh size, estimated SWVs have already converged within a threshold of 1%. Therefore, the final mesh was chosen to be the one with 84100 elements as indicated in blue in Table 6.2.

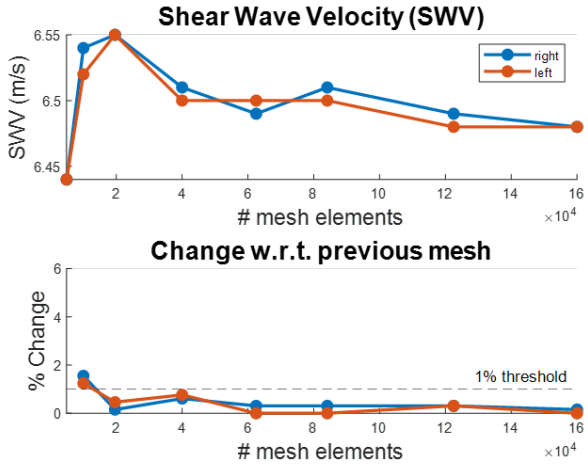

Figure 6.6: Estimated SWVs of the shear waves propagating to the left and right (top) and the change with respect to the previous mesh (bottom) for the healthy model.

[2]A comparison of the computation times could not be provided as simulations were performed on different computers. However, for reference, the model with a mesh of 84100 element ran during approximately four hours on a computer with an 11th Gen Intel(R) Core i7 (2.80 GHz) and 16 GB of RAM.

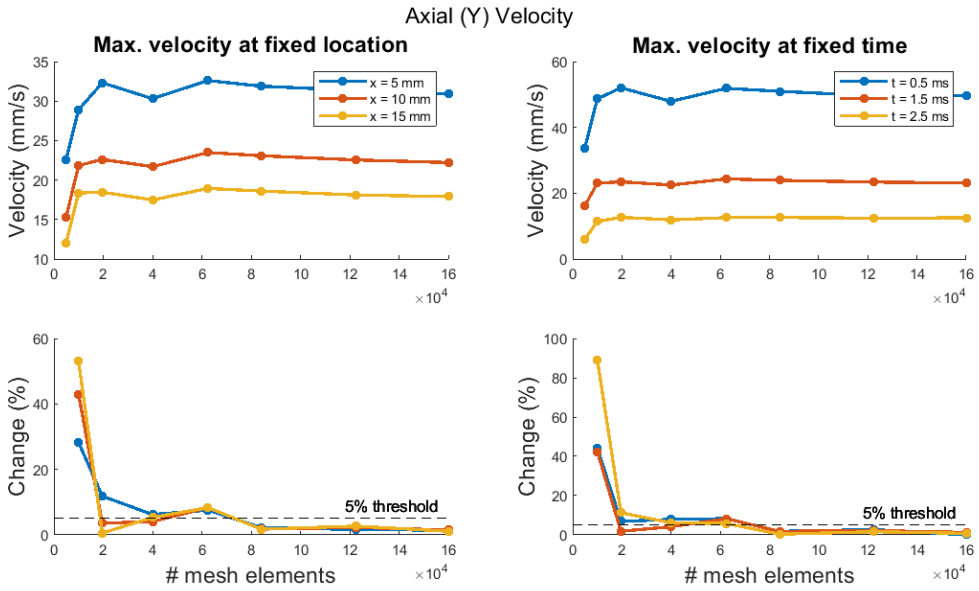

Figure 6.7: Maximal absolute velocity at multiple x-coordinates along the central horizontal line (left) and multiple timepoints (right). The relative changes with respect to the previous mesh are shown in the bottom plots.

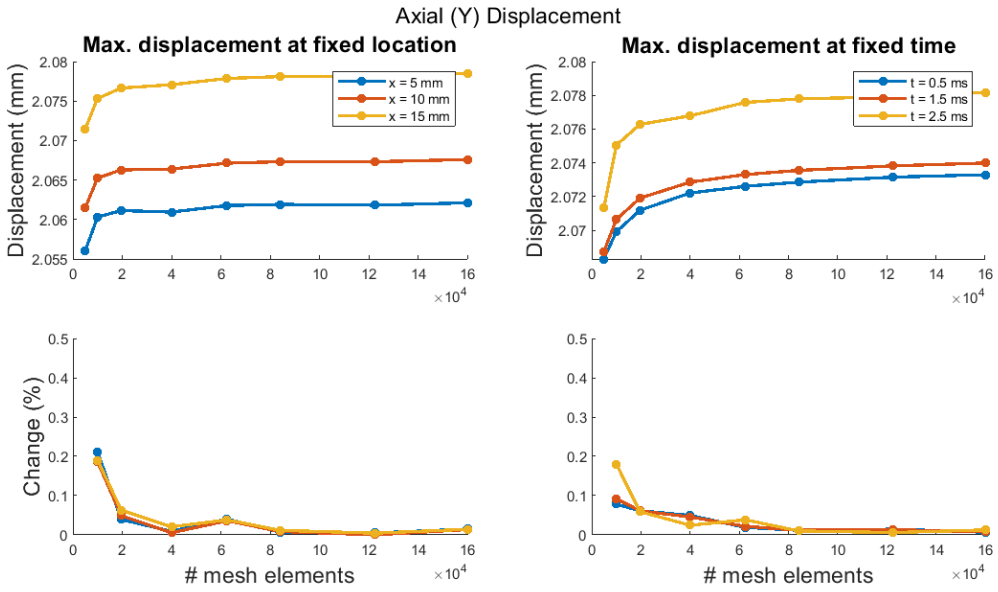

Figure 6.8: Maximal absolute displacement at multiple x-coordinates along the central horizontal line (left) and multiple timepoints (right). The relative changes with respect to the previous mesh are shown in the bottom plots.

6.4 Overview of Simulations

Multiple simulations are performed to study the influence of different parameters on the results. They are explained in more detail in chapters 8 and 9, but an overview is presented here:

– The influence of the permeability is assessed with the default boundary conditions of the model, i.e., fixed inlet pressure.

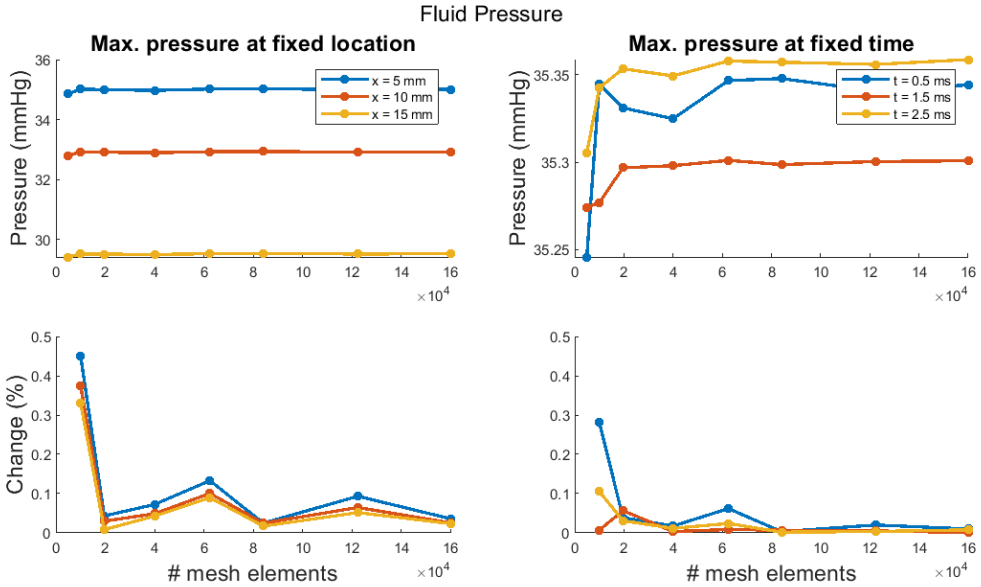

Figure 6.9: Maximal absolute fluid pressure at multiple x-coordinates along the central horizontal line (left) and multiple timepoints (right). The relative changes with respect to the previous mesh are shown in the bottom plots.

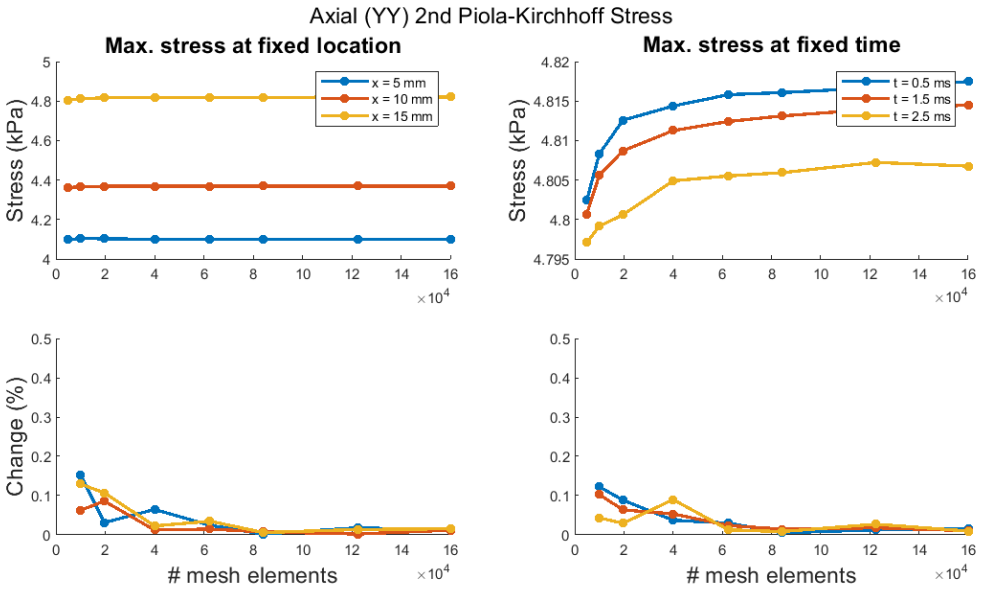

Figure 6.10: Maximal absolute second Piola-Kirckhhoff stress at multiple x-coordinates along the central horizontal line (left) and multiple timepoints (right). The relative changes with respect to the previous mesh are shown in the bottom plots.

- The influence of the permeability is assessed with adapted boundary conditions, i.e., fixed inlet flow.
- The influence of the porosity is assessed with the default boundary conditions.
- The influence of strain-dependent permeability and porosity are assessed with the default boundary conditions.
- The influence of the intrinsic stiffness and hyperelasticity is assessed in the non-pressurised

state, i.e., with adapted boundary conditions (no steady state and no inlet/outlet pressures).

- The influence of confinement in pressurised tissues is assessed, i.e. with adapted boundary conditions (constrained).
- The influence of pressurisation on SWV is assessed with the default boundary conditions.

6.5 Remarks

The models presented in this chapter were built up starting from the 'poroelastic numerical model with shear wave interaction' developed last year in the Master's thesis of Kristyna Holkova [31]. A summary of the changes and improvements that are implemented in this model is provided here:

- Hyperelasticity and strain-dependent porosity and permeability were introduced.
- Material parameters were adapted to be more similar to breast tissue.
- The body load for the shear wave generation, as well as the area on which it is applied, were increased in order to obtain more realistic tissue displacement magnitudes.
- The boundary conditions were adapted in order to obtain a symmetric pressure distribution across the ROI. Additionally, the fixed constraint at the bottom boundary was replaced by a roller (and one fixed point) in order to prevent singularities at the bottom boundary and convergence issues.
- The pressure was applied in a stationary step instead of time-dependent step as only the steady-state response is of interest in the model, avoiding transient effects and reducing computation time.
- Smaller timesteps were used in the step analysing the shear wave propagation to obtain a more accurate wave speed estimation.
- Post-processing was improved through interpolation of the nodes in the ROI into a regular grid. This avoids the artifacts that were present in [31] and are shown in Figure 6.11.
- The Perfectly Matched Layer (PML) was removed as it is not efficient in the time domain as explained in footnote 1.

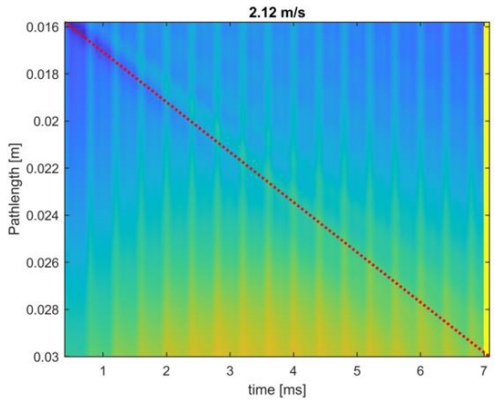

Figure 6.11: Example of artifacts in spatiotemporal plot due to absent interpolation of values during post-processing. [31]

7 Tumour Model - Proof of Concept

The healthy model described in the previous chapter mainly serves to analyse how IFP affects SWV. The tumour model described in this chapter serves to visualise its clinical implementation, as illustrated in Figure 7.1. The tumour model is a 'proof-of-concept' and is not fully elaborated. However, important aspects related to the tumour model are still discussed and analysed.

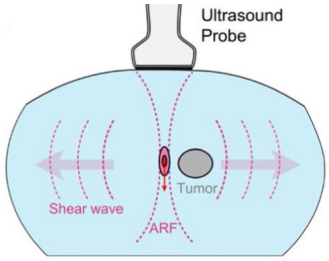

Figure 7.1: Illustration of SWE in a tissue including a tumour mass. [89]

7.1 Geometry and Mesh

For the tumour model, a square with sides of 70 mm is kept as in the previous model (section 5.1). A tumour mass is now added and is represented by a circle with radius 8 mm (corresponding to stage I breast cancer [48]). The center of the circle is shifted 10 mm to the right with respect to the centre of the square. This is visualised in Figure 7.2a. Note that the circle is made up of two layers, this is to facilitate the inclusion of a necrotic core (with different material parameters) in future models, even though the same material properties were applied throughout the whole tumour in this model. Note also that the geometry has been split up using additional lines. This is to allow different kinds of meshes to be used in each domain, as explained below.

As the tumour model is a proof of concept and not meant to study the influence of the IFP and material parameters on the estimated stiffness in detail, only a moderately fine mesh is used. The circle is meshed with free triangular elements. A small square surrounding the circle is meshed with free quadrilateral elements to obtain a transition towards a mapped (structured) mesh. As explained in section 6.3, the structured mesh is aligned with the primary shear wave propagation and displacement directions, which reduces numerical dispersion artifacts.

A maximal element size of 0.4 mm is used for all three types of meshes. Similarly to the previous model, the skewness factor of the elements in the structured mesh is 1 ('perfect'). But this is not the case for the elements in the circle and surrounding small square, see Figure 7.2d. The minimal skewness factor is 0.6.

7.2 Boundary Conditions

Similarly to the previous model, the bottom boundary is fixed at the centre and roller constraints are applied throughout the entire bottom boundary (section 6.1). Pressurisation of the tumour mass has to be done differently now, as an inlet pressure can only be used on outer boundaries and the pressure distribution within the tissue should be elevated in the centre of the tumour, with a high pressure drop towards the edges, and a low pressure within the healthy tissue surrounding the tumour. Two different boundary conditions can be used instead for the inlet: the pressure point constraint or mass source.

The pressure point constraint fixes the pressure level of a certain point and is used in cases where the pressure level cannot be defined on an outer boundary, in contrast to the inlet

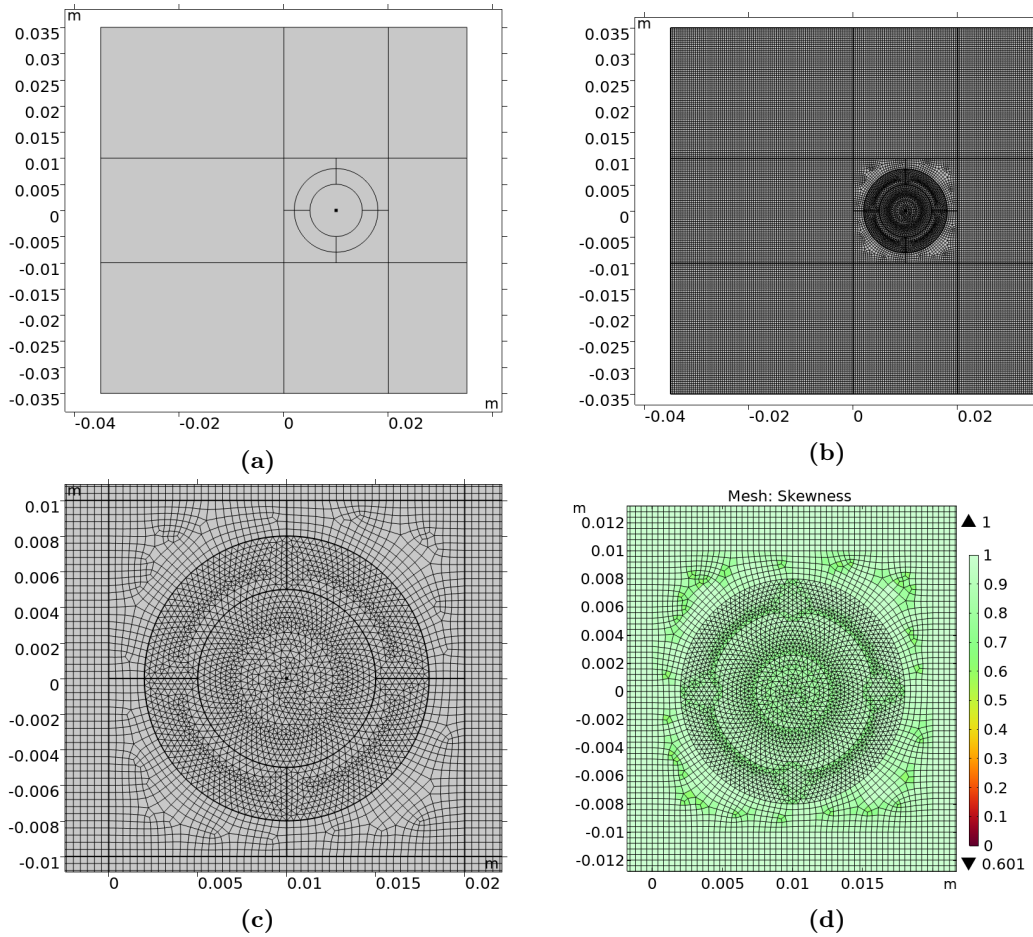

Figure 7.2: Geometry and mesh of tumour model. (a) Geometry. (b) Complete mesh. (c) Close-up of mesh around tumour inclusion. (d) Close-up of element skewness around tumour inclusion.

pressure boundary condition [16]. As the name suggests, the pressure can only be fixed at a certain point, not over an area. The resulting pressure distribution shows a sharp peak in the centre of the tumour where the constraint was defined, an example is shown in Figure 7.3. Even though it is convenient to define a pressure in the centre of the model, the resulting pressure distribution is not realistic due to the sharp peak. Therefore, a mass source constraint is used instead and is combined with an open boundary condition, through which fluid can enter and leave the domain, on the four outer boundaries.

A mass source can represent the injection of fluid (mass) per volume over time. The equation for mass conservation (defined in Equation 4.6) therefore becomes:

$$Q_m = \frac{\partial \phi}{\partial t} + \nabla \cdot \mathbf{q} \tag{7.1}$$

where Q_m is a mass source with units $kg/(m^3 \cdot s)$. This formulation is less convenient to use, as the pressure cannot be defined directly. The resulting pressure (drop) is dependent on the magnitude and radius of the mass source, as well as the porous material properties. The influence of these parameters is discussed in chapter 10.

7.3 Overview of Material Parameters

The material parameters of the healthy tissue are kept as in section 6.2. For the tumour tissue, the same material model is used but with different material parameters. As explained in

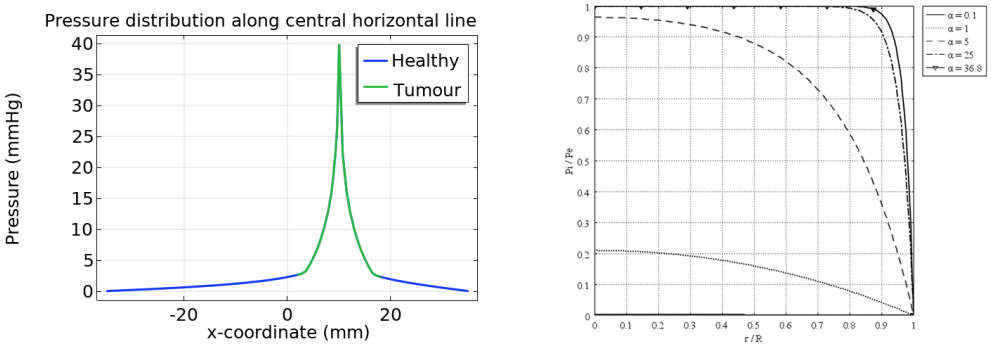

(a) **(b)**

Figure 7.3: (a) Example of a pressure distribution along the central horizontal line if a pressure point constraint is used. (b) Example of different (dimensionless) pressure distributions along the (dimensionless) radius of a tumour [75].

subsection 4.1.4, the porosity and permeability in tumour tissues is often lower and the tissue is stiffer.

Table 7.1: Overview of material parameters for the healthy model.

Property	Healthy tissue	Tumour tissue
Linear solid matrix		
Young's modulus	$E = 20\ kPa$	$E = 100\ kPa$
Poisson's ratio	$\nu = 0.495$	$\nu = 0.495$
Density	$\rho = 945\ kg/m^3$	$\rho = 945\ kg/m^3$
Interstitial fluid		
Viscosity	$\mu = 1.5 \cdot 10^{-3}\ Pa \cdot s$	$\mu = 1.5 \cdot 10^{-3}\ Pa \cdot s$
Density	$\rho = 1000\ kg/m^3$	$\rho = 1000\ kg/m^3$
Porous medium		
(Initial) porosity	$\phi = 0.51$	$\phi = 0.44$
(Initial) permeability	$k = 5.3 \cdot 10^{-12}\ m^2$	$k = 1 \cdot 10^{-12}\ m^2$
Exponential factor	$M = 4.3$	$M = 4.1$

Close to the tumour edge, the permeability of the tumour changes smoothly to the permeability of the healthy tissue with a transition zone of 1 mm and two continuous derivatives. The change in permeability and resulting permeability distribution in the tissue are shown in Figure 7.4.

7.4 Overview of Simulations

The same simulation setup is used as for the healthy model and described in chapter 5. The only difference is that the simulation time of the second step is extended to 4 ms to ensure sufficient propagation of the shear waves within the tumour mass. The different simulations that are performed are summarised below:

- The influence of the mass source magnitude, mass source radius, and tumour permeability on the pressure distribution wihtin the model are assessed.
- The influence of the tumour inclusion on the SWV is evaluated by considering an identical hyperelastic tissue but different permeability than the surrounding healthy tissue.
- The influence of the tumour inclusion on the SWV is evaluated by considering a stiffer hyperelastic tissue than the surrounding healthy tissue with identical permeability.
- The combined influence of the tumour stiffness and permeability on the SWV is evaluated.

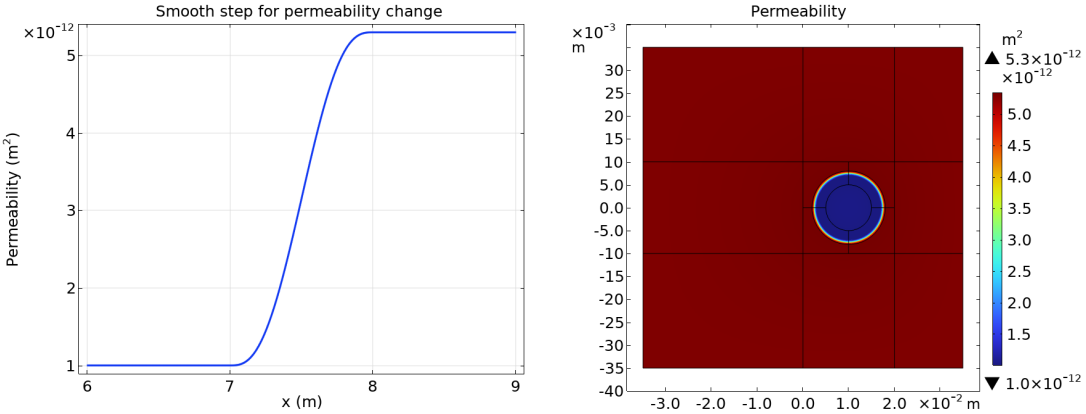

(a) **(b)**

Figure 7.4: Permeability change between healthy and tumour tissue. (a) Smooth step that was used for the change in permeability between the healthy and tumour tisse. (b) Resulting permeability distribution in the complete model.

Part III

Results & Discussion

8 Parametric Study - Healthy Model

In this chapter, the influence of different poroelastic properties on the fluid and solid phase are analysed. In general, the values of the material properties shown in section 6.2 are used. When different values are used, it is mentioned in the text. Additionally, when no time frame is mentioned, it means that the results after the stationary step (i.e., after pressurisation) are provided.

8.1 Effect of Permeability

8.1.1 Fixed Inlet Pressure

The influence of the permeability is studied in simulations with a linear elastic or hyperelastic material model and strain-dependent porosity and permeability. As can be seen from Table 8.1, changes in orders of magnitude of the permeability have a negligible effect ($<< 1\%$) on the solid matrix (stresses and strains). However, the permeability has a pronounced effect on the fluid flow. As expected from Darcy's Equation 4.1 (or Brinkman's Equation 4.7), a higher permeability increases the magnitude of the fluid flow. From this law, we'd also expect the permeability to influence the pressure drop. However, in these simulations the pressure at the in- and outlets is fixed through the boundary conditions. The influence of the permeability in the case that an inlet flow is defined instead of an inlet pressure, is discussed the following section.

8.1.2 Fixed Inlet Flow

At the top and bottom boundary, an inlet flow of 0.001 m/s is now applied instead of an inlet pressure. The outlet pressure is still kept to 0 $mmHg$ and only the hyperelastic case is analysed here. Results are provided in Table 8.2 and the resulting pressure distributions in the complete model are shown in Figure 8.1[1]. The influence of the permeability on the magnitude of the fluid flow is more limited compared to the previous case. However, marked differences in pressures can be observed. As the fluid phase is coupled to the solid phase via the pressure gradient (Equation 5.1), the solid matrix (stresses, strains, and displacements) is affected as well.

[1] Note that a smaller range of permeability values is used here due to convergence issues.

Table 8.1: Influence of the permeability with inlet pressure of 40 $mmHg$. Y denotes the axial direction and X the lateral direction. k is the intrinsic permeability, ε the strain, ε_{vol} the volumetric strain, S the second Piola-Kirchhoff stress, Δ the displacement, and q the fluid flow.

Linear ($E = 100\ kPa$) - Influence of permeability - Fixed inlet pressure										
$k\ [m^2]$	ε_{YY} [-]	ε_{XX} [-]	ε_{vol} [-]	$S_{YY}\ [kPa]$	$S_{XX}\ [kPa]$	$\Delta Y\ [m]$	$\Delta X\ [m]$	IFP $[mmHg]$	$q_Y\ [m/s]$	$q_X\ [m/s]$
Values at central point $x = 0\ mm$										
1.00e-14	-0.04036	0.04035	-1.228e-05	-2.740	2.658	-0.001475	-3.438e-16	22.28	-4.479e-08	3.905e-20
1.00e-12	-0.04036	0.04035	-1.229e-05	-2.740	2.658	-0.001475	-3.299e-16	22.28	-4.479e-06	-1.141e-18
1.00e-10	-0.04042	0.04041	-1.355e-05	-2.749	2.658	-0.001471	-2.161e-16	22.29	-4.466e-04	1.508e-16
Values at $x = 10\ mm$										
1.00e-14	-0.04059	0.04052	-7.669e-05	-2.969	2.456	-0.001477	3.811e-04	20.50	-4.552e-08	3.173e-07
1.00e-12	-0.04059	0.04052	-7.670e-05	-2.969	2.456	-0.001477	3.811e-04	20.50	-4.552e-06	3.173e-05
1.00e-10	-0.04065	0.04057	-7.758e-05	-2.976	2.457	-0.001473	3.816e-04	20.51	-4.538e-04	3.173e-03
Maximal values along central line $x = [-15\ mm, 15\ mm]$										
1.00e-14	-0.04036	0.04065	-1.226e-05	-2.740	2.658	-0.001475	5.725e-04	22.28	-4.479e-08	4.772e-07
1.00e-12	-0.04036	0.04065	-1.227e-05	-2.740	2.658	-0.001475	5.725e-04	22.28	-4.479e-06	4.772e-05
1.00e-10	-0.04042	0.04069	-1.353e-05	-2.749	2.658	-0.001471	5.732e-04	22.29	-4.466e-04	4.772e-03
Minimal values along central line $x = [-15\ mm, 15\ mm]$										
1.00e-14	-0.04081	0.04035	-1.569e-04	-3.249	2.199	-0.001479	-5.725e-04	18.27	-4.556e-08	-4.772e-07
1.00e-12	-0.04081	0.04035	-1.569e-04	-3.249	2.199	-0.001479	-5.725e-04	18.27	-4.556e-06	-4.772e-05
1.00e-10	-0.04085	0.04041	-1.574e-04	-3.253	2.201	-0.001475	-5.732e-04	18.27	-4.542e-04	-4.772e-03

Hyperelastic - Influence of permeability - Fixed inlet pressure										
$k\ [m^2]$	ε_{YY} [-]	ε_{XX} [-]	ε_{vol} [-]	$S_{YY}\ [kPa]$	$S_{XX}\ [kPa]$	$\Delta Y\ [m]$	$\Delta X\ [m]$	IFP $[mmHg]$	$q_Y\ [m/s]$	$q_X\ [m/s]$
Values at central point $x = 0\ mm$										
1.00e-14	-0.04939	0.05371	4.324e-03	-2.644	2.773	-1.837e-03	4.123e-16	23.09	-5.626e-08	-4.295e-20
1.00e-12	-0.04939	0.05371	4.324e-03	-2.643	2.773	-1.837e-03	-3.397e-16	23.09	-5.626e-06	2.656e-18
1.00e-10	-0.04940	0.05372	4.323e-03	-2.648	2.774	-1.836e-03	-2.154e-16	23.10	-5.620e-04	-1.813e-17
Values at $x = 10\ mm$										
1.00e-14	-0.04961	0.05352	3.902e-03	-2.890	2.564	-1.843e-03	4.968e-04	21.33	-5.768e-08	3.206e-07
1.00e-12	-0.04961	0.05352	3.902e-03	-2.890	2.564	-1.843e-03	4.968e-04	21.33	-5.768e-06	3.206e-05
1.00e-10	-0.04963	0.05353	3.901e-03	-2.894	2.565	-1.842e-03	4.969e-04	21.33	-5.763e-04	3.206e-03
Maximal values along central line $x = [-15\ mm, 15\ mm]$										
1.00e-14	-0.04939	0.05371	4.324e-03	-2.644	2.773	-1.837e-03	7.442e-04	23.09	-5.626e-08	4.839e-07
1.00e-12	-0.04939	0.05371	4.324e-03	-2.643	2.773	-1.837e-03	7.441e-04	23.09	-5.626e-06	4.839e-05
1.00e-10	-0.04940	0.05372	4.323e-03	-2.648	2.774	-1.836e-03	7.443e-04	23.10	-5.620e-04	4.839e-03
Minimal values along central line $x = [-15\ mm, 15\ mm]$										
1.00e-14	-0.04988	0.05325	3.373e-03	-3.195	2.299	-1.851e-03	-7.442e-04	19.10	-5.801e-08	-4.839e-07
1.00e-12	-0.04988	0.05325	3.372e-03	-3.195	2.299	-1.851e-03	-7.441e-04	19.10	-5.801e-06	-4.839e-05
1.00e-10	-0.04990	0.05327	3.372e-03	-3.199	2.301	-1.850e-03	-7.443e-04	19.11	-5.797e-04	-4.839e-03

Table 8.2: Influence of the permeability with inlet flow of 0.001 m/s. Y denotes the axial direction and X the lateral direction. k is the intrinsic permeability, ε the strain, ε_{vol} the volumetric strain, S the second Piola-Kirchhoff stress, Δ the displacement, and q the fluid flow.

Hyperelastic - Influence of permeability - Fixed inlet flow										
k $[m^2]$	ε_{YY} [-]	ε_{XX} [-]	ε_{vol} [-]	S_{YY} $[kPa]$	S_{XX} $[kPa]$	ΔY $[m]$	ΔX $[m]$	IFP $[mmHg]$	q_Y $[m/s]$	q_X $[m/s]$
Values at central point $x = 0$ mm										
1.00e-13	-0.1014	0.1286	2.725e-02	-1.833e+02	2.338e+02	-3.388e-03	-2.625e-15	2.032e+03	7.421e-17	-9.228e-05
1.00e-12	-0.0790	0.0862	7.214e-03	-2.213e+01	2.305e+01	-2.859e-03	-8.220e-17	1.873e+02	-1.324e-18	-6.782e-05
1.00e-11	-0.0458	0.0497	3.865e-03	-1.989e+00	2.169e+00	-1.662e-03	-7.775e-17	1.640e+01	2.917e-17	-3.500e-05
Values at $x = 10$ mm										
1.00e-13	-0.1046	0.1247	2.009e-02	-1.802e+02	2.204e+02	-3.457e-03	1.072e-03	1.912e+03	2.360e-04	-9.537e-05
1.00e-12	-0.0787	0.0849	6.187e-03	-2.154e+01	2.124e+01	-2.850e-03	7.612e-04	1.725e+02	2.678e-04	-6.406e-05
1.00e-11	-0.0451	0.0487	3.606e-03	-1.963e+00	1.978e+00	-1.639e-03	4.597e-04	1.497e+01	2.549e-04	-3.246e-05
Maximal values along central line $x = [-15\ mm, 15\ mm]$										
1.00e-13	-0.1014	0.1286	2.725e-02	-1.758e+02	2.338e+02	-3.388e-03	1.590e-03	2.032e+03	3.492e-04	-9.228e-05
1.00e-12	-0.0783	0.0862	7.214e-03	-2.078e+01	2.305e+01	-2.839e-03	1.135e-03	1.873e+02	3.932e-04	-5.896e-05
1.00e-11	-0.0442	0.0497	3.865e-03	-1.936e+00	2.169e+00	-1.610e-03	6.841e-04	1.640e+01	3.721e-04	-2.917e-05
Minimal values along central line $x = [-15\ mm, 15\ mm]$										
1.00e-13	-0.1085	0.1196	1.112e-02	-1.833e+02	2.032e+02	-3.539e-03	-1.590e-03	1.757e+03	-3.492e-04	-9.737e-05
1.00e-12	-0.0790	0.0832	4.921e-03	-2.213e+01	1.900e+01	-2.859e-03	-1.135e-03	1.543e+02	-3.932e-04	-6.782e-05
1.00e-11	-0.0458	0.0474	3.278e-03	-1.989e+00	1.744e+00	-1.662e-03	-6.841e-04	1.323e+01	-3.721e-04	-3.500e-05

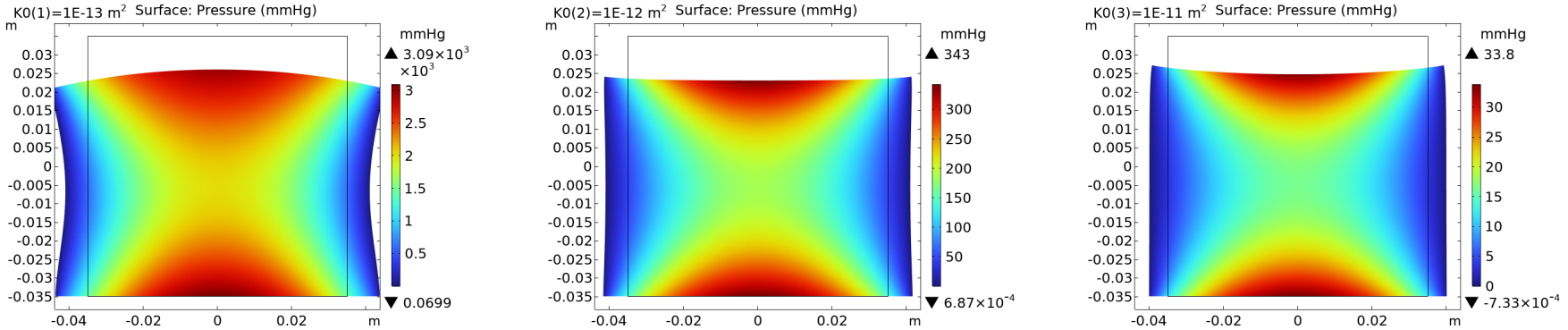

(a) **(b)** **(c)**

Figure 8.1: Influence of the permeability on the pressure distribution within a hyperelastic tissue when an inlet flow of 0.001 m/s is applied. (a) $k = 1 \cdot 10^{-13}$ m^2, (b) $k = 1 \cdot 10^{-12}$ m^2 (a) $k = 1 \cdot 10^{-11}$ m^2. Note the different color scales in each figure. The deformation of the tissue is also shown on the figures.

8.2 Effect of Porosity

The results of simulations with different porosities are shown in Table 8.3. A hyperelastic material model is used with inlet pressure of 40 $mmHg$ and strain-dependent porosity and permeability. As can be seen from the table, the porosity has no noticeable effect on the results (only the fluid velocity $\mathbf{v_f} = \frac{\mathbf{q}}{\phi}$ is affected). This is also the case in a linear elastic material model and when an inlet flow is defined (not shown). Estimated shear wave velocities in a linear elastic material with inlet pressure 20 $mmHg$ and porosities of 0.15, 0.51, and 0.85 all show a left and right SWV of 2.94 m/s. This behaviour can be explained by analysing the governing equations in more detail, as explained below.

The time derivative of the porosity appears in the law of mass conservation (Equation 4.6). As the strain-dependent porosity barely changes during the simulations (explained in section 8.3), this term is negligible[2]. If Brinkman's Equation 4.7 is rewritten in terms of the fluid flow $\mathbf{II}$ instead of fluid velocity $\mathbf{v_f}$, the effective viscosity is approximated by the fluid viscosity μ, and the term with the time derivative of the velocity is set to zero (steady state is considered), the equation can be rewritten to:

$$\frac{\rho^f}{\phi^2}\mathbf{q}\cdot\nabla\mathbf{q} = -\nabla\mathbf{P} - \frac{\mu}{k}\mathbf{q} + \frac{\mu}{\phi}\nabla^2\mathbf{q} \tag{8.1}$$

In this equation, the porosity appears in two terms: the convective and viscous term. As the results explained above suggest that the porosity does not influence the pressure or fluid flow, it would mean that these terms are negligible. For clarity, the terms in Brinkman's equation are calculated with an example. The values for the fluid flow, pressure, and their gradients are taken at coordinates $(10, 0)$ mm in the simulation of a hyperelastic tissue and inlet pressure of 40 $mmHg$. In the model, the standard configuration for the porosity (0.51), permeability and viscosity are used (Table 6.1)[3]. Simulations with porosities of e.g., 0.01 and 0.99 would not converge, but nevertheless the theoretical Brinkman's terms can still be calculated. The results are shown in Table 8.4. It can be seen that the convective (a) and viscous (d) terms are a few orders of magnitude smaller compared to the the pressure gradient (b) and fluid flow term (c). Even though the relative contributions of the convective and viscous terms increase with decreasing porosity, they are still negligible compared to the other terms. Therefore, Brinkman's equation can be reduced to Darcy's law in this simulation.

The influence of the viscosity was not analysed in this thesis. The relative contribution of the viscous term (d) could increase for increasing viscosity, even though the relative contribution of the resistance term (d) would increase as well. The influence of the porosity at higher flows (e.g., due to high inlet flow boundary condition that is not necessarily physiological), was also not analysed.

[2]The term becomes more important in e.g., confined compression experiments.

[3]In this case, the equality of Brinkman's Equation 4.7 does not hold. This is because a source term needs to be added to the equation to account for the fluid inflow resulting from the boundary conditions. The difference between the right- and left-hand side of the equation is related to the source term. Still, the example can provide some clarity concerning the relative contributions of each term.

Table 8.3: Influence of the porosity with inlet pressure of 40 $mmHg$. Y denotes the axial direction and X the lateral direction. k is the intrinsic permeability, ε the strain, ε_{vol} the volumetric strain, S the second Piola-Kirchhoff stress, Δ the displacement, and q the fluid flow.

Hyperelastic - Influence of porosity										
ϕ [-]	ε_{YY} [-]	ε_{XX} [-]	ε_{vol} [-]	S_{YY} $[kPa]$	S_{XX} $[kPa]$	ΔY $[m]$	ΔX $[m]$	IFP $[mmHg]$	q_Y $[m/s]$	q_X $[m/s]$
Values at central point $x = 0$ mm										
0.05	-0.04939	0.05371	0.004323	-2.645	2.773	-0.001836	-3.829e-16	23.09	9.937e-18	-2.981e-05
0.50	-0.04939	0.05371	0.004324	-2.644	2.773	-0.001837	-3.417e-16	23.09	6.045e-18	-2.982e-05
0.95	-0.04939	0.05371	0.004324	-2.643	2.773	-0.001837	-3.425e-16	23.09	1.491e-17	-2.982e-05
Values at $x = 10$ mm										
0.05	-0.04962	0.05352	0.003901	-2.892	2.564	-0.001843	4.969e-04	21.33	1.699e-04	-3.057e-05
0.50	-0.04961	0.05352	0.003902	-2.890	2.564	-0.001843	4.968e-04	21.33	1.699e-04	-3.057e-05
0.95	-0.04961	0.05352	0.003902	-2.890	2.564	-0.001843	4.968e-04	21.33	1.699e-04	-3.057e-05
Maximal values along central line $x = [-15\ mm, 15\ mm]$										
0.05	-0.04939	0.05371	0.004323	-2.645	2.773	-0.001836	7.442e-04	23.09	2.565e-04	-2.981e-05
0.50	-0.04939	0.05371	0.004324	-2.644	2.773	-0.001837	7.441e-04	23.09	2.565e-04	-2.982e-05
0.95	-0.04939	0.05371	0.004324	-2.643	2.773	-0.001837	7.441e-04	23.09	2.565e-04	-2.982e-05
Minimal values along central line $x = [-15\ mm, 15\ mm]$										
0.05	-0.04989	0.05326	0.003371	-3.197	2.300	-0.00185	-7.442e-04	19.10	-2.565e-04	-3.074e-05
0.50	-0.04988	0.05325	0.003372	-3.195	2.299	-0.001851	-7.441e-04	19.10	-2.565e-04	-3.075e-05
0.95	-0.04988	0.05325	0.003372	-3.195	2.299	-0.001851	-7.441e-04	19.10	-2.565e-04	-3.075e-05

Table 8.4: Example of terms calculated in Brinkman's equation (units Pa/m) at coordinates $(10, 0)$ mm in a hyperelastic material with inlet pressure of 40 $mmHg$.

	Term							
	a		**b**		**c**		**d**	
	$\frac{\rho^f}{\phi^2}\mathbf{q}\cdot\nabla\mathbf{q}$		$-\nabla\mathbf{P}$		$-\frac{\mu}{k}\mathbf{q}$		$\frac{\mu}{\phi}\nabla^2\mathbf{q}$	
ϕ	X	Y	X	Y	X	Y	X	Y
0.01	2.93e+01	5.27e+00	4.75e+04	-8.36e+03	-4.81e+04	8.65e+03	5.36e-11	-8.70e-12
0.51	1.13e-02	2.03e-03	4.75e+04	-8.36e+03	-4.81e+04	8.65e+03	5.36e-11	-8.70e-12
0.99	2.99e-03	5.38e-04	4.75e+04	-8.36e+03	-4.81e+04	8.65e+03	5.36e-11	-8.70e-12

8.3 Effect of Strain-Dependent Porosity and Permeability

The difference between constant and strain-dependent porosity and permeability are studied on a linear elastic and hyperelastic material. The resulting porosity and permeability distributions in the linear case are shown in Figure 8.2. The resulting porosity and permeability ranges, as well as the SWVs, are provided in Table 8.5. As can be seen from the figures and table, the strain-dependent porosity and permeability only change slightly after pressurisation and don't (significantly) affect the SWV. The compression as a result from the inlet pressure is thus mainly compensated through lateral expansion of the tissue, which can be seen in the figures, instead of a reduction in pore volume and permeability. Therefore, the solid matrix and SWV are not affected significantly by the strain-dependency of the porosity and permeability in these simulations. However, as mentioned before, implementation of the strain-dependency becomes crucial in cases such as confined compression experiments, where compression cannot be compensation by lateral expansion.

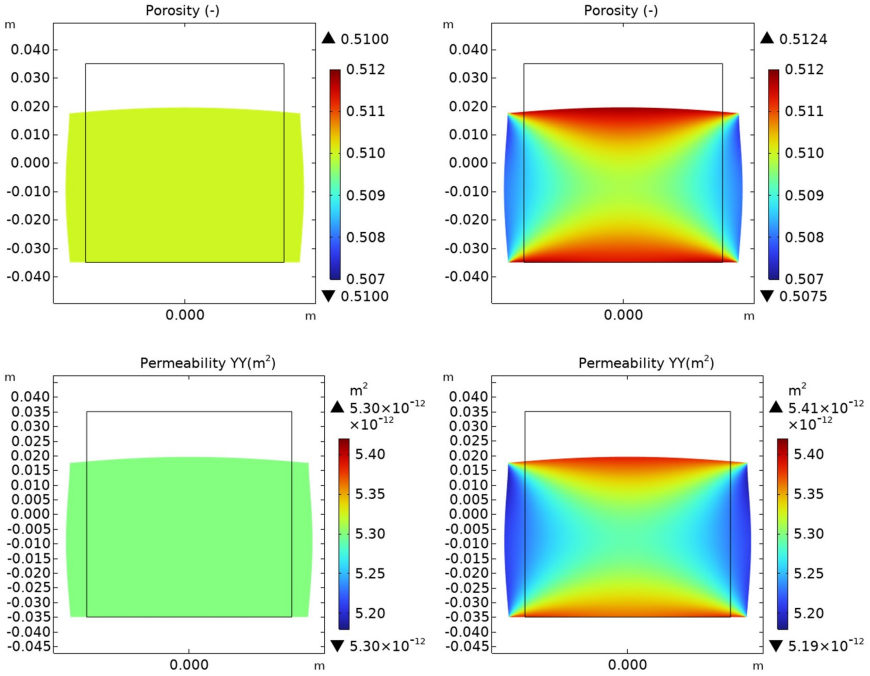

Figure 8.2: Resulting porosity and permeability distribution within a linear elastic tissue ($E = 20\ kPa$) for a model with an inlet pressure of 40 $mmHg$ and constant (left) or strain-dependent (right) poroelastic model. The deformation and initial geometry are shown as well.

Table 8.5: Influence of strain-dependent porosity and permeability on SWV in linear elastic and hyperelastic tissue. The complete geometry is considered for the porosity and permeability values.

Elasticity	**Linear** ($E = 20kPa$)		**Hyperelastic**	
Inlet pressure $[mmHg]$	40		60	
Poroelasticity	**Constant**	**Strain-dependent**	**Constant**	**Strain-dependent**
Porosity [-]	0.510	$0.508 - 0.512$	0.51	$0.509 - 0.516$
Permeability $[\cdot 10^{-12}\ m^2]$	5.30	$5.19 - 5.41$	5.30	$5.23 - 5.58$
Left SWV $[m/s]$	3.13	3.13	6.52	6.50
Right SWV $[m/s]$	3.13	3.13	6.51	6.51

Table 8.6: Influence of strain-dependent porosity and permeability and confinement on hyperelastic model with inlet pressure of 40 $mmHg$. Y denotes the axial direction and X the lateral direction. ϕ is the porosity, k is the intrinsic permeability, ε the strain, ε_{vol} the volumetric strain, S the second Piola-Kirchhoff stress, Δ the displacement, and q the fluid flow. The maximal and minimal values on the central horizontal line within the ROI ($X = [-15\ mm, 15\ mm]$) and the values in the central point ($X = 0\ mm$) and a point on the right($X = 0\ mm$) are given.

Hyperelastic - 60 $mmHg$ **inlet pressure**												
	ε_{YY} [-]	ε_{XX} [-]	ε_{vol} [-]	S_{YY} $[kPa]$	S_{XX} $[kPa]$	ΔY $[m]$	ΔX $[m]$	IFP $[mmHg]$	q_Y $[m/s]$	q_X $[m/s]$	ϕ [-]	k $[m^2]$
Constant poroelasticity - Unconstrained												
Centre	-0.0550	0.06005	5.054e-03	-4.056e+00	4.129e+00	-2.054e-03	-7.861e-17	34.84	-4.877e-05	3.364e-18	0.510	5.30e-12
Right	-0.0553	0.05976	4.431e-03	-4.424e+00	3.821e+00	-2.064e-03	5.505e-04	32.20	-5.025e-05	2.504e-04	0.510	5.30e-12
Max	-0.0550	0.06005	5.054e-03	-4.056e+00	4.129e+00	-2.054e-03	8.242e-04	34.84	-4.877e-05	3.786e-04	0.510	5.30e-12
Min	-0.0557	0.05939	3.653e-03	-4.877e+00	3.431e+00	-2.076e-03	-8.242e-04	28.86	-5.075e-05	-3.786e-04	0.510	5.30e-12
Strain-dependent poroelasticity - Unconstrained												
Centre	-0.0549	0.06009	5.160e-03	-3.990e+00	4.180e+00	-2.052e-03	-1.494e-16	35.28	-4.993e-05	1.181e-17	0.513	5.42e-12
Right	-0.0553	0.05981	4.539e-03	-4.358e+00	3.873e+00	-2.062e-03	5.509e-04	32.65	-5.145e-05	2.548e-04	0.512	5.40e-12
Max	-0.0549	0.06009	5.160e-03	-3.990e+00	4.180e+00	-2.052e-03	8.247e-04	35.28	-4.993e-05	3.853e-04	0.513	5.42e-12
Min	-0.0557	0.05943	3.761e-03	-4.812e+00	3.484e+00	-2.074e-03	-8.247e-04	29.31	-5.196e-05	-3.853e-04	0.512	5.39e-12
Strain-dependent poroelasticity - Constrained												
Centre	-0.0028	0.00283	6.709e-05	-1.525e-02	5.731e-02	4.883e-18	5.958e-18	30.49	9.467e-18	-3.513e-18	0.510	5.30e-12
Right	-0.0028	0.00215	-6.077e-04	-3.532e-01	-2.985e-01	2.787e-18	2.595e-05	27.80	1.894e-17	2.520e-04	0.510	5.29e-12
Max	-0.0027	0.00283	6.709e-05	-1.525e-03	5.731e-02	4.948e-18	3.466e-05	30.49	4.799e-16	3.749e-04	0.510	5.30e-12
Min	-0.0028	0.00128	-1.450e-03	-7.916e-01	-7.438e-01	4.522e-19	-3.466e-05	24.46	-5.180e-16	-3.749e-04	0.509	5.27e-12

8.4 Conclusions

The analyses of this chapter have allowed to assess the influence of different parameters on the solid matrix of the material. The solid phase is coupled to the fluid phase through a body force dependent on the pressure gradient, so parameters that affect the pressure gradient significantly also affect the solid phase. It was shown that using the default configuration of the model, Brinkman's equation could be reduced to Darcy's law due to negligible convective and viscous terms. As a result, porosity did not affect the fluid flow, pressure gradient or solid matrix, but only the fluid velocity (through Equation 4.2).

In the default configuration, the permeability significantly affected the fluid flow but not the pressure drop. It was shown that this was due to the choice of boundary conditions, and that when an inlet flow is applied instead of an inlet pressure, the pressure drop is influenced as well. Furthermore, incorporation of strain-dependent porosity and permeability had a negligible effect on the pressurised tissues, as compression was mainly compensated by lateral expansion of the tissue instead of a reduction in porosity and accompanying reduction in permeability.

9 IFP-SWV Relationship - Healthy Model

The previous chapter mainly analysed the influence of certain parameters on the solid and fluid phase after pressurisation. This chapter examines how the SWV is affected by the fluid pressure.

9.1 Comparison to Theoretical Values - No Pressurisation

In order to ensure that the model is realistic, the estimated SWVs can be compared to the theoretical values. For the linear elastic material model with $E = 20\ kPa$, $\nu = 0.495$, and $\rho^s = 945\ kg/m^3$ the theoretical SWV obtained with Equation 3.6 is 2.66 m/s. For a linear elastic material model with $E = 100\ kPa$, the theoretical value is 5.95 m/s. For the Ogden hyperelastic material model, the initial shear modulus is calculated with Equation 4.9 and using Equation 3.4b, a theoretical SWV of 2.36 m/s is obtained.

The values that are obtained in the computational model when the tissue is not pressurised are shown in Figure 9.1. In these simulations the steady state step (i.e., pressurisation step) is removed and the inlets and outlets replaced by an 'open boundary' through which fluid can enter and leave the tissue [16]. In the hyperelastic non-pressurised case (Figure 9.1c) oscillations are observed that are not present in the linear elastic cases or hyperelastic cases with higher pressures. These oscillations are also visible in Figure 9.5b. This could be induced due to numerical instabilities and results in an inaccurate estimation of the SWV.

And overview of the theoretically calculated and computationally obtained values is provided in Table 9.1. As can be seen from the table, the theoretical values are consistently a bit lower than the computationally obtained values. The higher values could be due to numerical dispersion or poroelastic dispersion. In the linear case, the difference between the theoretically and computationally obtained values are around 2%. This is higher than the 1% threshold that was used in the mesh sensitivity study (section 6.3). However, the mesh sensitivity study was performed with a hyperelastic material model and a pressurized tissue. In the hyperelastic case, the difference is greater ($\approx 19\%$). The discrepancy could be due to the fact that the theoretical values are approximations and/or due to the inaccuracies resulting from the numerical instability explained above. Nevertheless, the comparison with the theoretical values validates the model's ability to provide realistic estimates of the SWV.

Table 9.1: Comparison of the theoretically calculated SWVs and the SWVs obtained through different models.

SWV	**Linear** ($E = 20\ kPa$)	**Linear** ($E = 100\ kPa$)	**Hyperelastic**
Theoretical $[m/s]$	2.66	5.95	2.36
Left $[m/s]$	2.73	6.06	2.90
Right $[m/s]$	2.71	6.07	2.91

9.2 SWV in Pressurised Tissue

In Figures 9.2, 9.3, and 9.4, the influence of pressurisation on the SWV is visualised. More specifically, the relationships between the estimated SWVs and values of the fluid pressure, stresses, and strains in the central point of the model are analysed. A linear (y_1) and quadratic y_2 fit of the mean SWVs (left and right) and the correlation factors (R) with the fitted data are also included in the figures. Not all plots require quadratic fits. When the correlation factor of the linear fit is already approximately equal to one or the first coefficient of the quadratic fit close to zero, a linear relationship can be assumed. Still, it is interesting to include both fits as

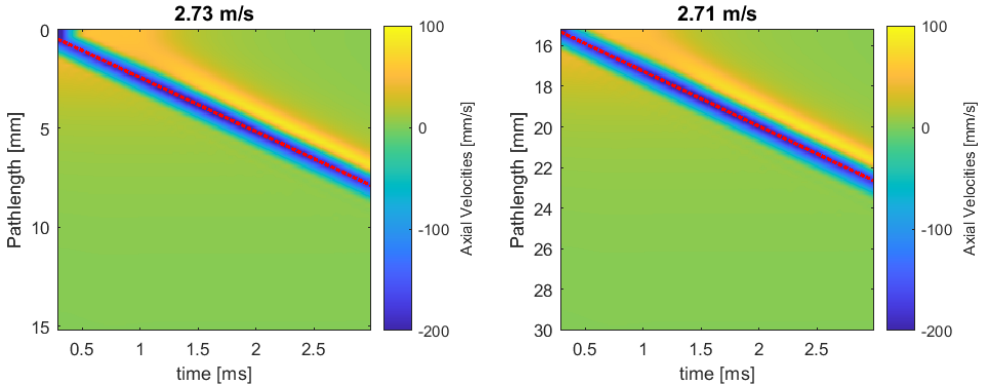

(a) Linear ($E = 20\ kPa$)

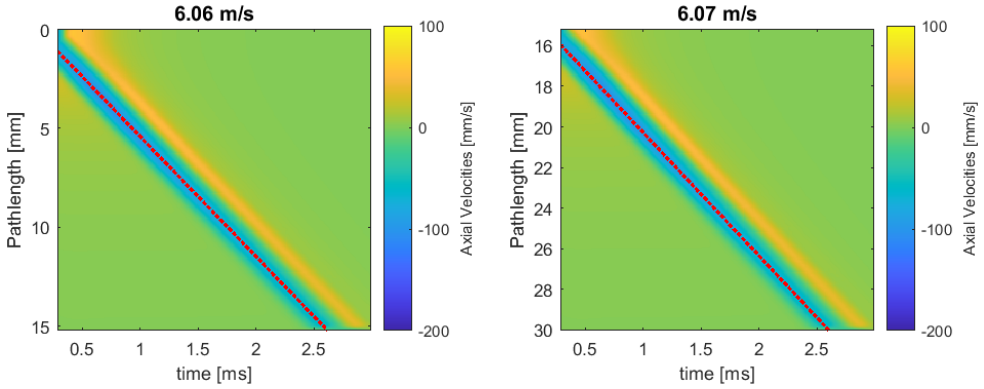

(b) Linear ($E = 100\ kPa$)

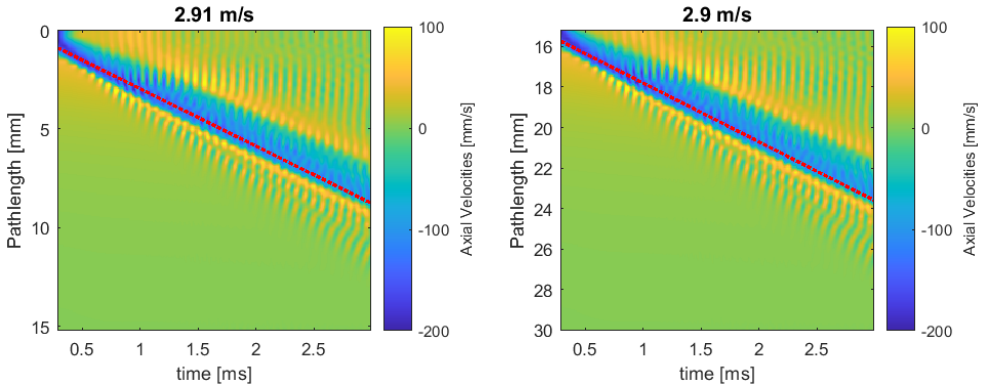

(c) Hyperelastic

Figure 9.1: Estimated SWVs in non-pressurised linear and hyperelastic tissues.

they vary across the material models. Figures of the propagation at different timeframes and pressures can be found in Figure 9.5.

The SWV is dependent on the IFP in both the linear elastic and hyperelastic models. However, a hyperelastic material model is required to observe greater differences in SWVs during pressurisation similarly to the chicken breast experiments (subsection 4.2.1). Recall that the SWV is a measure for the tissue stiffness. In the linear elastic material, the elevated IFP therefore increases the apparent stiffness of the tissue, but not the intrinsic Young's modulus of the solid matrix as mentioned in [14]. A possible explanation for this nonlinear behaviour in a linear elastic material is the nonlinear geometry, i.e., the quadratic term of the strain tensor, as noted in [23]. In the simulations performed in this thesis, the material is not subjected to uniaxial strain in contrast to [23], so it is difficult to compare the SWV to the equations presented in

[23]. Nevertheless, it is interesting to discuss. They observe that when the tissue is compressed in the same direction as the displacement caused by the ARF pulse, the shear wave velocity is related to the shear modulus μ through the relationship $\rho^s c_s^2 = \mu$, i.e., there is no nonlinearity. However, when the tissue is compressed in the direction parallel to the transducer surface (and shear wave propagation also occurs in that direction), the relationship becomes $\rho^s c_s^2 = \mu$, where σ is the uniaxial compression stress. In the simulations, a compressive stress is induced by the inlet pressure in the same direction of the displacement caused by the ARF pulse (axial or Y direction), but a tensile stress in the direction of the shear wave propagation (lateral or X direction) is also present. Therefore, the lateral stress could explain the linear relationship between stress in lateral direction and the shear wave velocity observed in the linear elastic materials.

Hyperelastic tissues show a stiffening behaviour at higher stress, so an additional nonlinear term is present. The results in the hyperelastic case show a slight concave quadratic relationship with the IFP, whereas a linear relationship was observed in the chicken breast experiments (subsection 4.2.1), a convex quadratic relationship in other *ex vivo* experiments (and corresponding analytical derivation) from literature (discussed in subsection 4.2.2)[1], and a concave quadratic relationship in the biomechanical model (discussed in subsection 4.2.3)[2].

The discrepancy between the relationship obtained from the numerical model and the chicken breast experiments could be due to different factors: the pressure range in the chicken breast experiments was maybe not sufficiently large to observe a quadratic relationship, the pressure and/or SWV measurements in the experiments were not accurate enough, or that the material model of the simulations does not correspond adequately to the chicken breast tissue. The discrepancy between the numerical results and experiments explained in subsection 4.2.2 could be caused by the different material models or material parameters. More specifically, a stretch-based strain energy function was used to describe the hyperelastic (Ogden) breast tissue in the numerical model (subsection 4.1.3) and an invariant-based strain energy function was used to describe hepatic tissue in subsection 4.2.2.

In the linear elastic models, and more so in the softer one, the worst fit is obtained when the volumetric strain is considered. A possible explanation could be that the softer linear elastic material deforms much more at higher inlet pressures, and small strains can definitely not be assumed anymore. In contrast, the hyperelastic tissue shows a stiffening behaviour at larger inlet pressures and therefore deforms less.

Table 9.2: SWV for different inlet pressures in linear elastic tissues.

	Linear ($E = 20\ kPa$)					**Linear** ($E = 100\ kPa$)			
IFP inlet $[mmHg]$	0	10	20	30	40	0	15	30	45
IFP centre $[mmHg]$	0	6	13	22	32	0	9	16	25
Left SWV $[m/s]$	2.73	2.83	2.94	3.02	3.13	6.06	6.17	6.25	6.36
Right SWV $[m/s]$	2.71	2.83	2.94	3.02	3.13	6.07	6.17	6.26	6.40

Table 9.3: SWV for different inlet pressures in hyperelastic tissue.

	Hyperelastic					
IFP inlet $[mmHg]$	0	10	20	40	60	120
IFP centre $[mmHg]$	0	5	11	23	35	73
Left SWV $[m/s]$	2.90	3.61	4.41	5.61	6.52	8.57
Right SWV $[m/s]$	2.91	3.60	4.44	5.60	6.51	8.60

[1] Another study used the same analytical model as derived in [51] (that was fitted to the experimental results discussed in subsection 4.2.2), but obtained a concave quadratic relationship [88]. This is shown in the appendix, Figure B.2.

[2] In Figure 4.4, a linear relationship can be seen between the IFP and the square of the SWV. This results in a concave quadratic relationship between the IFP and SWV.

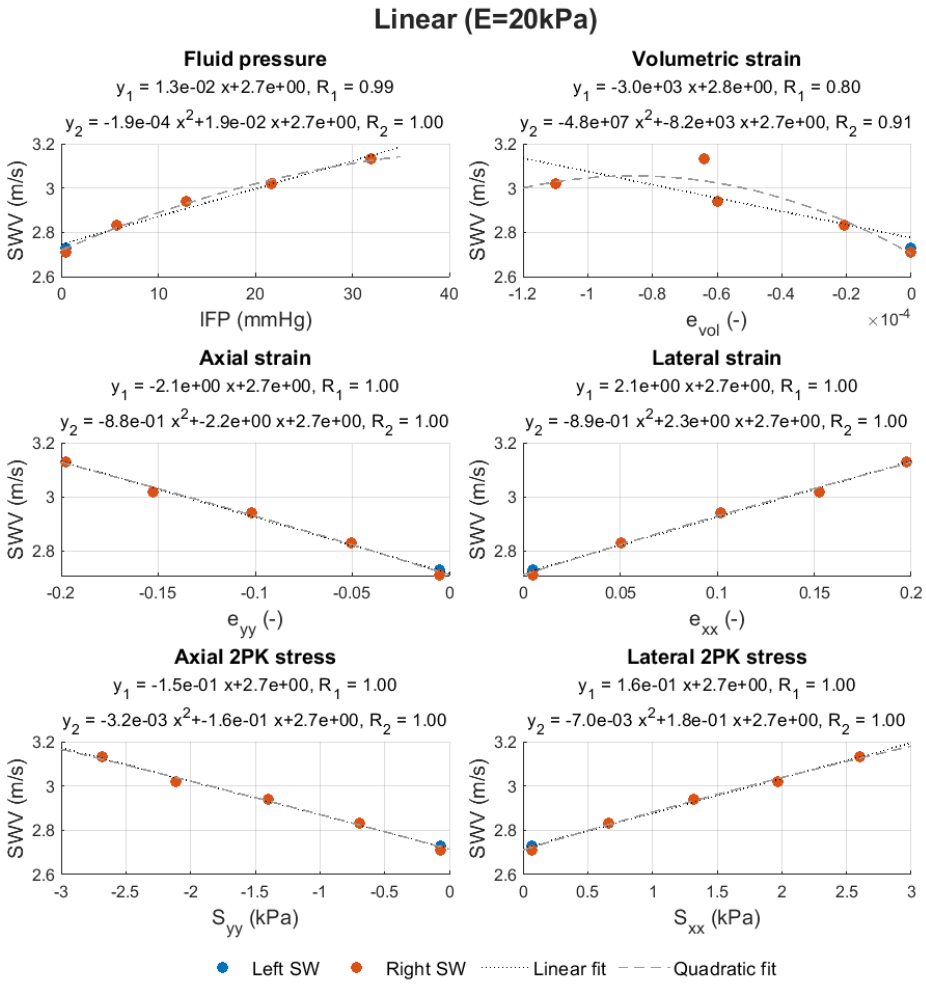

Figure 9.2: Relationship between the SWV and the IFP, strains, and stresses in the centre of the model of a linear elastic ($E = 20\ kPa$) material. A linear and quadratic fit of the mean of the right and left SWV is provided.

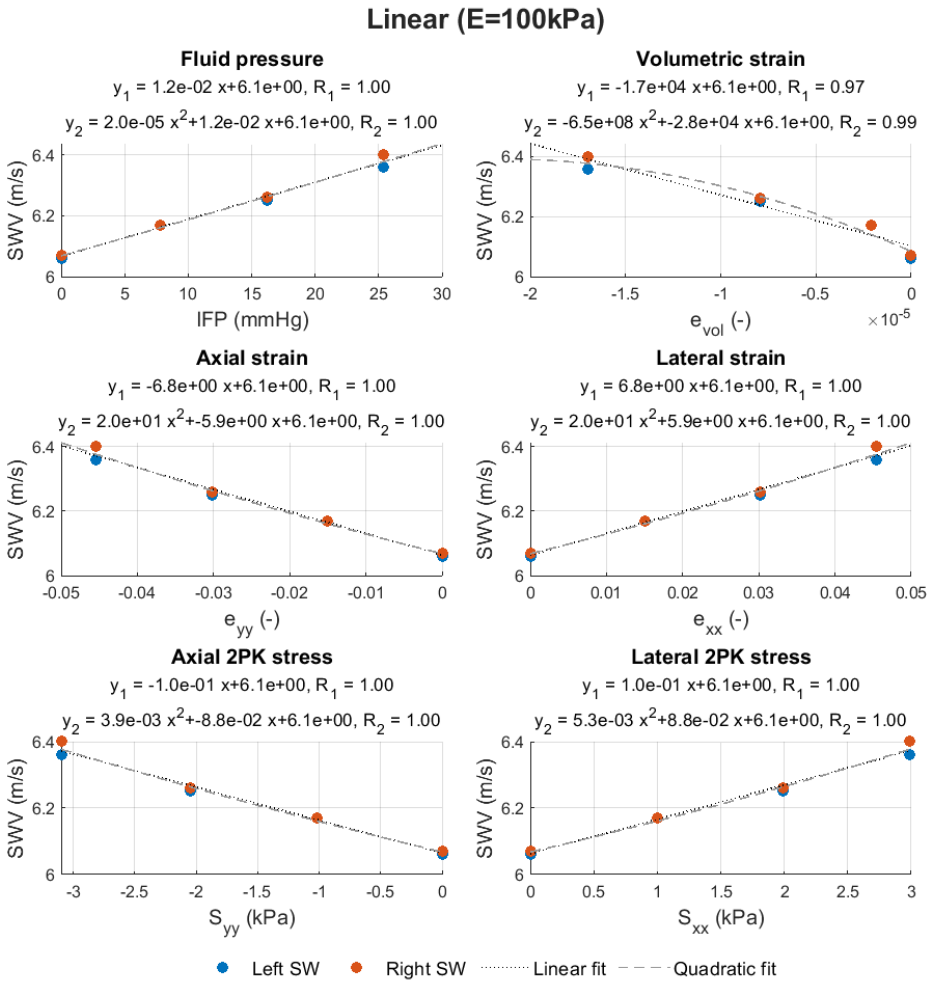

Figure 9.3: Relationship between the SWV and the IFP, strains, and stresses in the centre of the model of a linear elastic ($E = 100\ kPa$) material. A linear and quadratic fit of the mean of the right and left SWV is provided.

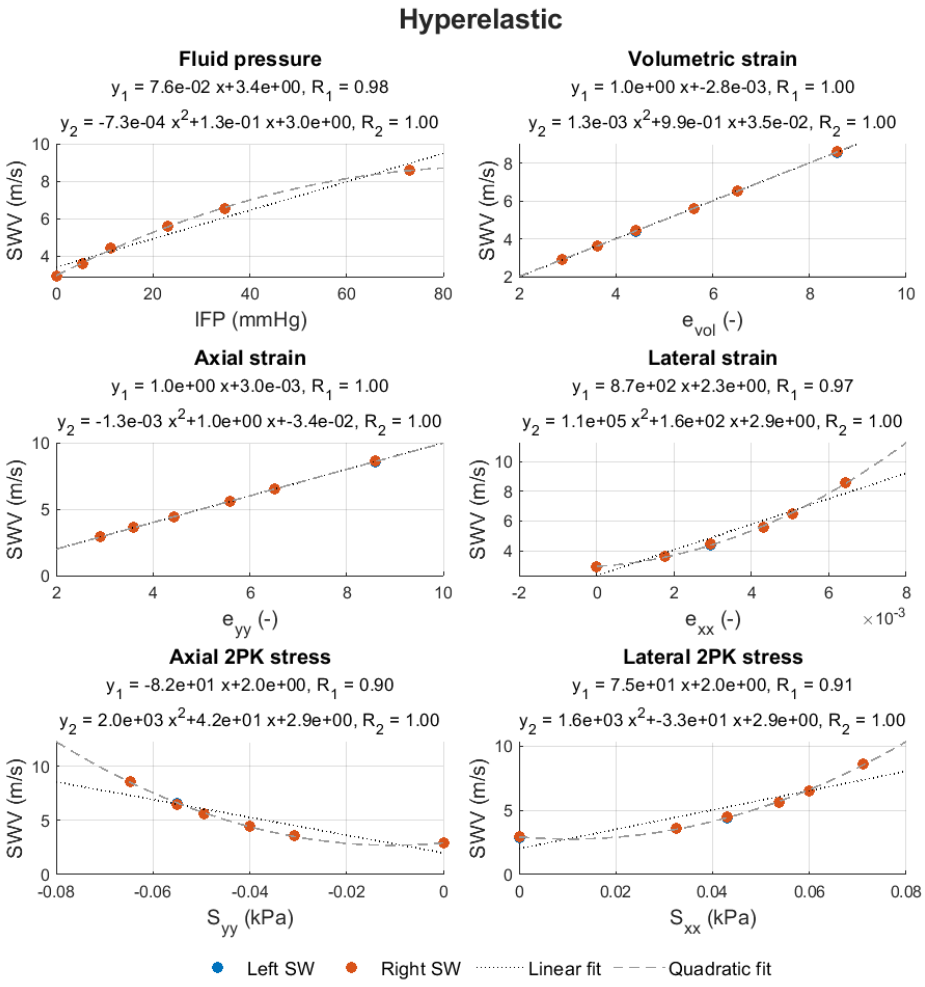

Figure 9.4: Relationship between the SWV and the IFP, strains, and stresses in the centre of the model of a hyperelastic material. A linear and quadratic fit of the mean of the right and left SWV is provided.

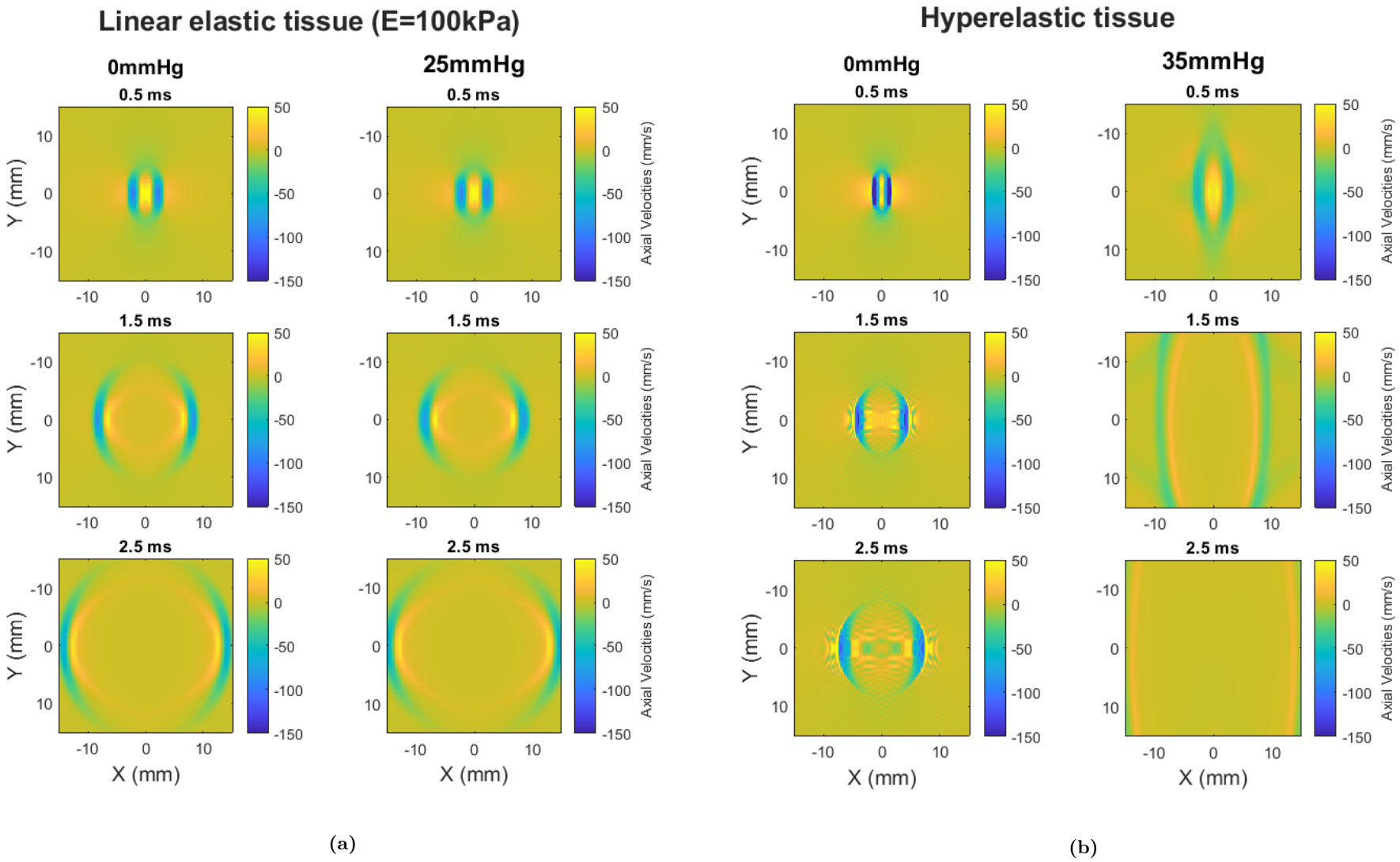

Figure 9.5: Shear wave propagation in pressurised and non-pressurised linear elastic (a) and hyperelastic (b) tissues for three different timeframes. The IFP in the centre is shown.

9.3 Effect of Confinement - After Pressurisation

As the experiments mentioned in subsection 4.2.2 observed an increase in SWV with IFP, but only if the tissue was unconstrained, this influence is also examined on the numerical model. Constrained simulations are performed, where rollers are placed on all four boundaries. In Table 9.4, the resulting SWVs are compared to the unconstrained and non-pressurised cases. Certain values for the stresses, strains, and displacement in the constrained and unconstrained pressurised hyperelastic tissue can be found in Table 8.6.

In the linear case, it can indeed be observed that the SWV is equivalent to the non-pressurised velocity, whereas higher SWVs are recorded in the pressurised and unconstrained model. In the hyperelastic case, a substantial difference between the pressurised constrained and unconstrained cases are observed. In the constrained case, the SWV is similar to the non-pressurised state but slightly lower, which could be due to the numerical instabilities mentioned in section 9.1. Therefore, it is confirmed that the fluid pressure itself is not sufficient to observe an increase in SWV with IFP, and that stresses and/or strains need to be taken into account as well.

Table 9.4: Comparison of the SWVs in constrained and unconstrained simulations. Measures given at centre

Linear ($E = 20\ kPa$)			
Deformation	**Unconstrained**	**Unconstrained**	**Constrained**
Inlet pressure $[mmHg]$	0	40	40
Left SWV $[m/s]$	2.73	3.12	2.72
Right SWV $[m/s]$	2.71	3.13	2.71
IFP_{centre} $[mmHg]$	0	32	32
Hyperelastic			
Deformation	**Unconstrained**	**Unconstrained**	**Constrained**
Inlet pressure [mmHg]	0	60	60
Left SWV $[m/s]$	2.90	6.52	2.78
Right SWV $[m/s]$	2.91	6.51	2.73

9.4 Conclusions

This chapter was mainly focused on analysing the computationally obtained SWVs. First and foremost, the comparison of the SWVs in non-pressurised tissues to theoretical SWVs allowed to confirm that realistic values can be obtained with the model for both linear elastic and hyperelastic tissues. Secondly, elevated IFP noticeably affected the SWV and this effect was compared to experimental values and analytical models defined in literature. More specifically, IFP increased the apparent stiffness of the tissue. In the linear elastic material, geometric nonlinearity could explain this behaviour. In hyperelastic tissues, an additional nonlinear term is introduced due to the stiffening behaviour (i.e., nonlinear shear modulus). Mostly linear relationships were observed between the SWV and the IFP, stresses, and strains in the linear elastic material. Conversely, mostly quadratic relationships were observed in the hyperelastic tissue. Finally, numerical experiments confirmed that the effect of IFP is limited in constrained tissues.

10 Clinical Implementation - Tumour Model

The objective of this thesis was to analyse the relationship between the IFP and SWV, which was done in the previous chapter. In this chapter, a supplementary model is evaluated. This model includes a tumour mass surrounded by healthy tissue, and allows to study the combined and separate influence of the IFP and stiffness. The analyses are performed on linear elastic tissues to avoid the numerical instabilities discussed in the previous chapter.

10.1 Pressurisation

A mass source in the fluid domain is comparable to an inlet flow. Therefore, the mass source (magnitude and radius) and tissue permeability influence the pressure as discussed in a previous chapter (section 8.1). These parameters can be changed to obtain realistic pressures and pressure distributions within the model. Their influence on the pressure is visualised in Figure 10.1. It can be seen that the tumour permeability mainly influences the pressure drop within the tumour, and not the pressure distribution within the healthy tissue. More specifically, fluid flow through the tumour pores is hindered at lower permeabilities, increasing the pressure drop.

On the other hand, the mass source magnitude and radius affect both the pressure drop within the tumour as the pressure within the healthy tissue. As expected, an increasing magnitude or radius increases the fluid flow and thus also the pressure within the model. In the subsequent simulations, the following values are selected as 'default' configuration: mass source magnitude of 300 $kg/(m^3 s)$ with radius of 6 mm, tumour permeability of $1 \cdot 10^{-12}$ m^2, and linear elasticity ($E = 100$ kPa). The resulting pressure, stress, and strain distributions after pressurisation are shown in the Appendix, Figure B.3.

10.2 Shear Wave Propagation

The shear wave propagation in the tumour model is analysed in three different cases, as summarised in Table 10.1. The influence of a pressurised less permeable and non-pressurised stiffer tumour are assessed separately first, and then their combined effect is analysed. The estimated SWVs and propagation plots for the three different cases in the tumour model are shown in Figures 10.2 and 10.3. In the less permeable case, the shear wave traversing the tumour (i.e., right shear wave) propagates faster as expected from the previous chapter, but no marked difference in the waveform is be observed. This is different in the stiffer case. As expected, the shear wave propagates faster in the stiffer tissue, and this is clearly visible in Figure 10.2b (right) due to the discontinuity in the blue trajectory when the tumour tissue is reached. But additionally, shear waves are reflected when they reach the stiffer tissue.

Finally, the SWV in the healthy tissue in the combined case slightly higher than in 'stiffer' case, as the pressure is slightly elevated throughout the healthy tissue and drops to zero at the borders as explained in the previous section. The SWV in the tumour is now lower than in the pressurised (less permeable) case, but this is due to the discontinuity in the blue trajectory at the intersection of the healthy and tumour tissue. If the healthy tissue in the right propagating shear wave is discarded, a similar SWV is obtained (as shown in the Appendix, Figure B.4).

10.3 Conclusions

The feasibility of including a tumour mass was examined in this chapter. It was shown that a mass source within the tumour could be employed to obtain an elevated pressure within the tumour and that the mass source magnitude, mass source radius, and tumour permeability can be adapted to obtain a desired pressure distribution in the healthy and tumour tissue. Finally,

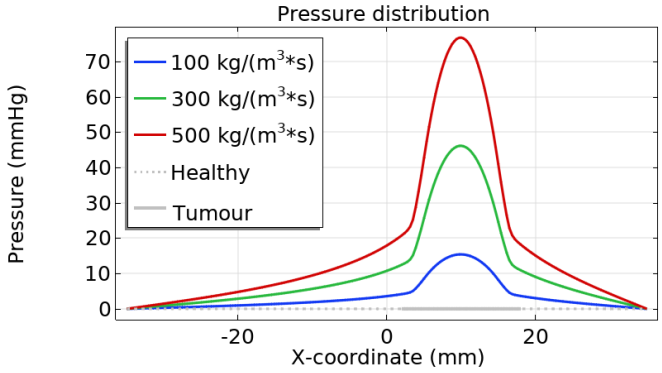

(a) Influence of mass source magnitude.

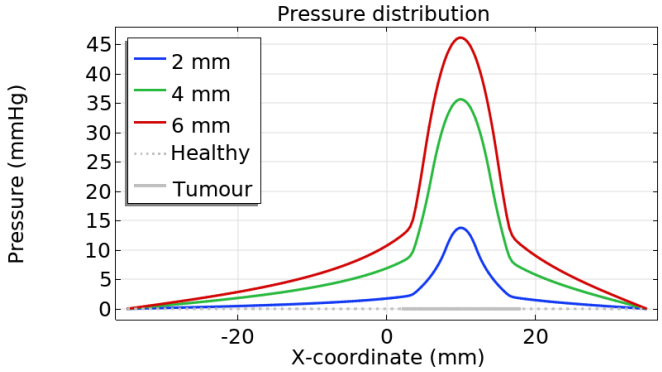

(b) Influence of mass source radius.

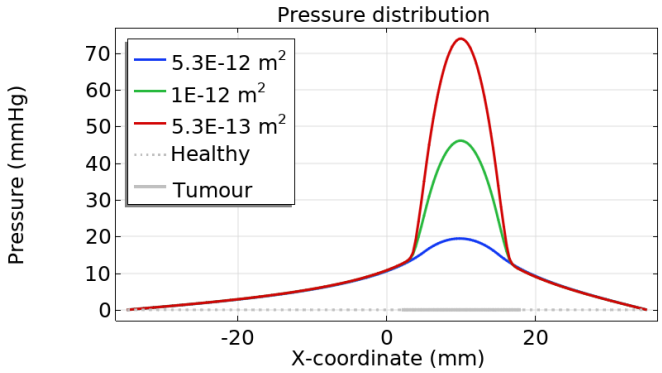

(c) Influence of tumour permeability.

Figure 10.1: Influence of the mass source magnitude (a), mass source radius (b), and tumour permeability (c) on the pressure distribution within the central horizontal line of the model. The default values during the analysis are a mass source magnitude of 300 $kg/(m^3 s)$, mass source radius of 6 mm, and tumour permeability of $1 \cdot 10^{-12}$ m^2. A linear elastic ($E = 100$ kPa) is used throughout the complete geometry.

Table 10.1: Overview of cases in linear tumour model. The magnitude and radius of the mass sources are, respectively, 300 $kg/(m^3 s)$ and 6 mm.

Property	**Healthy tissue**	**Tumour tissue**
Case 1 - Less permeable		
Young's modulus $[kPa]$	100	100
Permeability $[m^2]$	$5.3 \cdot 10^{-12}$	$1 \cdot 10^{-12}$
Mass source	N/A	Yes
Case 2 - Stiffer		
Young's modulus $[kPa]$	20	100
Permeability $[m^2]$	$5.3 \cdot 10^{-12}$	$5.3 \cdot 10^{-12}$
Mass source	N/A	No
Case 3 - Combined		
Young's modulus $[kPa]$	20	100
Permeability $[m^2]$	$5.3 \cdot 10^{-12}$	$1 \cdot 10^{-12}$
Mass source	N/A	Yes

the shear wave propagation was analysed in the tumour model. Both the pressurisation and tissue stiffness increase the shear wave velocity, which was already the case in the previous chapter. Additionally, it was observed that a difference in tissue stiffness causes reflections.

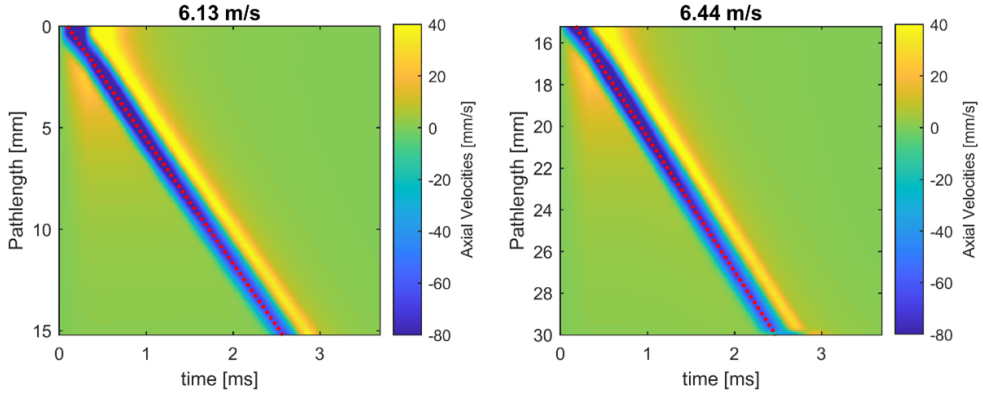

(a) Less permeable

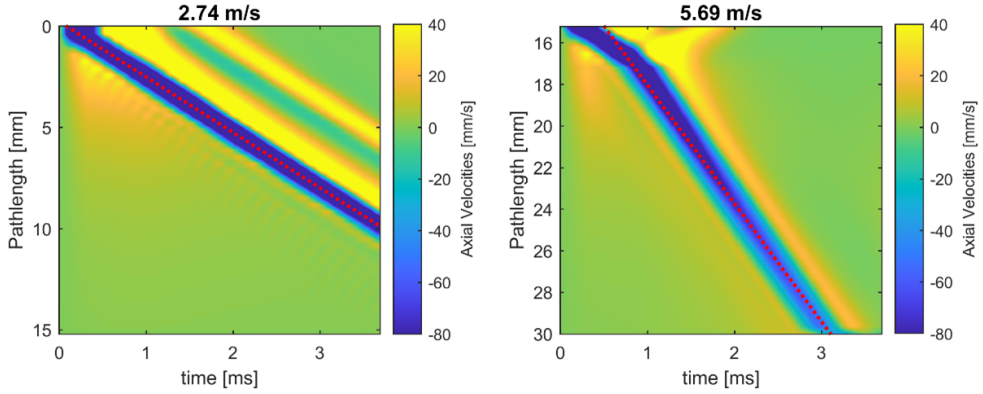

(b) Stiffer

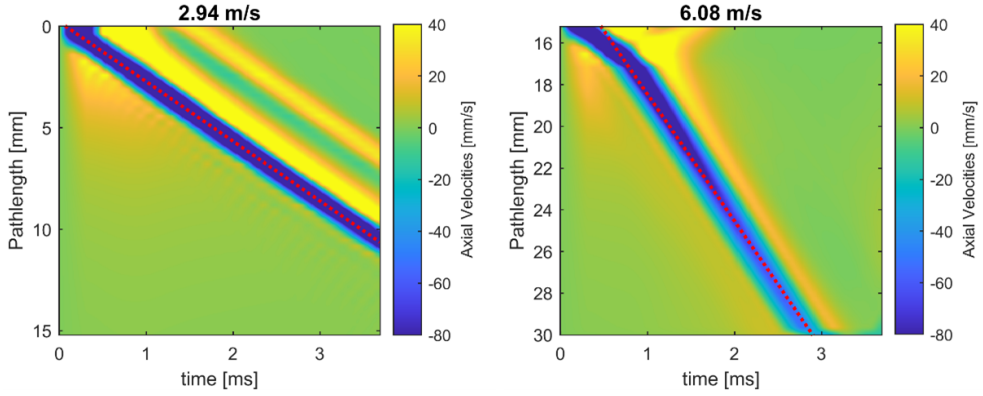

(c) Combination

Figure 10.2: SWVs of left and right propagating shear waves in tumour model. The tumour tissue starts at 17 mm. In the 'less permeable' case, the tumour and healthy tissue have the same linear elastic properties ($E = 100\ kPa$), but the tumour has a permeability of $1 \cdot 10^{-12}\ m^2$ and the healthy tissue a permeability of $5.3 \cdot 10^{-12}\ m^2$. In the 'stiffer' case, the linear elastic properties of the tumour ($E = 100\ kPa$) are different from the healthy tissue ($E = 20\ kPa$), but both tissues have the same permeability. In the 'combined' case, the tumour is stiffer and less permeable.

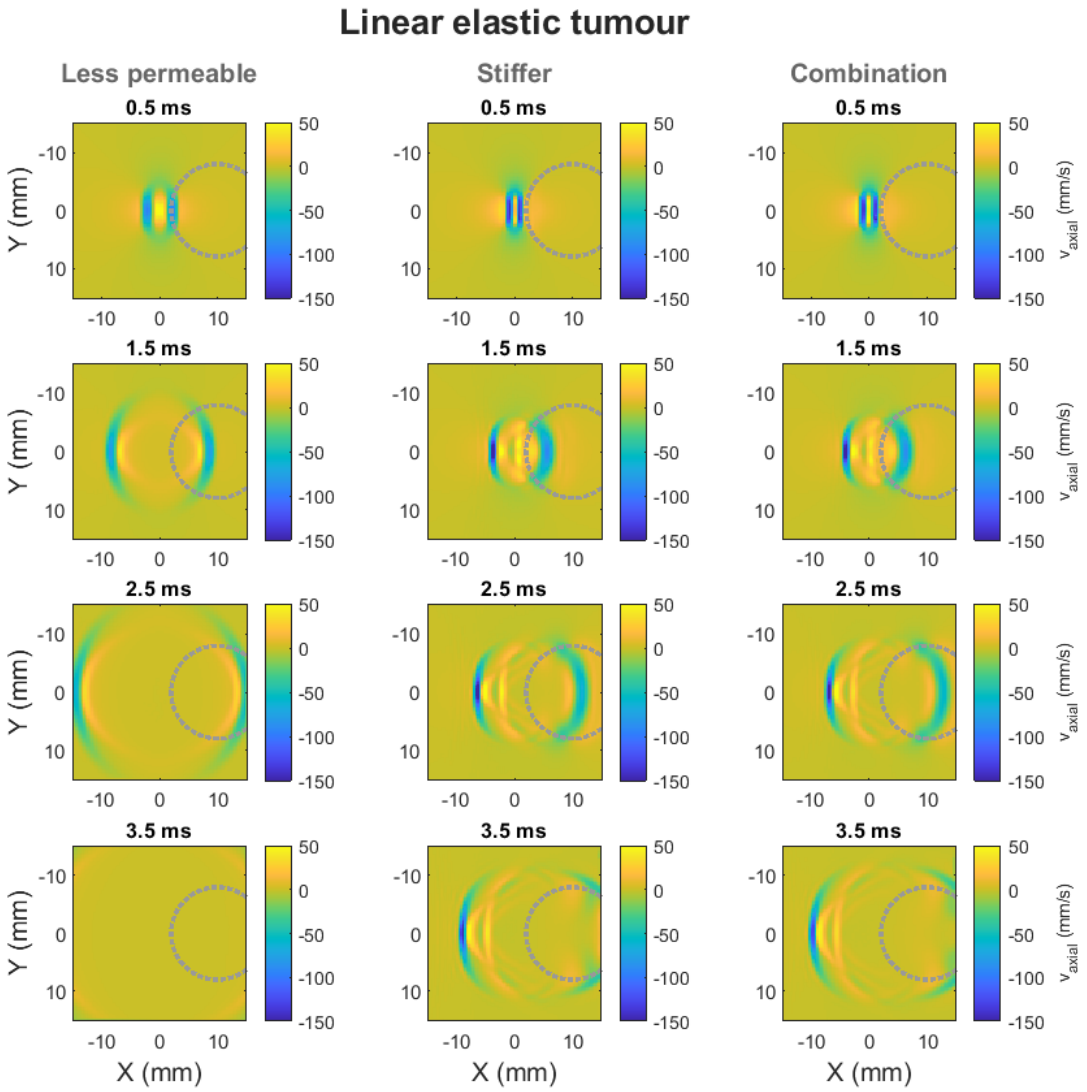

Figure 10.3: Shear wave propagation in linear elastic tumour model at different timeframes. The tumour geometry is indicated. In the 'less permeable' column, the tumour and healthy tissue have the same linear elastic properties ($E = 100\ kPa$), but the tumour has a permeability of $1 \cdot 10^{-12}\ m^2$ and the healthy tissue a permeability of $5.3 \cdot 10^{-12}\ m^2$. In the 'stiffer' column, the linear elastic properties of the tumour ($E = 100\ kPa$) are different from the healthy tissue ($E = 20\ kPa$), but both tissues have the same permeability. In the 'combined' column, the tumour is stiffer and less permeable.

11 General Conclusions

The objective of this thesis was to study the relationship between the IFP and SWV. In this regard, a poroelastic tissue was manually implemented into COMSOL Multiphysics® as validated by [74]. The material model was further extended to include hyperelasticity and strain-dependent porosity and permeability. The influence of the strain-dependency during pressurisation turned out to be limited in these models, but would be crucial in other applications involving higher strains.

The fluid and solid phase are related to each other through the fluid pressure gradient and solid volumetric strain. Pressurisation was obtained through different boundary conditions. Inlet pressures and mass sources were mainly discussed in this thesis. When fixed pressures were applied, permeability had a limited impact on the solid matrix properties as the pressure gradient was fixed. This changed when a fluid mass source was used instead. Higher permeabilities increased the pressure drop within tissues in this case. The porosity showed to have an insignificant effect on the solid matrix or on the pressure drop as convective and viscous terms were negligible. In these cases, Brinkman's equation reduces to Darcy's law.

The healthy model has proven to produce realistic estimates of the SWV in non-pressurised tissues compared to theoretical values. Numerical instabilities did occur in the hyperelastic tissue at zero or low IFP, and this should be resolved in future models to enable more accurate SWV estimation. Furthermore, clear correlations between the IFP and SWV were obtained in both linear and hyperelastic tissues. More specifically, elevated IFP increases the apparent stiffness of the tissue. Moreover, the tissue has to be unconstrained or order to observe the correlation.

Finally, a tumour mass was included in the model and allowed to compare the influence of pressurisation and intrinsic stiffness in both healthy and tumour tissues.

11.1 Limitations and Perspectives

In the models' current configuration, determination of the absolute value of the IFP within a tissue is not yet possible without knowledge of the tissue parameters, as comparison of the tumour SWV with adjacent tissues is not sufficient to decouple the influence of tumour stiffness and IFP. Therefore, only the variation in fluid pressure over time can be determined in a first stage, which would already be useful for monitoring the efficacy of treatments designed to lower the IFP over time that aim to improve uptake of other therapeutic drugs to the tumour. Moreover, the variation in fluid pressure could also be assessed in other pressure-related disorders, such as oedema.

In a second stage, the models developed in this thesis can serve as a basis to test whether additional measurements in the time and/or frequency domain can allow to characterise the tissue and fluid pressure. For example, Gennisson et al. [23] found that it is possible to characterise the nonlinear shear elasticity in one single shear wave experiment using different applied uniaxial stresses, instead of three different shear wave experiments with different polarisation directions. Similarly, supplementary tests adapted to the models could allow for additional parameters to be assessed.

11.2 Future Work

Future work can be divided in multiple phases: (1) limiting numerical dispersion and instabilities in the current models, (2) analysing the influence of additional parameters on the SWV in the current models, and (3) extending the models' complexity to encompass other clinical applications. In the first phase, the mesh in the tumour should be optimised through a mesh

sensitivity study and numerical instabilities in the hyperelastic tissue should be resolved. The second phase can analyse the influence of poroelastic and viscoelastic dispersion [1, 89] (which requires modelling in the frequency domain and inclusion of viscoelasticity), an increased fluid viscosity, and a compressible solid matrix [89] on the SWV. Finally, the models can be extended to 3D and anisotropic tissues to, amongst others, examine irregularly-shaped (tumour) geometries and IFP in tendinopathies.

Bibliography

[1] J. Aichele and S. Catheline. 'Fluids Alter Elasticity Measurements: Porous Wave Propagation Accounts for Shear Wave Dispersion in Elastography'. In: *Frontiers in Physics* 9 (2021). ISSN: 2296-424X. DOI: 10.3389/fphy.2021.697990. URL: https://www.frontiersin.org/articles/10.3389/fphy.2021.697990.

[2] M. Arbel-Ornath, E. Hudry, K. Eikermann-Haerter, S. Hou, J. L. Gregory, L. Zhao, R. A. Betensky, M. P. Frosch, S. M. Greenberg, and B. J. Bacskai. 'Interstitial fluid drainage is impaired in ischemic stroke and Alzheimer's disease mouse models'. In: *Acta Neuropathologica* 126.3 (July 2013), pp. 353–364. DOI: https://doi.org/10.1007/s00401-013-1145-2.

[3] A. B. Ariffin, P. F. Forde, S. Jahangeer, D. M. Soden, and J. Hinchion. 'Releasing Pressure in Tumors: What Do We Know So Far and Where Do We Go from Here? A Review'. In: *Cancer Research* 74.10 (May 2014), pp. 2655–2662. DOI: https://doi.org/10.1158/0008-5472.can-13-3696.

[4] A. Atangana. 'Principle of Groundwater Flow'. In: *Fractional Operators with Constant and Variable Order with Application to Geo-Hydrology* (2018), pp. 15–47. DOI: https://doi.org/10.1016/b978-0-12-809670-3.00002-3.

[5] G. Ateshian, W. Warden, J. Kim, R. Grelsamer, and V. Mow. 'Finite deformation biphasic material properties of bovine articular cartilage from confined compression experiments'. In: *Journal of Biomechanics* 30.11 (1997), pp. 1157–1164. DOI: https://doi.org/10.1016/S0021-9290(97)85606-0.

[6] P. E. Beshay, M. G. Cortes-Medina, M. M. Menyhert, and J. W. Song. 'The Biophysics of Cancer: Emerging Insights from Micro- and Nanoscale Tools'. In: *Advanced NanoBiomed Research* 2.1 (Nov. 2021), p. 2100056. DOI: https://doi.org/10.1002/anbr.202100056.

[7] M. A. Biot. 'Mechanics of Deformation and Acoustic Propagation in Porous Media'. In: *Journal of Applied Physics* 33.4 (June 2004), pp. 1482–1498. DOI: 10.1063/1.1728759.

[8] J. E. Brinkman, B. Dorius, and S. Sharma. *Physiology, Body Fluids*. May 2022. URL: https://www.ncbi.nlm.nih.gov/books/NBK482447.

[9] V. L. D. S. N. Button. 'Chapter 2 - Electrodes for Biopotential Recording and Tissue Stimulation'. In: *Principles of Measurement and Transduction of Biomedical Variables*. Ed. by V. L. D. S. N. Button. Oxford: Academic Press, 2015, pp. 25–76. ISBN: 978-0-12-800774-7. DOI: https://doi.org/10.1016/B978-0-12-800774-7.00002-7.

[10] D. Cacko and M. Lewandowski. 'Shear Wave Elastography Implementation on a Portable Research Ultrasound System: Initial Results'. In: *Applied Sciences* 12.12 (2022). DOI: 10.3390/app12126210. URL: https://www.mdpi.com/2076-3417/12/12/6210.

[11] A. Caenen. 'A biomechanical analysis of shear wave elastography in pediatric heart models'. eng. PhD thesis. Ghent University, 2018, p. 244. ISBN: 978-94-6355-100-7.

[12] A. Caenen, M. Pernot, K. R. Nightingale, J.-U. Voigt, H. J. Vos, P. Segers, and J. D'hooge. 'Assessing cardiac stiffness using ultrasound shear wave elastography'. In: *Physics in Medicine & Biology* 67.2 (Jan. 2022), 02TR01. DOI: 10.1088/1361-6560/ac404d.

[13] A. L. Castro, J. Yao, T. Battisti, and D. Lacroix. 'Poroelastic Modeling of Highly Hydrated Collagen Hydrogels: Experimental Results vs. Numerical Simulation With Custom and Commercial Finite Element Solvers'. In: *Frontiers in Bioengineering and Biotechnology* 6.142 (Oct. 2018). DOI: https://doi.org/10.3389/fbioe.2018.00142.

[14] A. Chaudhry, N. Kim, G. Unnikrishnan, S. Nair, J. N. Reddy, and R. Righetti. 'Effect of Interstitial Fluid Pressure on Ultrasound Axial Strain and Axial Shear Strain Elastography'. In: *Ultrasonic Imaging* 39.2 (2017), pp. 137–146. DOI: 10.1177/0161734616671713.

[15] COMSOL. *COMSOL Multiphysics Reference Manual 5.5*. 2019. URL: https://doc.comsol.com/5.5/doc/com.comsol.help.comsol/COMSOL_ReferenceManual.pdf.

[16] COMSOL. *Porous Media Flow Module User's Guide 5.6*. 2020. URL: https://doc.comsol.com/5.6/doc/com.comsol.help.porous/PorousMediaFlowModuleUsersGuide.pdf.

[17] COMSOL. *Low-Reflecting Boundary Condition*. URL: https://doc.comsol.com/5.5/doc/com.comsol.help.sme/sme_ug_theory.06.57.html (visited on 05/14/2023).

[18] COMSOL. *Perfectly Matched Layers (PMLs)*. URL: https://doc.comsol.com/5.5/doc/com.comsol.help.aco/aco_ug_pressure.05.106.html (visited on 05/14/2023).

[19] E. DETOURNAY and A. H.-D. CHENG. '5 - Fundamentals of Poroelasticity'. In: *Analysis and Design Methods*. Ed. by C. FAIRHURST. Oxford: Pergamon, 1993, pp. 113–171. ISBN: 978-0-08-040615-2. DOI: https://doi.org/10.1016/B978-0-08-040615-2.50011-3.

[20] W. Ehlers. 'Darcy, Forchheimer, Brinkman and Richards: classical hydromechanical equations and their significance in the light of the TPM'. In: *Archive of Applied Mechanics* 92.2 (Oct. 2020), pp. 619–639. DOI: https://doi.org/10.1007/s00419-020-01802-3.

[21] S. Ferretti, P. R. Allegrini, M. Becquet, and P. M. McSheehy. 'Tumor Interstitial Fluid Pressure as an Early-Response Marker for Anticancer Therapeutics'. In: *Neoplasia* 11.9 (Sept. 2009), pp. 874–881. DOI: https://doi.org/10.1593/neo.09554.

[22] M. Friedel, I. A. P. Thompson, G. Kasting, R. Polsky, D. Cunningham, H. T. Soh, and J. Heikenfeld. 'Opportunities and challenges in the diagnostic utility of dermal interstitial fluid'. In: *Nature Biomedical Engineering* (Jan. 2023). DOI: https://doi.org/10.1038/s41551-022-00998-9.

[23] J.-L. Gennisson, M. Rénier, S. Catheline, C. Barrière, J. Bercoff, M. Tanter, and M. Fink. 'Acoustoelasticity in soft solids: Assessment of the nonlinear shear modulus with the acoustic radiation force'. In: *The Journal of the Acoustical Society of America* 122.6 (Dec. 2007), pp. 3211–3219. DOI: 10.1121/1.2793605.

[24] K. M. Graczyk and M. Matyka. 'Predicting porosity, permeability, and tortuosity of porous media from images by deep learning'. In: *Scientific Reports* 10.1 (Dec. 2020). DOI: https://doi.org/10.1038/s41598-020-78415-x.

[25] E. V. Gubarkova et al. 'Nonlinear Elasticity Assessment with Optical Coherence Elastography for High-Selectivity Differentiation of Breast Cancer Tissues'. In: *Materials* 15.9 (May 2022), p. 3308. DOI: 10.3390/ma15093308.

[26] C. F. Guimarães, L. Gasperini, A. P. Marques, and R. L. Reis. 'The stiffness of living tissues and its implications for tissue engineering'. In: *Nature Reviews Materials* 5 (2020), pp. 351–370.

[27] L. Guta and S. Sundar. 'Navier-Stokes-Brinkman system for interaction of viscous waves with a submerged porous structure'. In: *Tamkang Journal of Mathematics* 41.3 (Sept. 2010), pp. 217–243. DOI: 10.5556/j.tkjm.41.2010.722.

[28] J. E. Hall and A. C. Guyton. *Guyton and hall textbook of medical physiology*. 12th ed. Saunders Elsevier, 2010.

[29] J. E. Hall and A. C. Guyton. *Guyton and hall textbook of medical physiology*. 11th ed. Saunders Elsevier, 2010.

[30] C.-H. Heldin, K. Rubin, K. Pietras, and A. Östman. 'High interstitial fluid pressure — an obstacle in cancer therapy'. In: *Nature Reviews Cancer* 4.10 (Oct. 2004), pp. 806–813. DOI: https://doi.org/10.1038/nrc1456.

[31] K. Holkova. 'Shear wave elastography for assessing interstitial fluid pressure: a combined computational-experimental study'. Master's thesis. Ghent University, 2022.

[32] M. Holmes and V. Mow. 'The nonlinear characteristics of soft gels and hydrated connective tissues in ultrafiltration'. In: *Journal of Biomechanics* 23.11 (Jan. 1990), pp. 1145–1156. DOI: https://doi.org/10.1016/0021-9290(90)90007-p.

[33] M. T. Islam, S. Tang, E. Tasciotti, and R. Righetti. 'Non-Invasive Assessment of the Spatial and Temporal Distributions of Interstitial Fluid Pressure, Fluid Velocity and Fluid Flow in Cancers In Vivo'. In: *IEEE Access* 9 (2021), pp. 89222–89233. DOI: 10.1109/ACCESS.2021.3089454.

[34] F. Q. Jin, A. E. Knight, C. T. Paley, L. S. Pietrosimone, L. D. Hobson-Webb, K. R. Nightingale, and M. L. Palmeri. 'An Open-Source Radon-Transform Shear Wave Speed Estimator with Masking Functionality to Isolate Different Shear-Wave Modes'. In: *2022 IEEE International Ultrasonics Symposium (IUS)*. 2022, pp. 1–4. DOI: 10.1109/IUS54386.2022.9957817.

[35] A.-R. Khaled and K. Vafai. 'The role of porous media in modeling flow and heat transfer in biological tissues'. In: *International Journal of Heat and Mass Transfer* 46.26 (2003), pp. 4989–5003. ISSN: 0017-9310. DOI: https://doi.org/10.1016/S0017-9310(03)00301-6.

[36] H.-G. Kim, A. R. Yu, J. J. Lee, Y.-J. Lee, S. M. Lim, and J. S. Kim. 'Measurement of Tumor Pressure and Strategies of Imaging Tumor Pressure for Radioimmunotherapy'. In: *Nuclear Medicine and Molecular Imaging* 53.4 (June 2019), pp. 235–241. DOI: https://doi.org/10.1007/s13139-019-00598-7.

[37] E. E. Konofagou, T. P. Harrigan, J. Ophir, and T. A. Krouskop. 'Poroelastography: imaging the poroelastic properties of tissues'. In: *Ultrasound in Medicine & Biology* 27.10 (2001), pp. 1387–1397. ISSN: 0301-5629. DOI: https://doi.org/10.1016/S0301-5629(01)00433-1.

[38] H. Kumar. *MODULE 3: PRESSURE MEASUREMENT*. 2020. URL: https://www.acsce.edu.in/acsce/wp-content/uploads/2020/03/BMT-18BM45-MODULE-3.pdf.

[39] W. M. Lai, V. C. Mow, and V. Roth. 'Effects of Nonlinear Strain-Dependent Permeability and Rate of Compression on the Stress Behavior of Articular Cartilage'. In: *Journal of Biomechanical Engineering* 103.2 (May 1981), pp. 61–66. DOI: 10.1115/1.3138261.

[40] S. Locke. 'The effect of interstitial pressure on tumour stiffness'. Master's thesis. University of Toronto, 2014.

[41] P. Lyu. *Which Porous Media and Subsurface Flow Interface Should I Use?* Feb. 2017. URL: https://www.comsol.com/blogs/which-porous-media-and-subsurface-flow-interface-should-i-use/ (visited on 05/14/2023).

[42] A. Malandrino and E. Moeendarbary. 'Poroelasticity of Living Tissues'. In: *Encyclopedia of Biomedical Engineering*. Ed. by R. Narayan. Elsevier, 2019, pp. 238–245. ISBN: 978-0-12-805144-3. DOI: https://doi.org/10.1016/B978-0-12-801238-3.99932-X.

[43] K. Manda and A. Eriksson. 'Time-dependent behavior of cartilage surrounding a metal implant for full-thickness cartilage defects of various sizes: a finite element study'. In: *Biomechanics and Modeling in Mechanobiology* 11.5 (Sept. 2011), pp. 731–742. DOI: https://doi.org/10.1007/s10237-011-0346-7.

[44] K. Manda and A. Eriksson. 'Modeling of constrained articular cartilage growth in an intact knee with focal knee resurfacing metal implant'. In: *Biomechanics and Modeling in Mechanobiology* 13.3 (Aug. 2013), pp. 599–613. DOI: https://doi.org/10.1007/s10237-013-0521-0.

[45] S. Moavenzadeh, M. L. Palmeri, G. Ferraioli, and R. G. Barr. 'CHAPTER 3 - Liver stiffness measurement techniques: Basics'. In: *Multiparametric Ultrasound for the Assessment of Diffuse Liver Disease*. Ed. by R. G. Barr and G. Ferraioli. New Delhi: Elsevier, 2024, pp. 25–34. ISBN: 978-0-323-87479-3. DOI: https://doi.org/10.1016/B978-0-323-87479-3.00012-0.

[46] M. C. Moghadam, A. Deyranlou, A. Sharifi, and H. Niazmand. 'Numerical simulation of the tumor interstitial fluid transport: Consideration of drug delivery mechanism'. In: *Microvascular Research* 101 (Sept. 2015), pp. 62–71. DOI: https://doi.org/10.1016/j.mvr.2015.06.007.

[47] H. J. Moon, J. M. Sung, E. K. Kim, J. H. Yoon, J. H. Youk, and J. Y. Kwak. 'Diagnostic Performance of Gray-Scale US and Elastography in Solid Thyroid Nodules'. In: *Radiology* 262.3 (Mar. 2012), pp. 1002–1013. DOI: https://doi.org/10.1148/radiol.11110839.

[48] S. Narod, J. Iqbal, A. Jakubowska, T. Huzarski, P. Sun, C. Cybulski, J. Gronwald, T. Byrski, and J. Lubinski. 'Are Two-Centimeter Breast Cancers Large or Small?' In: *Current Oncology* 20.4 (Aug. 2013), pp. 205–211. DOI: https://doi.org/10.3747/co.20.1364.

[49] National Cancer Institute. *Intersitial fluid*. URL: https://www.cancer.gov/publications/dictionaries/cancer-terms/def/interstitial-fluid (visited on 03/17/2023).

[50] National Institute of Neurological Disorders and Stroke. URL: https://www.ninds.nih.gov/health-information/disorders/hydrocephalus (visited on 04/30/2023).

[51] N. Nazari and P. Barbone. 'Shear wave speed in pressurized soft tissue'. In: *Journal of the Mechanics and Physics of Solids* 119 (2018), pp. 60–72. ISSN: 0022-5096. DOI: https://doi.org/10.1016/j.jmps.2018.06.009.

[52] H. T. Nia, L. L. Munn, and R. K. Jain. 'Mapping Physical Tumor Microenvironment and Drug Delivery'. In: *Clinical Cancer Research* 25.7 (Apr. 2019), pp. 2024–2026. ISSN: 1078-0432. DOI: 10.1158/1078-0432.CCR-18-3724. eprint: https://aacrjournals.org/clincancerres/article-pdf/25/7/2024/2058905/2024.pdf. URL: https://doi.org/10.1158/1078-0432.CCR-18-3724.

[53] K. Nightingale. 'Acoustic Radiation Force Impulse (ARFI) Imaging: A Review'. In: *Current Medical Imaging Reviews* 7.4 (Jan. 2011), pp. 328–339. DOI: https://doi.org/10.2174/157340511798038657.

[54] U. Ozerdem. 'Measuring interstitial fluid pressure with fiberoptic pressure transducers'. In: *Microvascular Research* 77.2 (2009), pp. 226–229. ISSN: 0026-2862. DOI: https://doi.org/10.1016/j.mvr.2008.08.002. URL: https://www.sciencedirect.com/science/article/pii/S0026286208001313.

[55] U. Ozerdem and A. R. Hargens. 'A simple method for measuring interstitial fluid pressure in cancer tissues'. In: *Microvascular Research* 70.1 (2005), pp. 116–120. ISSN: 0026-2862. DOI: https://doi.org/10.1016/j.mvr.2005.07.003. URL: https://www.sciencedirect.com/science/article/pii/S0026286205000646.

[56] A. Ozturk, J. R. Grajo, M. Dhyani, B. W. Anthony, and A. E. Samir. 'Principles of ultrasound elastography'. In: *Abdominal radiology (New York)* 43.4 (Apr. 2018), pp. 773–785. DOI: https://doi.org/10.1007/s00261-018-1475-6.

[57] G. Pagé, P. Garteiser, and B. E. Van Beers. 'Magnetic resonance elastography of malignant tumors'. In: *Frontiers in Physics* 10 (2022). ISSN: 2296-424X. DOI: 10.3389/fphy.2022.910036. URL: https://www.frontiersin.org/articles/10.3389/fphy.2022.910036.

[58] M. L. Palmeri, B. Qiang, S. Chen, and M. W. Urban. 'Guidelines for Finite-Element Modeling of Acoustic Radiation Force-Induced Shear Wave Propagation in Tissue-Mimicking Media'. In: *IEEE Transactions on Ultrasonics, Ferroelectrics, and Frequency Control* 64.1 (2017), pp. 78–92. DOI: 10.1109/TUFFC.2016.2641299.

[59] S. Park, S. R. Aglyamov, W. G. Scott, S. Y. Emelianov, S. Sethuraman, J. M. Rubin, J. Shah, A. B. Karpiouk, S. Mallidi, and R. W. Smalling. '1E-5 Synergy and Applications of Combined Ultrasound, Elasticity, and Photoacoustic Imaging (Invited)'. In: *2006 IEEE Ultrasonics Symposium*. 2006, pp. 405–415. DOI: 10.1109/ULTSYM.2006.114.

[60] Pathway Medicine. *Starling Forces*. URL: http://www.pathwaymedicine.org/starling-forces (visited on 04/14/2023).

[61] P. R. Perrinez, F. E. Kennedy, E. E. W. V. Houten, J. B. Weaver, and K. D. Paulsen. 'Modeling of Soft Poroelastic Tissue in Time-Harmonic MR Elastography'. In: *IEEE Transactions on Biomedical Engineering* 56.3 (2009), pp. 598–608. DOI: 10.1109/TBME.2008.2009928.

[62] J. J. Pitre and J. L. Bull. 'Imaging the Mechanical Properties of Porous Biological Tissue'. In: *Handbook of Thermal Science and Engineering* (2018), pp. 831–857. DOI: https://doi.org/10.1007/978-3-319-26695-4_38.

[63] P. J. Prendergast, W. D. van Driel, and J.-H. Kuiper. 'A Comparison of Finite Element Codes for the Solution of Biphasic Poroelastic Problems'. In: *Proceedings of the Institution of Mechanical Engineers, Part H: Journal of Engineering in Medicine* 210.2 (1996), pp. 131–136. DOI: 10.1243/PIME_PROC_1996_210_402_02.

[64] M. Ramazanilar and A. Mojra. 'Characterization of breast tissue permeability for detection of vascular breast tumors: An in vitro study'. In: *Materials Science and Engineering: C* 107 (2020), p. 110222. ISSN: 0928-4931. DOI: https://doi.org/10.1016/j.msec.2019.110222.

[65] D. Rosen and J. Jiang. 'Analyzing acoustoelastic effect of shear wave elastography data for perfused and hydrated soft tissues using a macromolecular network inspired model'. In: *Journal of Biomechanics* 97 (2019), p. 109370. ISSN: 0021-9290. DOI: https://doi.org/10.1016/j.jbiomech.2019.109370.

[66] V. Rotemberg, M. Palmeri, R. Nightingale, N. Rouze, and K. Nightingale. 'The impact of hepatic pressurization on liver shear wave speed estimates in constrained versus unconstrained conditions'. In: *Physics in Medicine & Biology* 57.2 (Dec. 2011), p. 329. DOI: 10.1088/0031-9155/57/2/329. URL: https://dx.doi.org/10.1088/0031-9155/57/2/329.

[67] V. Rotemberg, M. L. Palmeri, N. C. Rouze, R. Nightingale, and K. R. Nightingale. 'Comparison between Acoustic Radiation Force Impulse (ARFI)-based hepatic stiffness quantification in deformed and undeformed pressurized canine livers'. In: *2011 IEEE International Ultrasonics Symposium*. 2011, pp. 2090–2093. DOI: 10.1109/ULTSYM.2011.0518.

[68] N. C. Rouze, M. H. Wang, M. L. Palmeri, and K. R. Nightingale. 'Robust estimation of time-of-flight shear wave speed using a radon sum transformation'. In: *IEEE Transactions on Ultrasonics, Ferroelectrics, and Frequency Control* 57.12 (2010), pp. 2662–2670. DOI: 10.1109/TUFFC.2010.1740.

[69] N. C. Rouze, M. H. Wang, M. L. Palmeri, and K. R. Nightingale. 'Parameters affecting the resolution and accuracy of 2-D quantitative shear wave images'. In: *IEEE Transactions on Ultrasonics, Ferroelectrics, and Frequency Control* 59.8 (2012), pp. 1729–1740. DOI: 10.1109/TUFFC.2012.2377.

[70] H. Salavati, C. Debbaut, P. Pullens, and W. Ceelen. 'Interstitial fluid pressure as an emerging biomarker in solid tumors'. In: *Biochimica et Biophysica Acta (BBA) - Reviews on Cancer* 1877.5 (Sept. 2022), p. 188792. DOI: https://doi.org/10.1016/j.bbcan.2022.188792.

[71] A. Sanchez, C. Mills, and J. C. Scurr. 'Estimating Breast Mass-Density: A Retrospective Analysis of Radiological Data'. In: *The Breast Journal* 23 (2017).

[72] M. Sarntinoranont, F. Rooney, and M. Ferrari. 'Interstitial stress and fluid pressure within a growing tumor'. In: 31.3 (2003), pp. 327–335. DOI: 10.1114/1.1554923.

[73] R. M. Sigrist, J. Liau, A. E. Kaffas, M. C. Chammas, and J. K. Willmann. 'Ultrasound Elastography: Review of Techniques and Clinical Applications'. In: *Theranostics* 7.5 (2017), pp. 1303–1329. DOI: https://doi.org/10.7150/thno.18650. URL: http://thno.org/v07p1303.pdf.

[74] C. A. Silvera Delgado. 'Modeling the interaction between lymphatic capillaries and interstitium'. Master's thesis. Politecnico di Torino, 2022.

[75] M. Soltani and P. Chen. 'Numerical Modeling of Fluid Flow in Solid Tumors'. In: *PLOS ONE* 6.6 (June 2011), pp. 1–15. DOI: 10.1371/journal.pone.0020344.

[76] D. R. Sowinski, M. D. J. McGarry, E. E. W. Van Houten, S. Gordon-Wylie, J. B. Weaver, and K. D. Paulsen. 'Poroelasticity as a Model of Soft Tissue Structure: Hydraulic Permeability Reconstruction for Magnetic Resonance Elastography in Silico'. In: *Frontiers in Physics* 8 (2021). DOI: 10.3389/fphy.2020.617582.

[77] R. M. Spielman, W. J. Jenkins, and M. D. Lovett. *Psychology 2e*. OpenStax, Apr. 2020. ISBN: 9781951693312. URL: https://openstax.org/details/books/psychology-2e.

[78] R. H. Stewart. 'A Modern View of the Interstitial Space in Health and Disease'. In: *Frontiers in Veterinary Science* 7 (Nov. 2020). DOI: https://doi.org/10.3389/fvets.2020.609583.

[79] M. Taffetani, M. Griebel, D. Gastaldi, S. Klisch, and P. Vena. 'Poroviscoelastic finite element model including continuous fiber distribution for the simulation of nanoindentation tests on articular cartilage'. In: *Journal of the Mechanical Behavior of Biomedical Materials* 32 (2014), pp. 17–30. ISSN: 1751-6161. DOI: https://doi.org/10.1016/j.jmbbm.2013.12.003.

[80] L. Tan, M. D. J. McGarry, E. E. W. Van Houten, M. Ji, L. Solamen, W. Zeng, J. B. Weaver, and K. D. Paulsen. 'A numerical framework for interstitial fluid pressure imaging in poroelastic MRE'. In: *PLOS ONE* 12.6 (June 2017). Ed. by A. A. Oberai, e0178521. DOI: https://doi.org/10.1371/journal.pone.0178521.

[81] Theranostics. *Ultrasound Elastography: Review of Techniques and Clinical Applications*. 2017. URL: https://www.thno.org/v07p1303.htm (visited on 05/18/2023).

[82] UT Southwestern Department of Radiology. *Ultrasound - Liver Elastography*. Jan. 2023. URL: https://www.utsouthwestern.edu/education/medical-school/departments/radiology/protocols/us.html.

[83] F. J. Valdes-Parada, J. Alberto Ochoa-Tapia, and J. Alvarez-Ramirez. 'On the effective viscosity for the Darcy–Brinkman equation'. In: *Physica A: Statistical Mechanics and its Applications* 385.1 (2007), pp. 69–79. DOI: https://doi.org/10.1016/j.physa.2007.06.012.

[84] C. Wex, S. Arndt, A. Stoll, C. Bruns, and Y. Kupriyanova. 'Isotropic incompressible hyperelastic models for modelling the mechanical behaviour of biological tissues: a review'. In: *Biomedical Engineering / Biomedizinische Technik* 60.6 (2015), pp. 577–592. DOI: doi:10.1515/bmt-2014-0146.

[85] H. Wiig, R. K. Reed, and K. Aukland. 'Measurement of interstitial fluid pressure: Comparison of methods'. In: *Annals of Biomedical Engineering* 14.2 (Mar. 1986), pp. 139–151. DOI: https://doi.org/10.1007/bf02584264.

[86] W. Wilson, B. van Rietbergen, C. van Donkelaar, and R. Huiskes. 'Pathways of load-induced cartilage damage causing cartilage degeneration in the knee after meniscectomy'. In: *Journal of Biomechanics* 36.6 (2003), pp. 845–851. ISSN: 0021-9290. DOI: https://doi.org/10.1016/S0021-9290(03)00004-6.

[87] Y. Zhang, J. Tang, Y.-m. Li, X. Fei, E.-h. He, Q.-y. Li, and H.-y. Shi. 'The contribution of strain patterns in characterization of prostate peripheral zone lesions at transrectal ultrasonography'. In: *Acta Radiologica* 53.1 (2012), pp. 119–126. DOI: 10.1258/ar.2011.110504.

[88] Y. Zheng, Y. Jiang, and Y. Cao. 'A porohyperviscoelastic model for the shear wave elastography of the liver'. In: *Journal of the Mechanics and Physics of Solids* 150 (2021), p. 104339. ISSN: 0022-5096. DOI: https://doi.org/10.1016/j.jmps.2021.104339.

[89] Y. Zheng, Y. Jiang, and Y. Cao. 'Effects of interstitial fluid pressure on shear wave elastography of solid tumors'. In: *Extreme Mechanics Letters* 47 (2021), p. 101366. ISSN: 2352-4316. DOI: https://doi.org/10.1016/j.eml.2021.101366. URL: https://www.sciencedirect.com/science/article/pii/S2352431621001140.

[90] J. Zhou, W. Zhan, C. Chang, X. Zhang, Y. Jia, Y. Dong, C. Zhou, J. Sun, and E. G. Grant. 'Breast Lesions: Evaluation with Shear Wave Elastography, with Special Emphasis on the "Stiff Rim" Sign'. In: *Radiology* 272.1 (July 2014), pp. 63–72. DOI: https://doi.org/10.1148/radiol.14130818.

A Appendix - Ethical Considerations

A.1 Ethical aspects directly related to the work done in the thesis

No *in vivo* or *ex vivo* experiments were performed during this thesis. Numerical results were compared to data of *ex vivo* experiments on chicken breasts performed in [31] and to results available in literature [66]. Material parameters were mainly taken from literature, and focused on (female) breast tissue. However, the material parameters don't have to be sex-specific and can be adapted easily.

A.2 Reflection about the potential (future) impact of study results

The impact of the work performed in this thesis could potentially allow for SWE to be used in a clinical context for assessment of the IFP, and improve diagnosis and treatment of tumours, as current techniques for the assessment of IFP are invasive and therefore not widely implemented into clinical practise. Besides its applications in oncology, non-invasive assessment of IFP could also be used in other clinical fields and pathologies, such as oedemas and tendinopathies. Moreover, as IFP affects the apparent tissue stiffness, estimation of this property could be improved by considering the effect of IFP on the SWV.

SWE can be performed with conventional ultrasound transducers, as long as they allow for high-energy burst transmission, high-frame rate data acquisition, and dispose of the adequate software (which requires an additional cost) [10]. This equipment and additional cost might be difficult to cover in low-resource settings. However, ultrasound-based techniques are still cheaper than MRI-based techniques.

On another note, the strain-dependent poroelastic model developed in this thesis can also be adapted to enable modelling of other soft (biological) tissues in COMSOL Multiphysics®.

A.3 Scientific integrity

Information retrieved from literature was consistently followed or preceded by the appropriate reference. For figures and tables that were sourced from literature, the corresponding reference was provided in the caption. If the figure or table was adapted, this was also mentioned in the caption. When no reference was included in the caption of a figure or table, it was created from scratch.

This thesis is a continuation of the master's thesis of Kristyna Holkova [31]. The models that she developed were provided by her and subsequently improved and adapted in this thesis. The code for the shear wave velocity estimation from 2D data was provided by Dr. Ir. Annette Caenen and adapted to fit the data obtained from the computational model.

No numerical results were omitted in this thesis, but results that provided no additional information than what was already discussed, were not always included. For example, the results of all three linear ($E = 20\ kPa$ and $E = 100\ kPa$) and hyperelastic cases for each part of the parameteric study were not always shown, instead, priority was given to one or two of these cases.

The literature study, discussions with knowledgeable researchers (e.g., counsellor Dr. Ir. Annette Caenen), and personal experience with modelling all contributed to the work performed in this thesis.

B Appendix - Supplementary Information

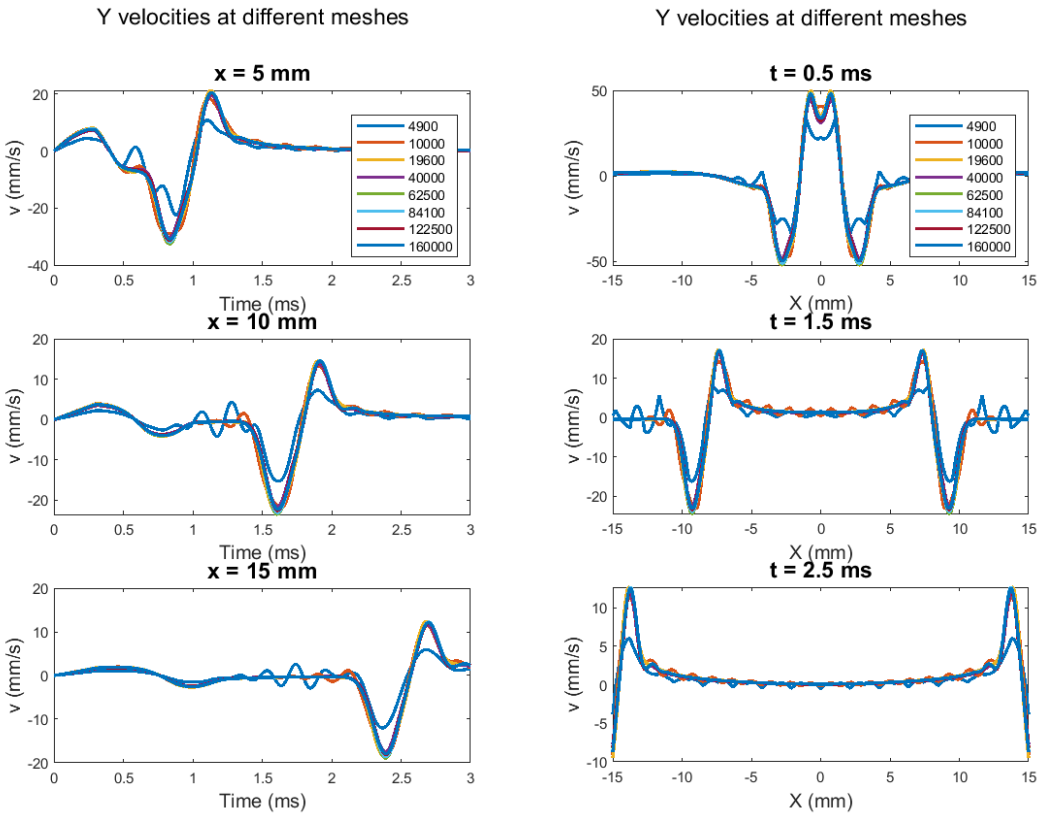

Figure B.1: Y velocities at different x-coordinates and timeframes for the different meshes of section 6.3.

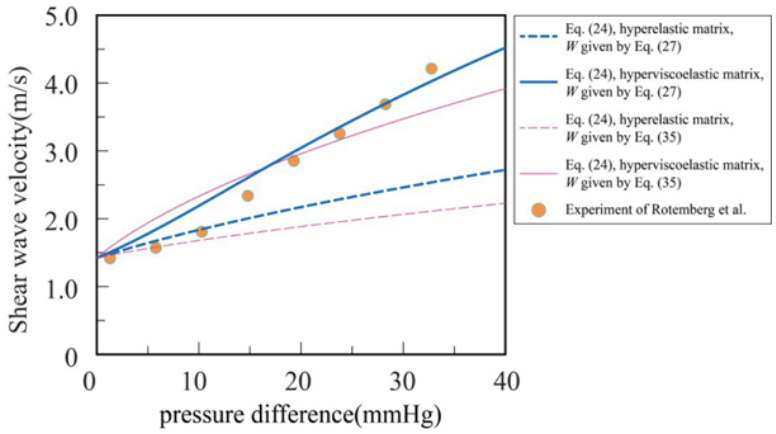

Figure B.2: IFP-SWV relationship obtained by [88]. The dashed pink line (third in the legend) employs the same analytical model as derived in [51] and discussed in subsection 4.2.2. [88]

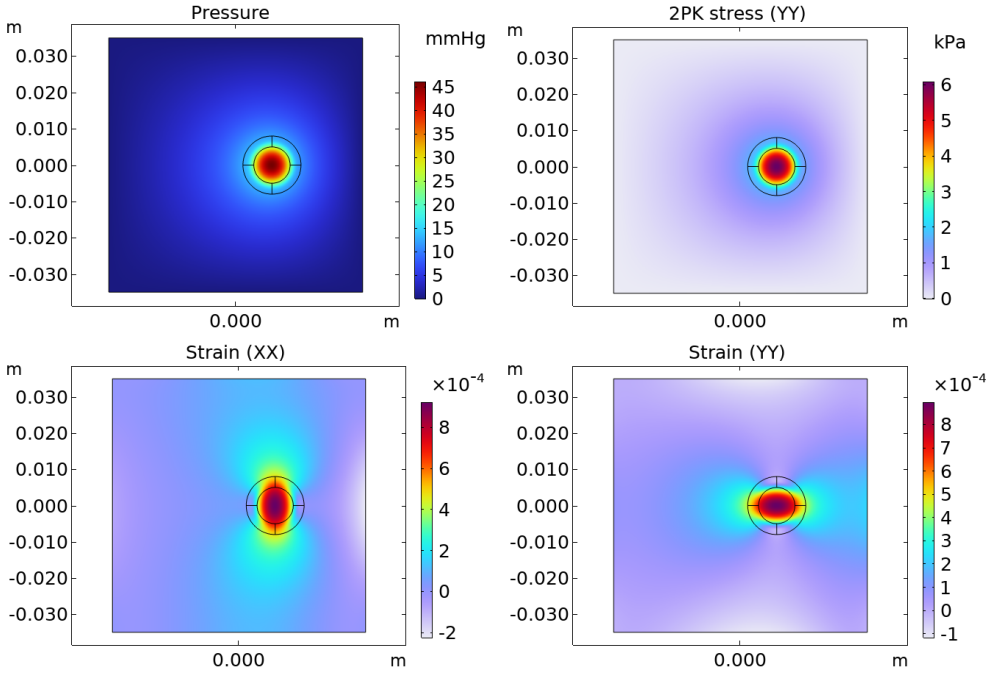

Figure B.3: Resulting pressure, stress, and strain distribution in the default tumour model.

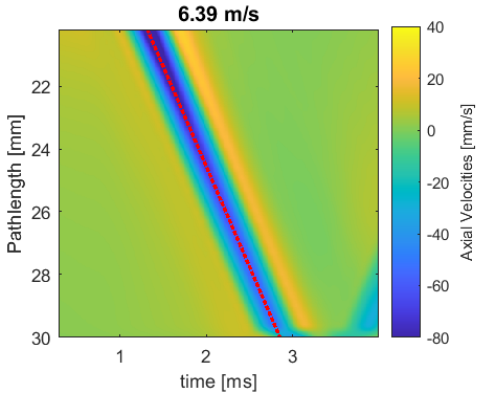

Figure B.4: Right SWV in the tumour model case 3 if the healthy tissue is not considered.

FACULTY OF ENGINEERING AND ARCHITECTURE

Shear wave elastography for assessing interstitial fluid pressure in tumours

Ariana Cihan
Student number: 02100167

Supervisors: Prof. dr. ir. Patrick Segers, Prof. dr. ir. Charlotte Debbaut
Counsellor: Dr. ir. Annette Caenen

Master's dissertation submitted in order to obtain the academic degree of
Master of Science in Biomedical Engineering

Academic year 2022-2023

GHENT UNIVERSITY

VUB VRIJE UNIVERSITEIT BRUSSEL